UNIVERSITÀ DEGLI STUDI DI PAVIA

Facoltà di Scienze Matematiche Fisiche e Naturali

Dottorato di Ricerca in Fisica
XI ciclo

Soft Multiparticle Production in $p\bar{p}$ Interactions at 1800 and 630 GeV

Tesi di dottorato di:
Niccolò Moggi

Tutore:
dr. **Gianluca Introzzi**

— Anno Accademico 1998/99 —

Contents

List of Figures

List of Tables

Introduction

Soft hadron interactions have been intensively and widely studied by ISR experiments in the 70's.

As the center of mass energy increased above the ISR region many remarkable changes have been reported in multiparticle production: correlations have been studied at the CERN $Sp\bar{p}S$ collider at energies ranging from 200 to 900 GeV and at the Fermilab's Tevatron. But no overall systematic analyses have been done in this field since then. Known data are often partial and limited to small phase space regions, so that direct comparison is not always possible.

This dissertation originates as a part of a more complex and complete work whose final goal is to try a new and non conventional approach to soft proton-antiproton interactions.

On one side the aim is the investigation for any specific behavior which – somewhat charaterising soft interactions – can help understand the transition from the soft multiparticle production to the rare high transverse momentum jet production.

On the other side the intent is to perform a systematic and comparative study of different types of correlations. More specifically, various correlations are analyzed as a functions always of the same reference variable(s) in order to extract a significant information on the complex dynamics of these interactions.

In this thesis I present some of the preliminary result that have been obtained in the last few years by the minimum bias group at CDF.

Chapter **1** is dedicated to a brief introduction to minimum bias physics and reviews some of the latest results on the subject.

Chapter **2** shortly describes the CDF experiment at Fermilab and those parts of the apparatus that are more relevant to the data presented in the analysis.

In chapter **3** I discuss the data sample and the selections that were applied. A Montecarlo study of the detector efficiency for minimum bias events is included.

In chapter **4** the minimum bias sample is analyzed. Two different and connected studies are introduced: the correlation of p_t with multiplicity and the dispersion of the mean event transverse momentum.

In chapter **5** the same analysis is developed in different ranges of transverse energy. Finally, a clustering algorithm is applied in order to study if and how a description of the min bias sample as a superposition of a "jet" and a "no-jet" subsample can help a better comprehension of the subject.

Chapter 1

Hadron Interactions

1.1 Forces and Particles

The universe appears to be governed by three kinds of forces: strong, electroweak and gravitational, and to be made of few "elementary" particles: leptons, quarks and bosons.

Strong forces act only at very small distances: they bind quarks into nucleons and nucleons together to make nuclei. Electroweak forces provide attraction between electrons and nuclei that build atoms and molecules and are responsible for the β decay of nuclei. Gravitational forces are the weakest: they are important for large bodies but negligible for nuclear and subnuclear particles.

All these apparently different forces are transmitted by specific integer-spin particles called bosons.

According to the Standard Model [1] the elementary [1] particles on which is based our present understanding of the physical world, are the leptons and the quarks. There are six types of leptons and six types of quarks, called flavors. All of them can be grouped into three generations or families.

All of them have an associated antiparticle with same mass and spin but opposite charge.

While leptons are subject only to electroweak interactions, quarks experience also the strong force. The description of this force requires to introduce a new quantum number: the color charge, which can take three possible values, say red, green and

[1] by *elementary* we mean structureless at all scales presently accessible

	flavor			charge
u-type quarks	**u**	**c**	**t**	+2/3
d-type quarks	**d**	**s**	**b**	-1/3
charged leptos	**e**	μ	τ	-1
neutrinos	$\nu_{\mathbf{e}}$	ν_μ	ν_τ	0
generation	1^{th}	2^{nd}	3^{rd}	

Table 1.1: "Elementary" particles.

blue. Each quark is supposed to have one of these possible colors. The gluons are the quanta of color fields and carry a color and an anticolor.

Quarks are bound together in hadrons by the strong color force via the exchange of colored gluons. All observed hadrons are described in the parton model as colorless states composed of three quarks (barions: qqq) or of two quarks (mesons: $q\bar{q}$). The quarks of these configurations are called *valence* quarks because they are responsible for the charge and other quantum numbers of hadrons.

The theory that describes strong (color) interactions is called *Quantum Chromo Dynamics* or QCD [2].

	EM	Strong	Weak		Gravitational
symbol	γ	g	Z^0	$W^\pm$	G
EM charge	0	0	0	± 1	0
spin	1	1	1	1	2
mass (GeV)	0	0	91.186	80.385	0
range (m)	∞	10^{-15}	10^{-12}		∞

Table 1.2: Carriers of the forces.

1.2 QCD and the structure of hadrons

In the QCD description of strong force the interaction is the result of the exchange of a massless gluon. Since the gluon is massless, the potential might be expected

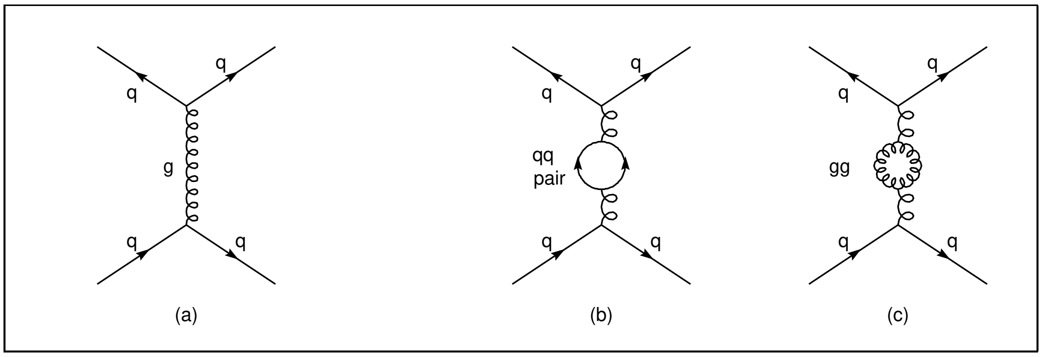

Figure 1.1: **(a)** Lowest order $q\bar{q}$ interaction. **(b)** and **(c)** lowest order corrections to the quark-quark coupling.

to fall as $1/r$ (where r is the distance) as in quantum electrodynamics, but actually behaves very differently at large[2] distances.

This is due to the fact that gluons carry color (while photons do not carry electromagnetic charge) and hence couple to each other. In quantum field theories like QED and QCD any charge (color or electromagnetic) is shielded by a cloud of polarized charges: a quark can emit a gluon which can convert into $q\bar{q}$ or gg pairs which in turn can radiate gluons and we have a branching tree of quarks and gluons (this effect is called *vacuum polarization*). Because of this effect of charge screening the charge one measures depends on the distance (or the wavelenght, or transfered momentum Q^2) with which one is probing the charge itself. We thus have a "running" coupling constant (α, in QED) which changes ("runs") with the transferred momentum:

$$\alpha = \alpha(Q^2) \qquad with \qquad Q^2 = -\mathsf{q}^2 > 0 \tag{1.1}$$

where q is the four-momentum of the virtual boson exchanged between the charges.

In QED this implies that at some very large Q^2 or very small distance the coupling $\alpha(Q^2)$ is infinite[3]. In QCD the situation is the opposite: the gluons, coupling each other, spread out the effective color charge of the quark so that it will be

[2] distances greater than the size of hadrons which is roughly ~ 1 fm (10^{-15} m).

[3] The bare charge is said to be "ultraviolet divergent". We should not worry about this divergency, though, since quantum gravity effects are expected to modify the coupling long before such very high Q^2 are reached. In the "infrared" region the q^2 dependence is experimentally undetectable.

preferentially surrounded by a cloud of charges of its same color. This result in an *antiscreening* of the color charge: by moving closer to the original quark the amount of the measured color charge decreases.

To first approximation in Q^2/Λ_{QCD} we have:

$$\alpha_S(Q^2) \simeq \frac{4\pi}{\left(\frac{11}{3}N_C - \frac{2}{3}N_F\right)\ln\frac{Q^2}{\Lambda_{QCD}}} \tag{1.2}$$

where N_C is the number of colors and N_F is the number of quark flavors. Λ_{QCD} is a parameter that, qualitatively, indicates the magnitude of the scale at which $\alpha_S(Q^2)$ becomes strong; it is determined experimentally to be about 0.2 GeV.

With three colors and six flavors we can see that $\alpha_S(Q^2) \longrightarrow 0$ (decreasing) when $Q^2 \longrightarrow \infty$, which means that quarks and gluons appear like almost free particles when probed at very high energy or short distances. This fact is called *asimptotic freedom* and allows perturbation theory to be applied to theoretical QCD calculations to produce experimentally verifiable predictions for hard scattering processes.

The other important consequence of equation 1.2 is that $\alpha_S(Q^2) \longrightarrow \infty$ when $Q^2 \longrightarrow \Lambda^2$ (which serves to define Λ_{QCD}) and so the coupling becomes stronger at larger distances and the perturbation series breaks down as $r \longrightarrow 1/\Lambda$.

When a quark and an antiquark are forced to separate, their color interaction becomes stronger and so the quarks (and gluons) can never escape.

This so-called *infrared slavery* is believed to be the origin of the confinement of quarks to colorless hadrons and explains why we do not observe free quarks.

From the phenomenological point of view, we can consider two hadrons colliding at high energy – such as at the Tevatron Collider – to be colliding broad-band beams of quarks, antiquarks and gluons.

Especially for bound states such as the proton, composed only of u and d quarks whose masses are small compared to the QCD scale Λ_{QCD}, the coupling α_S is $\gtrsim$1 and the probability of creating additional virtual gluons and $q\bar{q}$ pairs ("sea quarks") within the particle is very high. Whereas the number of valence quarks is fixed by the quantum numbers of the hadron, the number of virtual sea quarks and gluons that can be created is unlimited and rapidly fluctuating. Each parton i carries a momentum fraction x_i ($0\lesssim x_i \lesssim 1$) of the proton total momentum. In terms of this variable x (Bjorken-x) we say that the gluon and sea quark distribution becomes very large at small x.

1.3 Hadron Hadron Interactions

The scattering of two hadrons may be viewed as in figure 1.2. Though each hadron is an overall colorless cluster of partons, within it there will be a distribution of color charges, and the approach of another cluster will induce a redistribution (or polarization) of this color charge. We use to empirically classify the final states by the configuration of the interaction process.

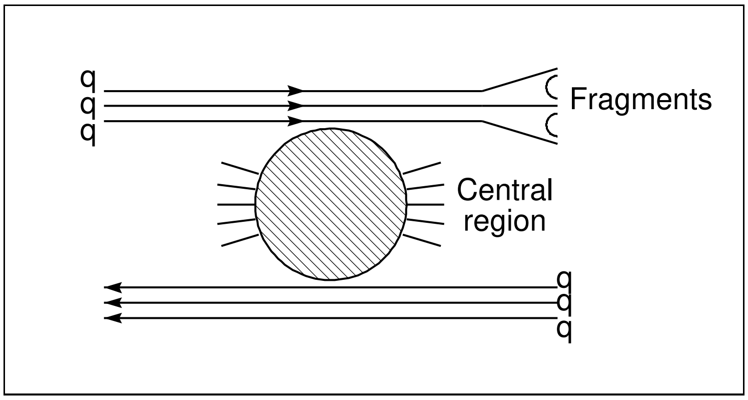

Figure 1.2: Naive picture of a generic $h\bar{h}$ scattering. The hadron coming from the left, after collision, fragments into new hadrons. The other hadron does not fragment and is said to be a "leading" particle. Many soft hadrons are produced in the central region.

a. One or both the hadrons may be rather little affected by the interaction. But because of the excitation they may form into new colorless hadrons, which we call *fragments*. Fragments manifest themselves as spreads or jets of particles in the forward and/or backward directions (*fragmentation region*).

b. Those partons which happen to be travelling very slowly in the center of mass at the moment of the collision, may combine to produce new hadrons, nearly at rest. These low momentum particles populate the *central region* of the interaction. Most of them are pions, since the pion is the lightest hadron and hence it occurs in the decay products of most hadrons, and are not particularly associated with anyone of the colliding particles. The momentum transferred by the color force is quite small: in the final state the total transverse momentum is only a small fraction of the total momentum of the interacting particles and the collision is said to be *soft*.

c. A third set of different processes involves direct quark-quark interaction at small impact parameter. In the parton picture this means that two partons have passed very close to each other and so have scattered at wide angles. The scattered partons produce two jets of hadrons (see § 1.5); the rest of the incoming hadrons continue almost undisturbed and give rise to a soft scattering. These rare processes require the transferred momentum to be very high and are therefore called *hard scattering* processes.

Following this classification the total $p\bar{p}$ cross section can be conveniently subdivided into three terms:

- elastic[4];
- single and double diffractive (described in point **a**);
- non-diffractive inelastic (described in **b** and **c**).

$$\sigma_{TOT} = \sigma_{EL} + (\sigma_{SD} + \sigma_{DD}) + \sigma_{ND} \tag{1.3}$$

At the energy range from few GeV to 2 TeV (Tevatron) the total $p\bar{p}$ scattering cross section varies very slowly with the `c.m.s.` energy. As most hadron-hadron reactions, it falls a bit at lower energies and rises for $\sqrt{s}$ >30 GeV. The measures at the higher energy available (1.8 TeV at the Tevatron) yield (experiments E710 and CDF):

$$\sigma_{TOT}\text{=72.8}\pm\text{3.1 mb [3]}$$
$$\sigma_{TOT}\text{=80.03}\pm\text{2.24 mb [4]}$$

The elastic and single diffractive cross sections [4] are:

[4]Elastic scattering is the special case in which the incoming clusters of partons retain their integrity and are not broken up to form new hadrons. Experimentally is defined when in the final state are present only the incoming protons travelling on trajectories (different from the beam one) that originate from a common vertex.

$$\sigma_{EL}=19.70\pm0.85 \text{ mb}$$
$$\sigma_{SD}=9.46\pm0.44 \text{ mb}$$

and the inelastic non-diffractive amounts to about 45 mb. The global dependence of σ_{TOT} with $\sqrt{s}$ seems to favour a logaritmic dependence:

$$\sigma_{TOT} = \ln^{\alpha}(s) \qquad \alpha \simeq 2 \tag{1.4}$$

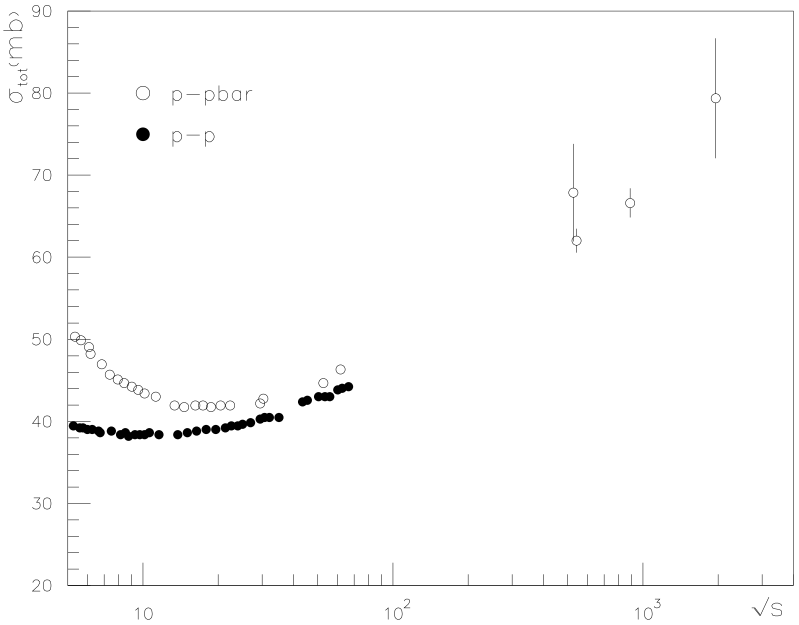

Figure 1.3: The dependence of the total cross section on the `c.m.s.` energy (GeV).

1.4 Inclusive Processes

At high energy the final state if often quite complex, several particles being produced in a collision, some of which are likely to miss any detectors which have been set up. It is common to measure the so called *inclusive* single particle cross section. For the process:

$$AB \longrightarrow C + X \tag{1.5}$$

C is the detected particle and X symbolizes all the other particles that may have been produced but have not been observed.

The Lorentz-invariant single particle distribution for this kind of process can be written as:

$$f(AB \to CX) \equiv E_C \frac{d^3\sigma}{d^3\vec{p}_C} = \frac{E_C}{\pi} \frac{d^2\sigma}{dp_L dp_t^2} \tag{1.6}$$

where $\frac{d^3\sigma}{d^3\vec{p}_C}$ is the differential cross section for detecting particle C within the phase space volume element $d^3\vec{p}_C$; p_L and p_t are the component of p_C along and transverse to the beam direction, respectively.

It is convenient to introduce here the variables commonly used to describe inclusive processes.

If θ is the angle at which a particle is produced with respect to the beam direction, then we define the longitudinal and transverse momenta:

$$p_L = |\vec{p}| \cos\theta \tag{1.7}$$

$$p_t = |\vec{p}| \sin\theta \tag{1.8}$$

The transverse momentum is invariant for Lorentz boost. The Lorentz-invariant square of the total center of mass energy is usually written as:

$$s = (E_A + E_B)^2 \tag{1.9}$$

where $E_{A,B}$ are the total energies of the incident particles. At collider experiments particles A and B usually have equal and opposite momenta.

The dimensionless variable

$$x \equiv \frac{p_L}{|\vec{p}|} \tag{1.10}$$

measures, in the `c.m.s.` frame, the fraction of the beam's momentum $\vec{p}$ which is contained by the longitudinal momentum component p_L of the detected particle. It is called *Feynman-x* [5] and varies from -1 to 1.

In hadron-hadron collisions the beam axis has a special significance: we use this axis to define another longitudinal variable called *rapidity*. The rapidity y is just the particle velocity component along the beam axis $\beta \cdot c = dz/dt$ defined by:

$$y \equiv \frac{1}{2} \ln \frac{E + p_L}{E - p_L} \tag{1.11}$$

[5] not to be confused with Bjorken-x.

Clearly y depends on the choice of the frame, but it has the advantage that rapidity differences are invariant under Lorentz boost. A particle of mass m travelling along the rapidity axis with momentum p has a rapidity $y = ln(E+p_L/m)$ whose maximum value is 7.5 for a proton in a $900 + 900$ GeV collision. The full rapidity coverage is:

$$\Delta y \simeq \ln \frac{s}{m^2} \tag{1.12}$$

In high energy processes it is more convenient to use the so called *pseudo-rapidity* that does not require to measure the mass of the particle:

$$\eta = \frac{1}{2} \ln \frac{p + p_z}{p - p_z} = -\ln \tan \frac{\theta}{2} \tag{1.13}$$

The pseudorapidity η is defined in such a way that at large values it does not saturate but keeps going: as $\beta \to 1$, $\eta \to \infty$. It is a good approximation to y as long as the mass is small compared to p_t:

$$\eta \longrightarrow y \quad \ for \quad p_t \gg m \tag{1.14}$$

1.5 Parton Model and Large P_t Processes

Hadronic collisions which involve a short distance scattering can be described, in first approximation, by the Parton Model. Since the transfered momentum is the conjugate variable of the (quark-quark) impact parameter, large Q^2 implies that partons have scattered at small distances where α_S is small. In order to be able to apply perturbation theory one needs a momentum transfer of about 10 GeV: from the uncertainty principle we calculate that the associated distance is in the order of 10^{-17}m. From the experimental point of view there is no certain way to separate such rare events but intuition suggests that large p_t final state particles should be a good indication and experiments fully support this.

We can picture this scattering process as a sequence of three different phases occurring at different time scales [6].

[6] We imagine the proton as constantly dissociating into virtual states of free partons. The time duration of a collision during which the boson energy q^0 is absorbed by the proton is of the order

1. Partons approach each other with a momentum distribution given by a "Parton Distribution Function" (PDF). Parton transverse momenta are neglected.

2. A hard collision takes place between a pair of partons regarded as free particles. The cross section involves only high momentum transfer and does not depend on the details of the hadron wave function or on the type of hadrons. Thanks to asymptotic freedom it can be computed by perturbative QCD.

3. The two partons shot out sideways with large transverse momenta, generate more quarks and gluons which subsequently rearrange into new hadrons. This process is called *fragmentation*.

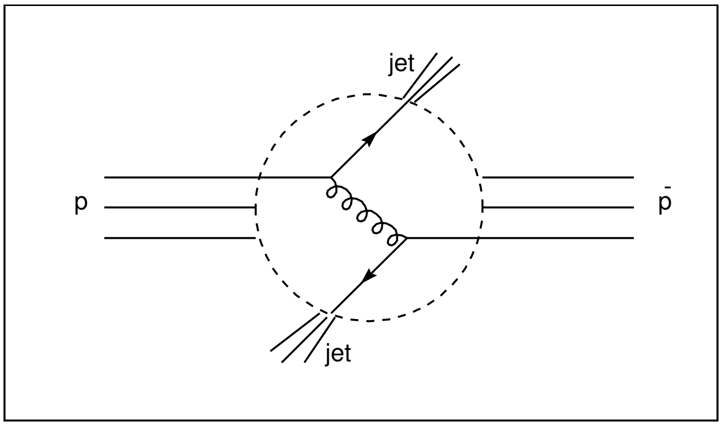

Figure 1.4: Scattering of quarks observed as di-jet final state.

The fragmentation process typically involves the creation of additional $q\bar{q}$ pairs in a perturbative evolution during which partons loose their energy through bremstrahlung and pair production from the color force field.

The branching process repeats itself until the invariant mass of the string is small enough. When the parton shower is terminated a collection of partons –or clusters of partons– with virtual mass squared in the order of the cut-off scale t_0 (typically ~ 1 GeV^2) is left.

$\tau_{coll} \sim 1/q^0$. If the colliding time is much shorter than the virtual state lifetime we may treat the partons as free during the collision. These time scales depend on the Lorentz frame we use; the justification for the parton model is made in a frame where the proton is moving very fast so that, by relativistic time dilatation, its clock runs very slowly. We must establish, however, that $\tau_{coll} \ll \tau_{virt}$ in this frame [5].

In the `c.m.s.` the new hadrons emerge from the collision more or less in the same direction of the originating quark and form two opposite (in ϕ) back-to-back jets of particles. This picture suggests that the properties of the jet depend only on the initial quark: thus, each fast parton fragments independently, as first approximation. This is a manifestation of a more general approach to hadronization called *local parton-hadron duality*. In this approach it is assumed that the flow of momentum and quantum numbers at the hadron level tends to follow the flow that originates at the parton level.

The essential assumption of the parton model, leading to the expectation of jets, is that the transverse momenta of quark fragmentation products come mainly from soft processes and remain small, whereas the longitudinal momenta can increase with the quark energy.

In order to make quantitative predictions a more specific hadronization model is needed. The string model will be briefly described in § 1.8.1; many other models have been developed over the years whose description goes beyond the limits of this dissertation.

1.5.1 Parton-parton Cross Section

In the parton model approximation the invariant cross section for the inclusive reaction $AB \longrightarrow CX$ can be expressed as the weighted sum of differential cross sections of all the possible parton scatterings that can contribute.

In hard parton collisions, however, the cross section of scattered partons rises very rapidly with $\sqrt{s}$. The sea gluon and quark density become very large at very small x: the momentum fraction $x \sim \sum |p_t| / \sqrt{s}$ for producing a given large transverse momentum get smaller when $\sqrt{s}$ increases.

Hence we expect that hard parton-parton scattering and jet production will dominate the cross section for sufficiently large $\sum |p_{ti}|$ at sufficiently high energy (see the case of *mini-jets* in § 1.7). However, the total interaction cross section for n partons confined in a box (the hadron) cannot greatly exceed the size of the box itself, no matter how large n may be. A correct treatment cannot simply add parton cross section incoherently but must take into account multiple scattering, shadowing and screening corrections, etc.

1.6 Central Hadron Production and log(s) Physics

As already mentioned, the overwhelming part of inelastic non-diffractive $p\bar{p}$ cross section is due to "soft" processes with small transverse momenta with respect to the collision axis. Soft processes are associated with coherence effects among (already) interacting partons. At high energies these processes typically result in the production of ten to hundreds of particles in the final state and many variables are involved.

Even so, in principle, it should be possible to compute the properties of soft multiparticle events from the Lagrangian of QCD which is now the accepted theory of strong interactions. However no short distance (high Q^2) interaction is involved and the coupling is much too large for perturbation theory to be sensible. Hadron dynamics involves QCD at a length scale of $\sim$1 fm, which corresponds to a coupling constant of order unity. Alternative non perturbative procedures must be adopted. The best that can be done at present is to develop simplified models (see § 1.8) that account for the phenomenology already known.

The behavior of particles produced in the central region is independent of the identities of the initial colliding particles. We can imagine that, due to the collision between two parton clusters, a "blob" of excited matter is produced. During the expansion of the blob, light hadrons are formed in the central rapidity region which have no memory of the initial state. In other words, the number of $q\bar{q}$ pairs in the hadron sea is so large at small x that the influence of the initial quantum numbers is negligible and the particle distribution is independent of the incident hadrons.

Even though the details of the dynamic are not understood, it has become clear that many dynamical quantities of soft, high cross section, processes show the same logaritmic dependence with $\sqrt{s}$ as the total cross section. These and other features characterize soft central production. We usually refer to these phenomena as "log(s)" physics. Here we discuss:

- average number of particles produced $\Rightarrow$ $\langle n \rangle \sim \log^2(s)$
- average transverse momenta $\Rightarrow$ $\langle p_t \rangle \sim \log^2(s)$
- particle density in the central region $\Rightarrow$ $\left.\frac{dn}{d\eta}\right|_{\eta=0} \sim \log^2(s)$

Many different correlations are present among final state particles. Their study can provide information on hadron dynamics beyond that obtained from single particle inclusive spectra. In this dissertation we are concerned only with the correlation of particle's momentum with multiplicity.

As already mentioned, the invariant cross section can be factorized (see equation 1.6), and, at fixed energy, depends only on p_t and p_L (or rapidity). Therefore the cross section of inclusive particle production can be analyzed as a function of just one variable at a time.

1.6.1 Rapidity Distribution

The cross section as a function of the pseudorapidity in the `c.m.s.` is shown in figure 1.5. The distribution exhibits a central plateau at small η and a falling cross section (not shown in the figure) in the fragmentation region where $y \longrightarrow y_{\max}$. The width of the plateau increases with $\ln(s)$.

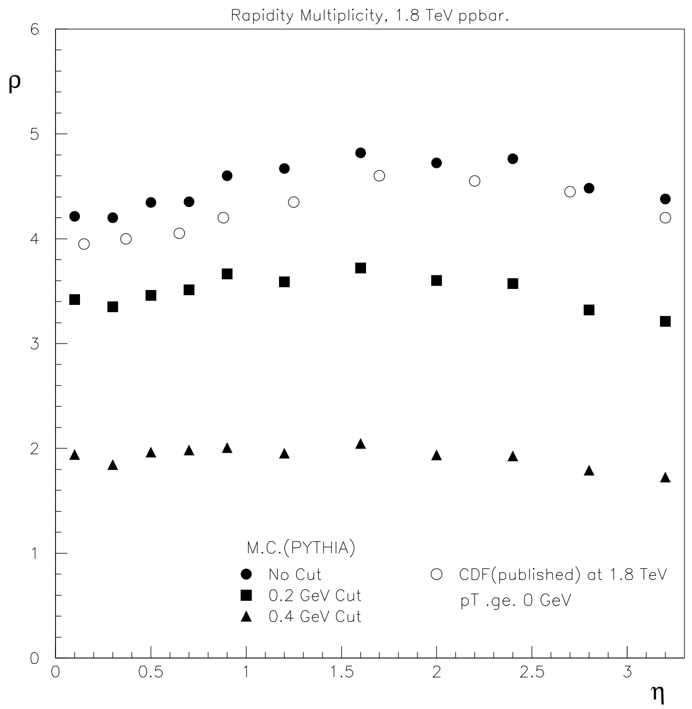

Figure 1.5: Pseudorapidity distribution in the central region at $\sqrt{s}$ =1.8 TeV.

The multiplicity density $\rho = dN_{ch}/d\eta$ in $\eta = 0$ is shown in figure 1.6 as a function of the `c.m.s.` energy. A fit by UA5 [6] to a $\log(s)$ dependence yields:

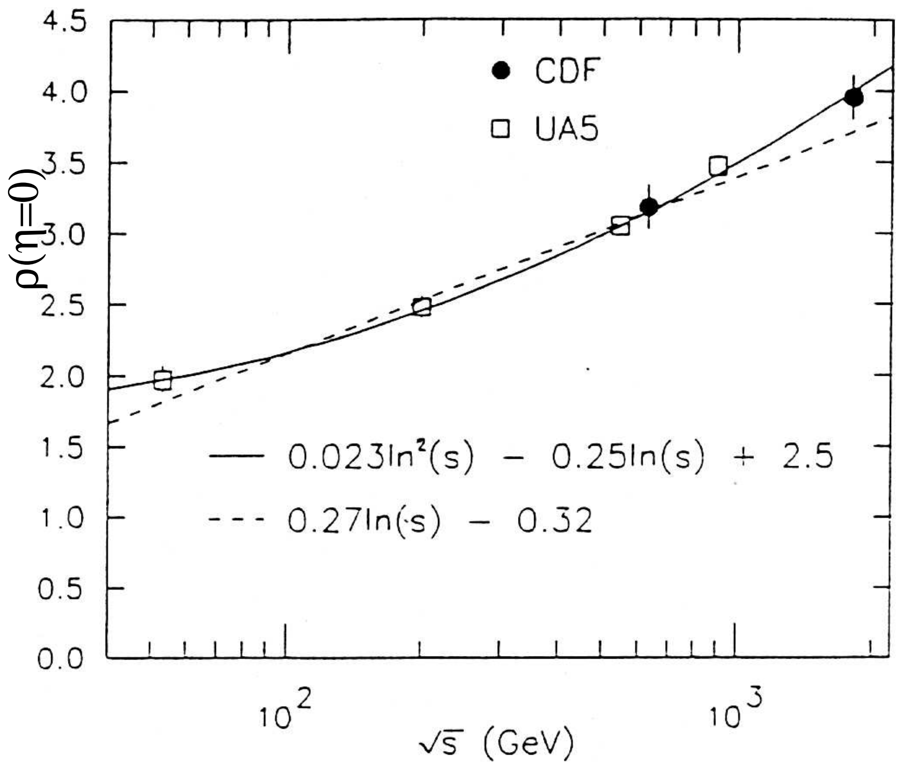

Figure 1.6: Growth of the height of the central plateau with $\sqrt{s}$.

$$\rho(\eta = 0) = (0.01 \pm 0.14) + (0.22 \pm 0.02)\log(s)$$

The data from CDF [8] seems to favor a $\log^2(s)$ dependence. This value has been measured to be $3.18 \pm 0.06 \pm 0.10$ at 630 GeV and $3.95 \pm 0.03 \pm 0.13$ at 1800 GeV.

1.6.2 P_t Spectrum

The exponentially falling spectrum in transverse momentum, p_t, of the produced particles, is one of the most interesting characteristics of hadronic collisions and is considered to be directly related to the underlying scattering process [9].

At *SpS* and higher energies there are non exponential tails at high transverse momenta which indicate the onset of hard scattering contributing to the cross section [10]. Again, the average p_t as a function of $\sqrt{s}$ rises logaritmically. The data, spanning an energy range from 25 to 1800 GeV, is well fitted with quadratic logarithmic law of the form [7]:

$$\langle p_t \rangle = 0.40 - 0.030\log(\sqrt{s}) + 0.0053\log^2(\sqrt{s})$$

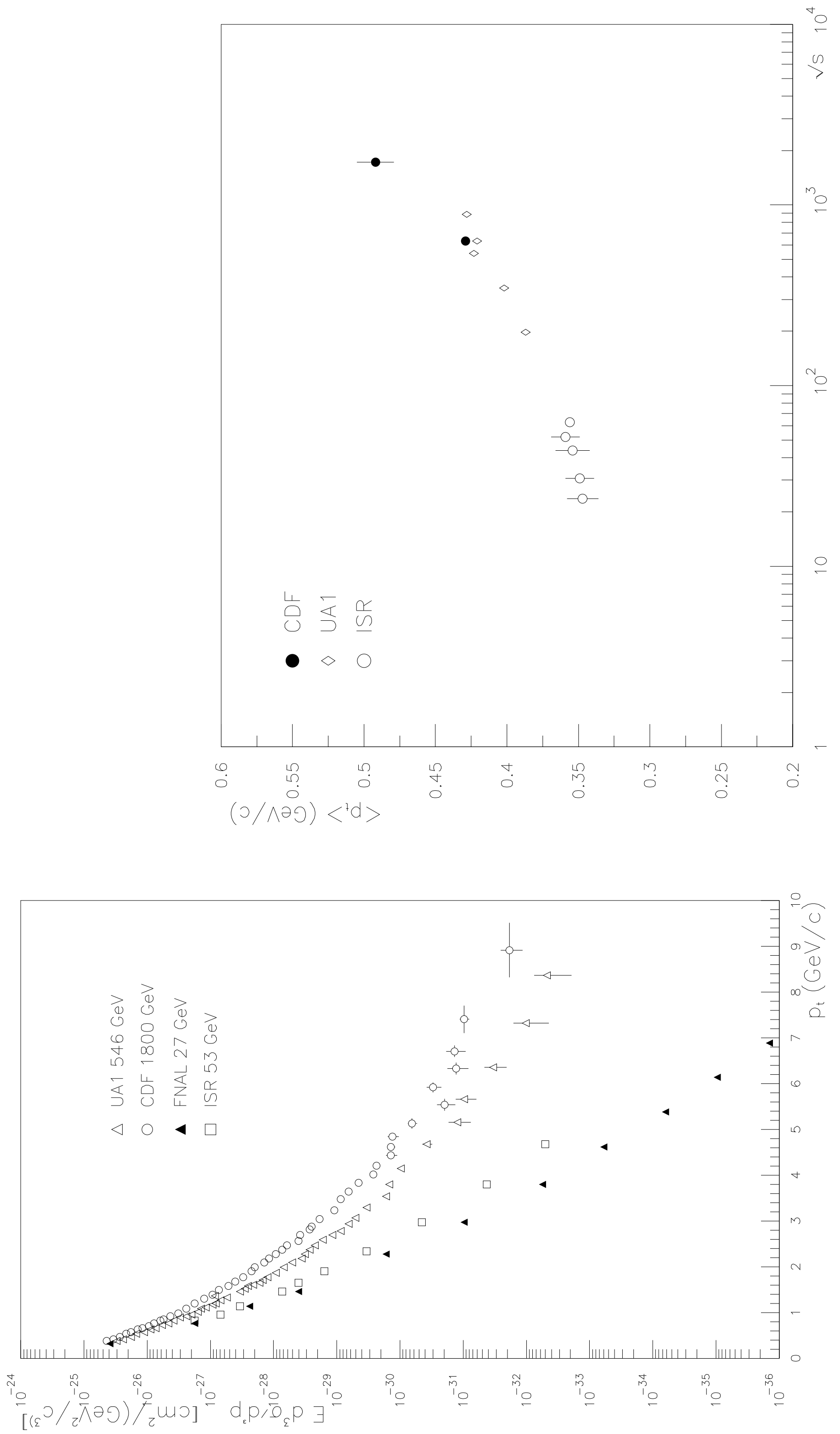

Figure 1.7: Lower (left): invariant inclusive cross section as a function of p_t. Upper (right): growth of $\langle p_t \rangle$ with $\sqrt{s}$.

1.6.3 Multiplicity Distribution

The multiplicity distribution describes the frequency with which is produced, in a single interaction, a final state composed of n particles. n is an integer which range from the lowest compatible with the conservation of the initial quantum numbers (zero, in $p\bar{p}$) to the maximum value compatible with energy-momentum conservation. Since CDF, as most experiments, can count only charged particles, from now on we will write "multiplicity " for "charged multiplicity ".

The probability of a final state with n_{ch} charged particles is

$$P\left(n_{ch}\right) = \frac{1}{N_{ev}} \frac{dN_m}{dn_{ch}} \tag{1.15}$$

where N_{ev} is the total number of events analyzed and N_m the number of events with a given fixed multiplicity. The mean value of the distribution is defined by:

$$\langle n_{ch} \rangle = \sum_{n_{ch}=0}^{\infty} n_{ch} \cdot P\left(n_{ch}\right) \tag{1.16}$$

The total charged multiplicity of an event is given by the integral of the charged particle density distribution:

$$N_{ch} = \int \frac{dN_{ch}}{d\eta} d\eta \tag{1.17}$$

The average number of particles produced in a collision increases with the energy. A fit to the data by UA5 [11] yield:

$$\langle n_{ch} \rangle = 2.99 - 0.23 \log(s) + 0.168 \log^2(s)$$

The $\log^2(s)$ dependence is confirmed by CDF [12] and can be readily understood considering that both the pseudorapidity density distribution at $\eta = 0$ and the kinematically allowed η range have a simple logaritmic dependence on the `c.m.s.` energy.

The particular form of the distribution is due to the correlations among final state particles. An independent emission of every single particle would give rise to a poissonian distribution. The consistent deviation from this shape is an important insight on the particle production process. Starting from the phenomenology of the multiplicity distribution it has been found that –in first approximation– $\bar{n}P(z)$ scales in terms of $z = n/\bar{n}$. In other words the (unknown) function $\Psi(z) = \bar{n}P(z)$

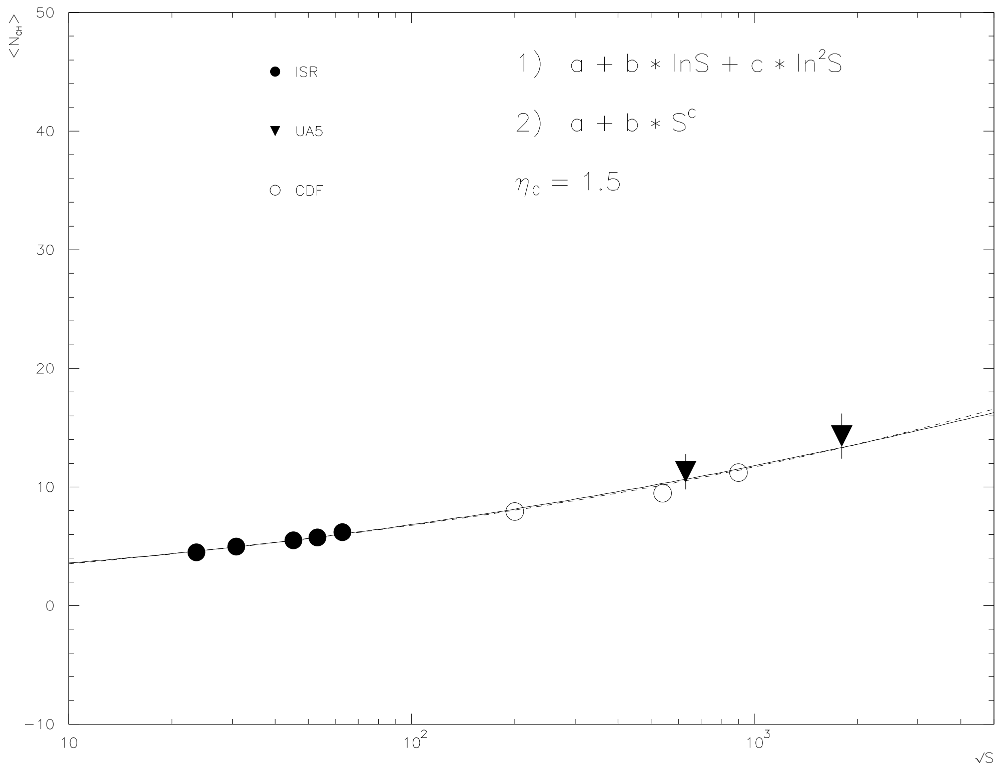

Figure 1.8: Growth of $\langle n_{ch} \rangle$ with $\sqrt{s}$.

depends only on the `c.m.s.` energy and the shape of the multiplicity distribution is constant if plotted against the variable z. This property, called KNO scaling [18], is not exact (at energies $\geq$540 Gev it is violated, especially in large rapidity intervals [12, 15]) but the important role played by the average multiplicity $\bar{n}$ might indicate the existence of some statistical effect.

A lot of work has been done in the attempt of describing the data and fits were tried with many different functions [13]. Among these, the Negative Binomial [14] (NBD) seems to be the most promising, fitting e^+e^- data and $h\bar{h}$ data up to ISR energies in the full phase space[15]. However at higher energies shoulder structures start to be clearly visible as shown by the UA5 Collaboration at the CERN $p\bar{p}$ collider [15]. At 900 GeV NBD cannot be trusted in pseudorapidity intervals larger than 5 units [16] and at 1800 GeV in intervals larger than 0.5 units [12].

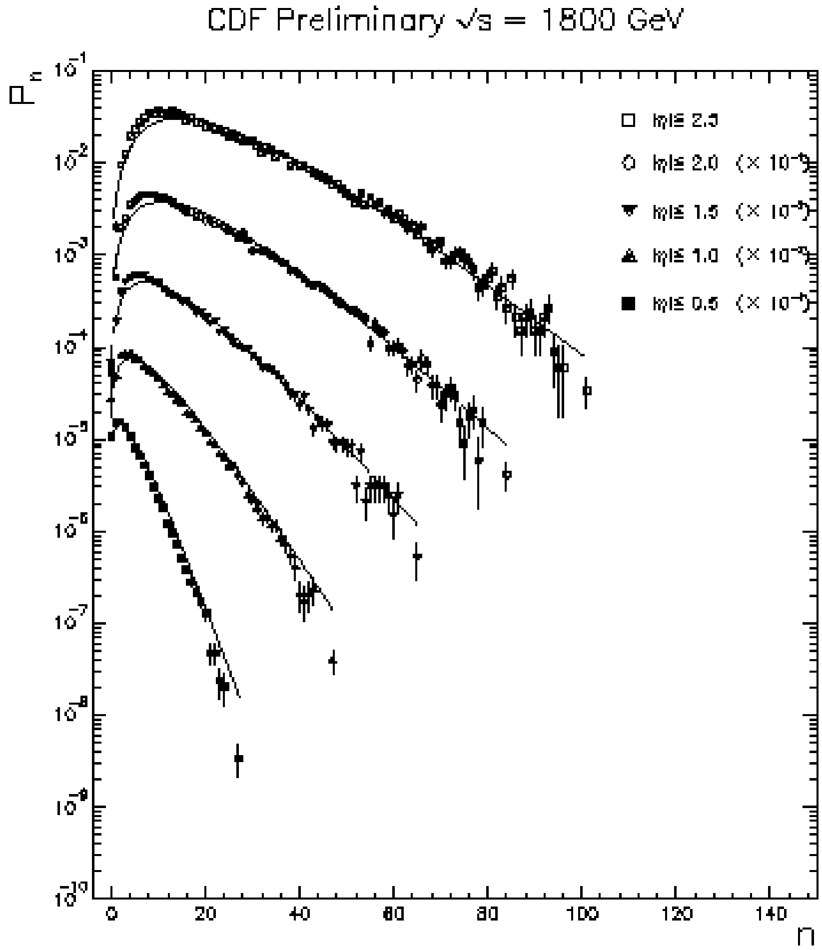

Figure 1.9: Multiplicity distributions at $\sqrt{s}$ =1800 GeV in various pseudorapidity ranges. Data are fitted with a Negative Binomial Distribution.

1.6.4 Dependence of $\langle p_t \rangle$ on Multiplicity

The behavior of the p_t distribution in relation to the event multiplicity has been one of the most important subjects in minimum bias physics. An increase of $\langle p_t \rangle$ with increasing charged particle density in the central region has first been observed by UA1 [17] and other experiments [10, 19, 20].

Due to large systematic errors coming from calculation of the $\langle p_t \rangle$ and statistical errors on true multiplicities of the high density events, the shape of the correlation is an open question, but it is clear that it is the high multiplicity events that have the higher average p_t per particle, which is the opposite of what one would expect from kinematics under the condition of particle density saturation.

Many interpretations have been proposed in terms of semi-hard effects [21] in the central region or possible hadronic phase transition [22], but the correct explanation is still unknown.

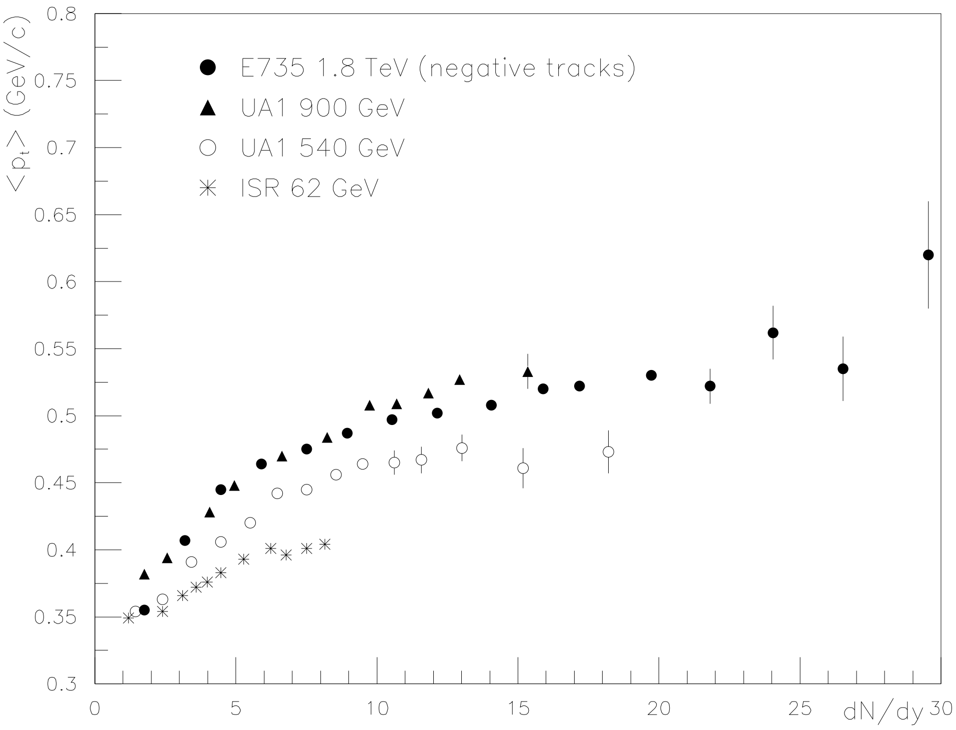

Figure 1.10: Correlation between $\langle p_t \rangle$ and particle density at various energies.

1.7 Introducing *Mini-Jets*

Up to energies of about 50 GeV the average transverse momentum of particles is independent of the other reaction variables, such as the multiplicity.

One of the interpretations proposed for the change in characteristics of minimum-bias events as $\sqrt{s}$ increases is that an increasing fraction of the inelastic non diffractive cross section (σ_{ND}) contains QCD jets:

$$\sigma_{ND} = \sigma_{no-jet} + \sigma_{jet} \qquad (1.18)$$

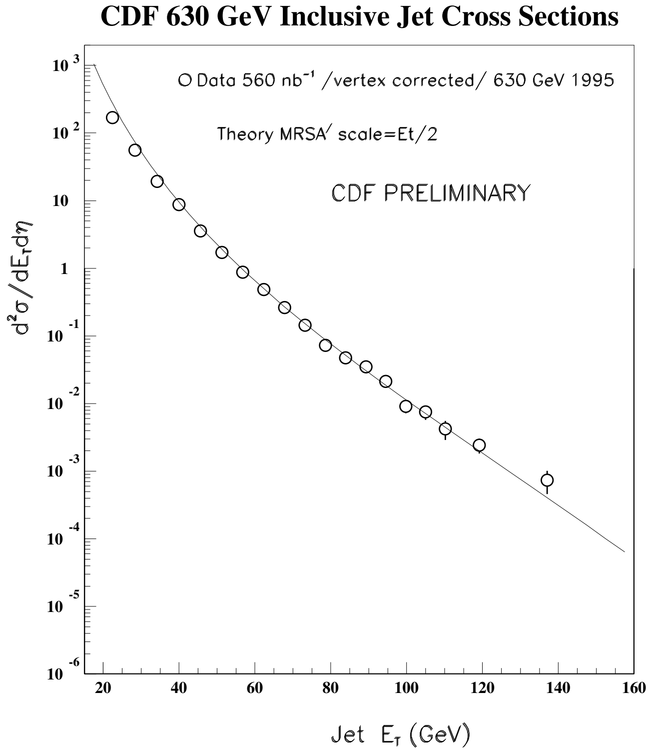

Figure 1.11: Inclusive jet cross section as a function of jet transverse energy at c.m.s. 630 GeV from CDF.

The term σ_{jet} would be the result of hard collisions of low Bjorken-x partons. Here the idea is that jet production gains in importance with increasing energy and is sufficient [27] to accommodate many of the features shown by the data as the rise of the total cross section, of the central rapidity plateau, of the p_t spectrum tail and the correlation of $\langle n_{ch} \rangle$ with multiplicity. In the model there is no indication on where to fix the onset of jet production. Experimentally no evidence of the presence of a boundary between the two production mechanisms has ever been noticed.

At $\sqrt{s} \ll 1$ TeV hadrons interact via their valence quarks. When $\sqrt{s}$ approach the threshold of ~ 1 TeV the density of semi-soft gluons in the hadrons get very large [28] and calculations using the hard scattering mechanism predicts a large cross section dominated by gg contributions.

Experimentally these interactions manifest themselves with the presence, in the final state, of one or more "mini-jet": a mini-jet is a jet whose transverse momentum p_t is large if compared with the nucleon mass but much less than the c.m.s. energy.

According to some authors [29] perturbative calculations are possible down to p_t in the order of the QCD scale Λ_{QCD}, i.e. for $\Lambda_{QCD}(\simeq 200\text{ MeV}) < p_t \ll \sqrt{s}/2$. In this semi-hard momentum regime it would be possible [27] to compute the inclusive jet cross section down to $p_t > p_{tmin} \simeq 1$ GeV. This would contribute to σ_{tot} up to about 30 mb at 1800 GeV [30].

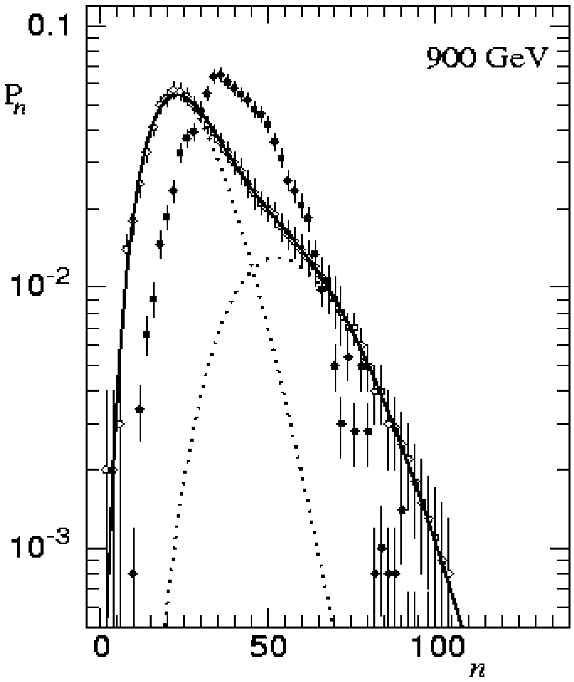

Figure 1.12: Charged multiplicity distributions at `c.m.s.` energy 900 GeV. Data (open dots) are from UA5 Coll. The dotted line show results from MC calculation (Pythia). The solid line is a fit with the superposition of two NBDs.

However, there is no theoretical understanding of how small p_t is allowed to be with such calculations still being valid. When p_t is not very large there are theoretical and experimental difficulties in distinguishing the particles in the mini-jet from the other particles produced in the reaction.
The UA1 Collaboration reports [31] the presence of QCD jets right down to $p_t = 5$ GeV with a growing production cross section which is close to 20 mb at 900 GeV.

It is worth noting that at higher energies the shape of the multiplicity distribution has an appearance such that may suggest a two-component structure. This feature can be modelled [32] as the effect of the superposition of two independent Negative

Binomial distributions, accounting one for soft and one for semi-hard (mini-jet) events.

1.8 Particle Production Models for Soft Hadronic Interactions

During the years a number of simplified phenomenological models have been developed in order to describe soft particle production.

In most models particle production is assumed to have two components. The hard interaction is described by perturbative QCD. The soft component – the basic mechanism for particle production – is usually described as a separation of color charges resulting, through different mechanisms, in low-p_t production. At higher energies many of the changes in the event characteristics can be described increasing the number of strings.

On the other hand a completely different statistical approach: the entropy (proportional to the number of particles in the final state [37]) is produced very early after the collision, at a time less than about 1 fm, with the produced plasma of particles then flowing outwards according to the laws of hydrodynamics.

1.8.1 Pythia

Pythia is the name given to a MonteCarlo generator developed by the Lund University group [33]. The approach used is an attempt to extend the perturbative parton-parton framework into the low-p_t region.

In this model the simplest possible way to produce a (soft) event is to have an exchange of a very soft gluon between the two colliding hadrons. Without initially affecting the momentum distributions of partons, the hadrons become color octet objects rather than color singlet ones. If only valence quarks are considered, the color octet state of a barion can be decomposed into a color triplet quark and an antitriplet diquark.

When a color-neutral quark-diquark pair is produced in a $p\bar{p}$ collision, a color force field is created between them. Because of the interactions of gluons with one

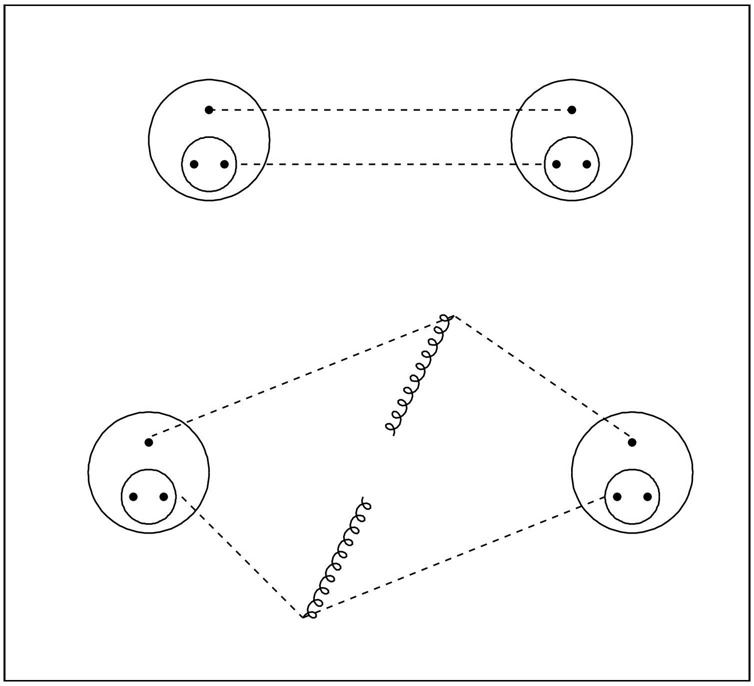

Figure 1.13: Up: $p\bar{p}$ scattering; dashed lines represent the strings. Lower: $p\bar{p}$ scattering including a hard gg scattering.

another the color field lines of force are contained in a tube-like region. Since the potential is linear ($V(r) \sim r$) the force between the color charges remains approximately constant with separation and the tube acts as a string with constant tension[7]

As the quarks fly apart they are decelerated by the string tension, accelerated back together and then fly apart once more executing periodic oscillations.

The color force field may materialize a massless $q\bar{q}$ pair of zero energy-momentum at a point of the string. The string then separates into two independent color-neutral string. As time develops the string breaks randomly into smaller pieces carrying smaller fraction of the initial energy. When the invariant mass of a string piece gets small enough it is identified as a hadron (or cluster of hadrons) and the breaking stops within that piece [34]. Thus the whole system eventually evolves into hadrons.

If gluons are present they are assumed to produce kinks (excitation) on the

[7]This picture is consistent with Regge phenomenology, heavy quark spectroscopy and lattice QCD which indicate a value of the string tension [34]

$$k \simeq \frac{1\ GeV}{1\ fm} \approx 0.2\ GeV^2 \tag{1.19}$$

strings so to bend them and to produce two strings, each one having one end on the gluon. Hadrons will then be forming also in the "middle" gluon region and the resulting angular distribution is not symmetrically distributed about the parton axis.

If we assume that all the breaks occur during the first expansion phase of the oscillation, the evolution can be expressed as a stochastic process.

Pythia assumes that different pairwise interactions can take place independently so that the number of scatterings in a collision, for a fixed hadron-hadron impact parameter, is given by a poissonian distribution. Radial hadronic matter distribution in the hadron is assumed to be double gaussian.

The parton-parton hard cross section σ_{hard} has been computed to be comparable to the total cross section down to $p_{t_{min}} \approx 1.5 - 2$ GeV. A gradual turn off at low p_t is used instead of a sharp cut-off so that a continuous spectrum is obtained from $p_t = 0$ to $\sqrt{s}/2$. For $p_t \gg p_{t0}$ the standard perturbative QCD cross section is recovered, while values $p_t \ll p_{t0}$ are strongly dumped. The p_{t0} scale, which is the main free parameter of the model, comes out to be of the same order of magnitude as $p_{t_{min}}$, i.e. about 2 GeV. The p_{t0} at a given `c.m.s.` energy is determined by the requirement that the mean charged multiplicity in the model should agree with the experimental one.

Within the model the total multiplicity distribution can be separated into the contribution from diffractive events, events with one interaction, with two interactions and so on. The low multiplicity tail is dominated by double diffractive events and the high multiplicity one by events with several interactions. The average charged multiplicity increases with the number of interactions.

1.8.2 Dual Parton Model (DPM)

DPM [35] describes soft interactions among protons by single and double Pomeron exchange[8]. Chains are assumed to be formed by Pomeron exchange where each Pomeron gives rise to two chains stretched between either valence or sea partons.

[8]A Pomeron is a color neutral object which in the parton model can be identified as a gluon-gluon pair. In Regge theory it is the highest of Regge trajectories. For a complete dissertation about Regge theory and phenomenology refer to [36] and references therein.

The leading contribution to particle production (soft interaction term) is a two-chain diagram, i.e. the simplest topology with vacuum quantum number exchange. In the case of a proton the collision separates the valence quarks of each incident parton into two colored systems: a slow "held back" quark and a fast diquark. The fragmentation occurs in the form of two quark diagram chains, each chain being an overall color singlet which contains a quark fragmentation region and a diquark fragmentation region.

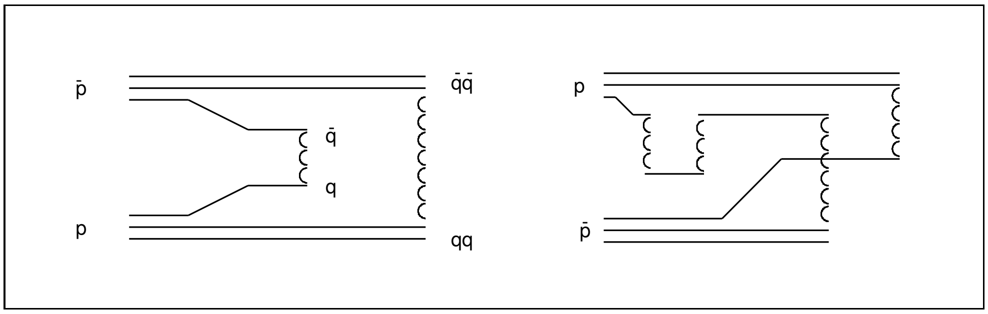

Figure 1.14: Left: two chain diagram for $p\bar{p}$ scattering in DPM. Right: four chain diagram.

Corrections to the leading two-chain diagram come from multiple Pomeron exchanges, corresponding to multiple inelastic scattering. The new chains connect sea partons. Since sea partons carry only a small fraction of the momentum of the incident hadrons, the chains are concentrated in the central rapidity region. Each chain must have a minimum threshold center of mass energy in order for physical hadrons to materialize from it. Therefore at higher energy the multichain contribution becomes increasingly important and the average number of chains increases with $\sqrt{s}$. Thus, these extra chains might explain the rise of the central particle density. In all the processes each chain is assumed to be independent of other chains and the hadronic spectra of each chain are obtained from the convolution of momentum distribution functions and fragmentation functions.

1.8.3 Statistical approach

It is generally assumed [37] that the energy formed in a collision emerges from a region no more than a fermi thick. If this is true, it follows from simple geometry that the produced hadrons cannot be formed until the radius of this shell is more than 5 fm, because otherwise the hadrons would be overlapping so much that there would be no way to consider them as real particles. Therefore some kind of collective quasi-macroscopic transport phenomena must occur.

Many models approach these phenomena through statistical physics. They all originate from a statistical model proposed by Fermi in 1950 for multiparticle production processes in nuclear collisions [38]. According to the main assumptions of the model the process of multiparticle production occurs via the creation of a unique system in which a thermodynamical equilibrium is established. Distributions of secondary particles are described by thermodynamical formulae for blackbody radiation.

At higher energies the evolution of the system can be better described as a hydrodynamical expansion of a blob of nuclear matter [39]. Incidentally, this idea has the nice advantage that it naturally explains the limited transverse momenta observed in soft production.

It has been suggested by many authors [40] that the initial system of hadronic matter could be formed of a plasma of quarks and gluons (*Quark-Gluon Plasma* or QGP). Quantum Chromodynamics predicts [41] that when hadronic matter is raised to sufficiently high temperature or matter density, a phase transition takes place: beyond the transition matter behaves like an ideal gas of quarks and gluons which are no longer confined within individual hadrons. This is because of the property of asymptotic freedom of QCD. If many quarks are very close together, a given quark will not feel any force from the other quarks far away from it: these forces are screened by the nearer quarks. But the nearby quarks are very close and so the force that they produce is weak and they can move freely through the plasma over long distances.

At energy densities higher than 1-2 GeV/fm^3 [42, 43] one can expect the appearance of QGP. Many estimates [42, 44] show that such energy densities can appear in nucleus-nucleus collisions and in high energy hadronic interactions.

All the incident energy, deposited in a small space region, thermalizes (i.e. undergoes that process that tends to thermodynamical equilibrium). After the possible plasma formation the system will expand and cool down to a critical temperature $T_C \approx 200$ MeV. Below this temperature hadronization occurs and the blob decays into the final particles.

Since the time needed for a quark to hadronize is about 1 fm/c [45] it is not clear if the system lifetime is long enough to reach thermodynamical equilibrium. This determines whether we have a hydrodynamical plasma expansion starting from some moment or if the process of conversion into hadrons is essentially a non-equilibrium one.

The expansion of the blob is given in thermodynamical terms. Following the concepts of hydrodynamical models, the final state density $dn/d\eta$ reflects the entropy, whereas the p_t spectrum reflects the combined effects of temperature and transverse expansion of the blob [46].

At equilibrium (before the expansion of the blob) the central multiplicity n is approximately proportional to the total entropy of the system:

$$n \sim \sigma \cdot V \tag{1.20}$$

where V is the volume of the blob and σ its average entropy density. At a fixed reference time, larger σ means larger temperature T ($\sigma \sim T$) at fixed volume. Thus, given an initial collision producing a blob of volume V, we have that higher n indicates hotter hadronic matter:

$$n \sim T \tag{1.21}$$

The time evolution goes as follows. When the initial blob expands, σ and T decrease with $\sigma \cdot V$ approximately constant. At the critical temperature T_C hadronization begins. During the phase transition regime T remains approximately constant while the system continue to expand, until the final state is reached.

The equation of state diagram (σ versus T) will then show an increase of T (i.e. p_t) with σ (i.e. n) except than at phase transition where T (the p_t spectrum) will remain constant. In conclusion the occurrence of a hadronic phase transition in the central blob could be signalled by an anomaly in the variation of $\langle p_t \rangle$ with n [19].

Chapter 2

The Experimental Apparatus

The Tevatron $\overline{p}p$ Collider is currently the world's highest energy particle accelerator. It is the largest in a chain of five accelerators at Fermilab used to produce proton-antiproton collisions at center of mass energy $\sqrt{s} = 1.8$ TeV. The Collider Detector at Fermilab (CDF) was the first general-purpose detector built to exploit physics at the Tevatron. It was first commissioned in 1987. Since then the CDF detector has undergone several upgrades, some of which are relevant to this analysis. The Tevatron and the Collider Detector at Fermilab (CDF) are extremely complex devices and are described in detail elsewhere [48]. However, I will briefly explain the methods for producing colliding beams at the Tevatron and describe those components of the CDF detector which are important to this analysis.

2.1 The Accelerator Complex

The Accelerator Complex at Fermilab (see Figure 2.1) consists of several stages: in each stage protons and antiprotons are accelerated to reach the final energy of 900 GeV in the Tevatron. The acceleration stages consist of:

1. Pre-accelerator (Cockroft-Walton). $\Rightarrow$ 750 keV

2. Linear accelerator. ($length$=150 m) $\Rightarrow$ 400 MeV

3. Booster. ($circumference$=475 m) $\Rightarrow$ 8.0 GeV

4. Accumulator

5. Proton and antiproton injectors

6. Main ring ($circumference$=6.3 km) $\Rightarrow$ 150 GeV

7. Tevatron ring ($circumference$=6.3 km) $\Rightarrow$ 900 GeV

The protons used in the collisions originate from Hydrogen gas molecules (H_2) which are ionized to form H^-. The negative ions are then accelerated to 750 KeV in the Cockroft-Walton electrostatic generator, at which point they are injected into the Linac.

The Linac is a 150 m long series of nine radio-frequency (RF) cavities which produce an electric field that rapidly changes direction. The cavities increase in length in the direction of increased acceleration. This is to provide constant acceleration along the entire length of the Linac.

The ions emerge from the Linac through a carbon foil that strips their outer electrons to leave a pure proton beam.

A RF debuncher is used to minimize the momentum spread of the bunches upon injection into the Booster.

The Booster is an 8 GeV fast cycling proton syncrotron [1] of conventional magnets (used to focus and steer the beam) and an RF cavity (used to accelerate the beams) with a 75.5 meter radius. Once the Booster is filled with bunches, the RF cavity is slowly turned on to capture the beam and the protons are accelerated. At the end of the acceleration process protons leave the Booster with kinetic energy of 8 GeV in bunches of 10^{10} particles and are injected into the Main Ring.

The Main Ring, also a synchrotron accelerator, consists of a 6.3 km string of alternating dipole (bending) and quadrupole (focusing) magnets and a simple RF cavity to boost the protons to 150 GeV.

The Main Ring then injects these protons into the Tevatron.

[1] In a synchrotron a single RF cavity does all the acceleration. The rate of the change of the electric field can be precisely controlled (hence *rapid cycling*) to provide continuous acceleration (a constant field would only provide acceleration once). During the phase when the electric field in the Booster would retard the protons they are in another portion of the ring.

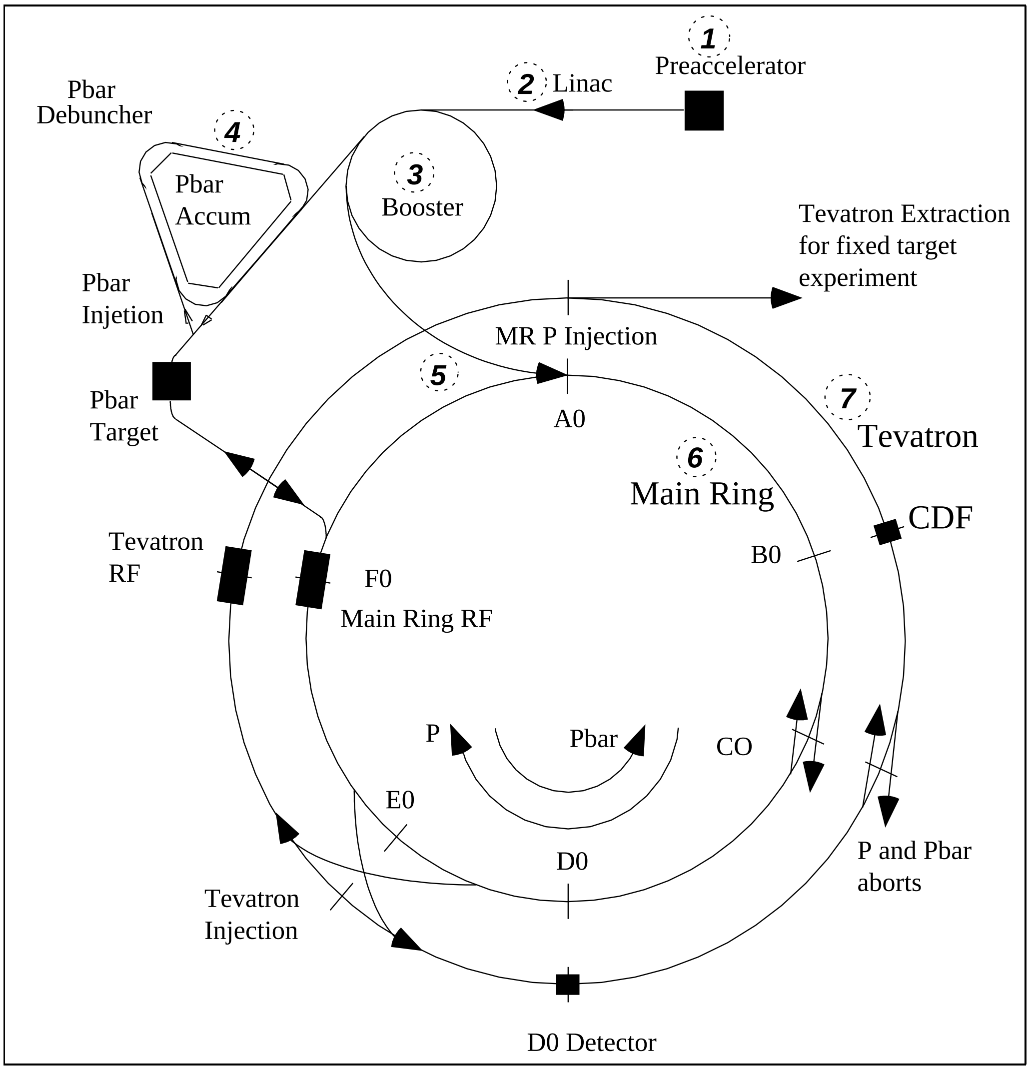

Figure 2.1: Overview of the accelerator complex at Fermilab. H^- ions are injected into the Linac from the Cockcroft-Walton, travel to the Booster, then to the Main Ring, and finally to the Tevatron. Some protons are extracted from the Main Ring and are used to make anti-protons. The anti-protons are re-injected into the Main Ring and then into the Tevatron. The final center of mass energy is $\sqrt{s} = 1.8$ TeV. Note that the Tevatron and Main Ring have the same radius (1 km) and in fact occupy the same tunnel.

During antiproton stacking, the Main Ring also serves as a source of 120 GeV protons to be extracted onto the antiproton source which consists of a nickel target.

Approximately one antiproton is produced for every 10^5 protons striking the target. Antiprotons are collected and stored in the Accumulator Ring, where stochastic cooling is used to reduce their spatial and momentum dispersion. After enough antiprotons have been accumulated, they are re-injected first into the Main Ring to be accelerated to 150 GeV as for the protons, then injected into the Tevatron ring.

Thus, proton and antiproton beams of 150 GeV are injected into the Tevatron from the Main Ring. Like the two previous rings, the Tevatron is a rapid cycling syncrotron, resides in the same tunnel as the Main Ring and has the same radius of about 1 Km. The magnets in the Tevatron, however, are super-conducting: the magnetic field strength (4 Tesla) in the Tevatron is much higher than in the Main Ring and allows to accelerate the beams up to 900 GeV, yielding a 1.8 TeV center-of-mass energy.

The beams circulate for many hours (typically 12-18) during which time the luminosity falls of almost an order of magnitude.

Antiproton stacking continues during Tevatron operation. When the antiproton stack is sufficiently large and the luminosity in the Tevatron decayed, the beam in the Tevatron would be dumped and new bunches would be injected.

In the Tevatron protons and antiprotons bunches are made to collide at two interaction regions, B∅ and D∅, at which are housed Fermilab's two general purpose Collider detectors, CDF and D∅ respectively.

Special superconducting quadrupole magnets called low-beta quadrupoles squeeze the beam at the luminous regions, achieving a roughly Gaussian longitudinal profile with a σ of about 30 cm, and an approximately circular cross section with a radial spread of about 40 μm.

The instantaneous luminosity $\mathcal{L}$ is given by:

$$\mathcal{L} = \frac{fBN_pN_{\bar{p}}}{4\pi\sigma^2} \tag{2.1}$$

where f is the revolution frequency, B the number of bunches, N_p and $N_{\bar{p}}$, respectively, the number of protons and antiprotons per bunch and σ the transverse cross sectional area of each bunch.

During data taking periods (*runs*) from 1992 to 1996 the Tevatron was operated in collider mode with six bunches of protons and six of antiprotons, for a beam crossing every 3.5μs. The istantaneous luminosity was in the order of 10^{31}cm^{-2}s^{-1}.

2.2 The Collider Detector at Fermilab

The Collider Detector at Fermilab (CDF) is a large general purpose detector built to study proton antiproton interactions at the Tevatron collider. It is approximately 27 m long, 10 m high and weights about 5000 tons.

It was designed to measure position, momentum, energy and – where possible – identity of particles emerging from $\overline{p}p$ collisions over as large fraction of the solid angle as pratical. The detector is solenoidal with forward-backward symmetry. Many layers of different detector components surround the interaction region: these subsystems are divided by polar angle in the detector (central, plug, and forward) and by function (tracking, calorimetry and muon detection).

Figure 2.2 shows a side view of the detector.

2.2.1 The CDF Coordinate System

CDF employs a right-handed cartesian coordinate system or, alternatively, a cylindrical coordinate system. Figure 2.3 shows the overall CDF coordinate frame, in both the Rectangular and cylindrical systems. We assume the nominal interaction point to be in the geometrical center of the detector $(0, 0, 0)$ in both of them.

- Rectangular coordinate system:

  z -axis: it lies parallel to the beam axis, positive to the the proton direction.

  y -axis: it points upwards from the plane of the Tevatron.

  x -axis: points radially outwards as shown in Figure 2.3.

- Cylindrical coordinate system:

  ϕ: Azimuthal angle about z-axis, 0 at x-axis, and it increases clockwise.

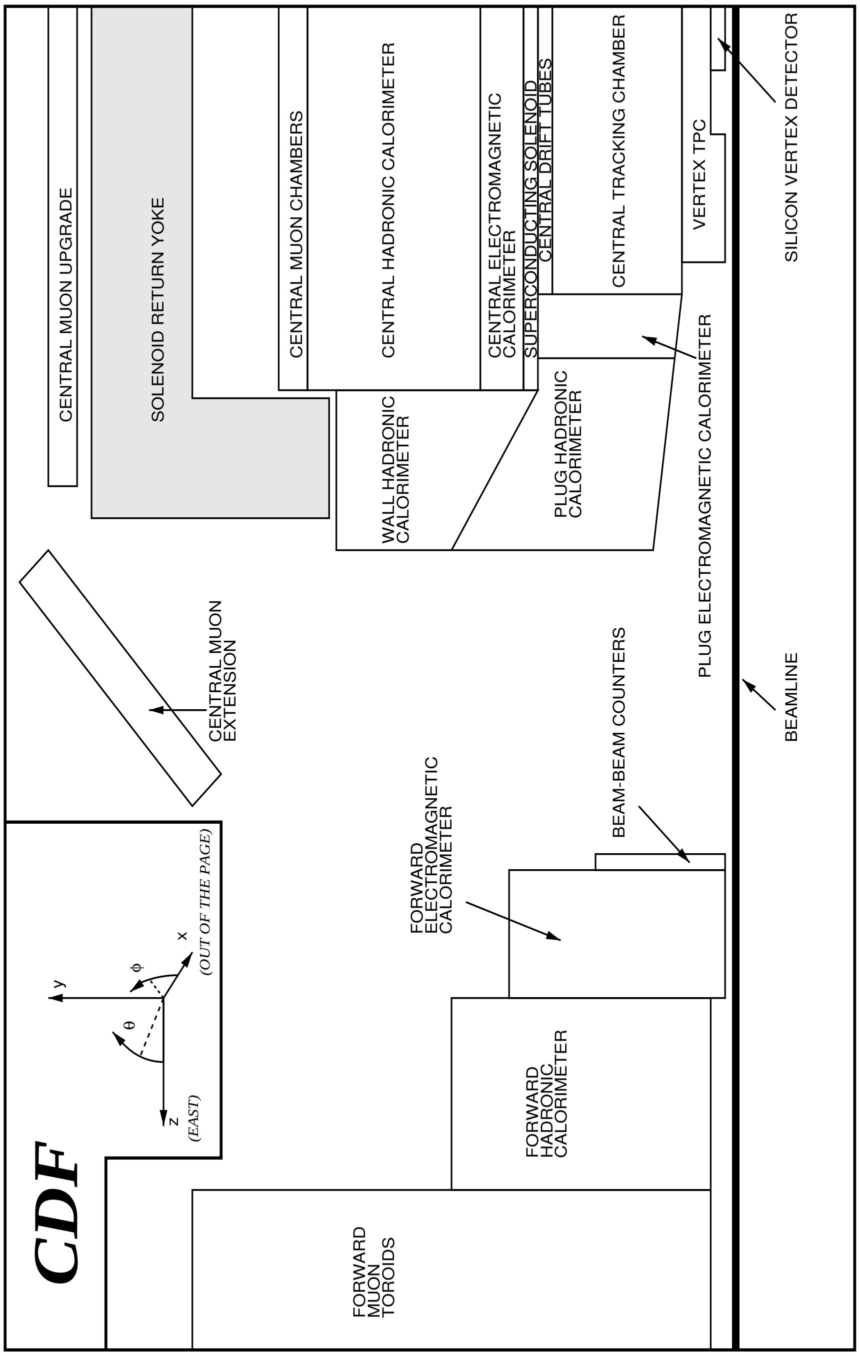

Figure 2.2: Cross section view of one quarter of CDF.

θ: Polar angle relative to z-axis

r: Radial distance from the z-axis.

- Interaction point is at $(0, 0, 0)$ for both coordinate systems.

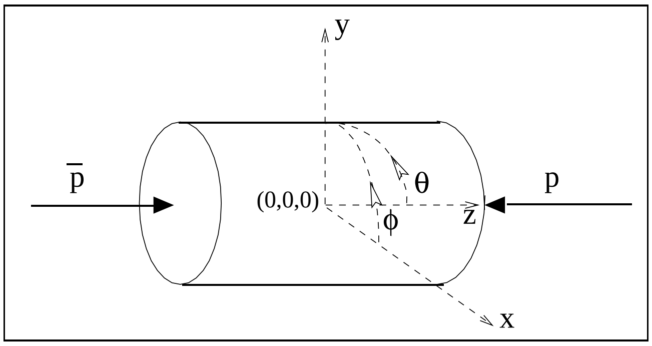

Figure 2.3: The CDF Coordinate System.

Since the incident proton and anti-proton have no transverse momentum and they have equal and opposite longitudinal momentum, the total momentum of the products of the collision would sum to zero in a full 4π solid angle experiment. However, some space must be left for the beampipe. Those particles from the collision that travel at a very small angle, two degrees or less (such as hadrons from the spectator quarks' hadronization), will fly down the beampipe and will thus completely miss all detectors. Such unmeasured particles will not carry away significant amounts of transverse momentum, but they may carry away a significant amount of longitudinal momentum. Because of this effect, longitudinal momentum will not balance in the detector, but transverse momentum will, to the detector's accuracy.

For these reasons, rather than using E (total energy) and p (total momentum), we generally deal with transverse energy, E_t, and transverse momentum, p_t, which can be expressed as follows:

$$E_t = E \times \sin(\theta)$$

$$p_t = p \times \sin(\theta).$$

In the large energies found at CDF, E_t for a particle is nearly equal to p_t. However, we use these variables in a very specific way. We use E_t to describe transverse energy deposited in a calorimeter (so that the angle θ is referred to the origin of the coordinate system), while p_t usually refers to transverse momentum measured in a tracking chamber (so that θ is the angle of the particle).

The “natural” kinematic variables for hadron collisions are pseudorapidity (1.13), transverse momentum (1.8) and azimuthal angle since the shapes of their distributions are invariant [2] under Lorentz boost.

2.2.2 Overview of CDF sub-detectors

A cross section view of a quarter of the CDF detector is shown in Figure 2.4.

Starting from the interaction point and moving out radially particles encounter, in sequence: the thin Berillium wall of the vacuum pipe, the Silicon Vertex Detector (SVX, discussed in section 2.3.1), the Vertex Time Projection Chamber (VTX, section 2.3.2), the Central Tracking Chamber (CTC, section 2.3.3), the superconducting solenoid, the electromagnetic and hadronic calorimeters (section 2.4.1) and the muon chambers. Farther forward, at a smaller angle with respect to the beamline, are the plug and forward calorimeters (section 2.4.2), the beam-beam counters (section 2.5), and the Forward Muon System.

The trigger system will be discussed in section 2.6.

SVX, VTX and CTC form the tracking system. In general, the SVX is used to measure displaced vertices and the VTX to reconstruct the z coordinates of the vertices of interactions. The CTC together with the VTX provides tracking information for charged particles and measures the momentum of charged particles.

The tracking system altogether thus provides charged particles multiplicity and momenta, the position of the event vertex, identification of multiple interactions and calibration data for the calorimeter response.

The physical properties of all of the tracking subsystems are listed in Table 2.1.

The tracking subsystem is embedded in a 1.41 Tesla magnetic field which allow a precise measurement of the momentum of charged tracks. The magnetic field is produced by a superconducting solenoid located just outside the CTC. The solenoid

[2] As already mentioned in chapter one, transverse momentum and azimuthal angle are invariant to Lorentz transformations along the z axis and the pseudorapidity is simply additive.

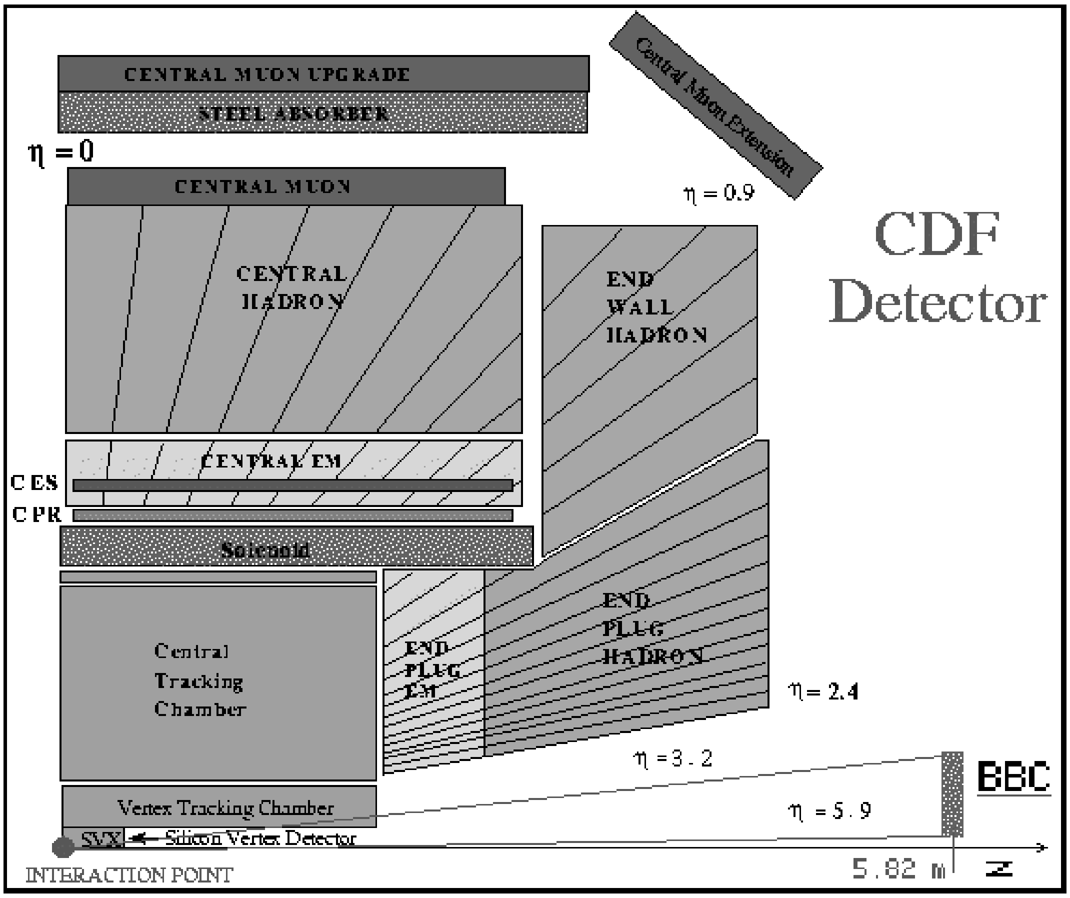

Figure 2.4: A quarter of the CDF detector. Only central and end-plug subsystems are shown.

coil is 4.8 m long, 1.5 m in radius and covers an angular range between 8° and 172°.

The magnetic field flux is returned through a steel yoke. The yoke also functions as a support to the calorimeters located radially outside the solenoid.

Energy measurements of jets, electrons, photons and hadrons are made by the combined calorimetry systems: central, plug and forward electromagnetic (EM) and hadronic calorimeters (HAD).

Table 2.3 briefly summarises the properties of the CDF calorimeter system.

Because of the importance of hadronic jets in $\overline{p}p$ collisions a "tower" geometry was chosen for all the calorimeters. The coverage of the calorimeter towers in $\eta - \phi$ space is shown in Figure 2.9.

Each tower has an electromagnetic shower counter in front of a corresponding tower calorimeter so that detailed comparison of electromagnetic to hadronic energy can be made on a tower by tower basis.

The towers are projective, *i.e.* they point at the interaction region and are 0.1 units in η wide by 15° (central region) and 5° (plug and forward region) in ϕ.

Hadronic calorimeters have a slightly different sharing of the rapidity coverage from the electromagnetics, due to the geometry of the solenoid.

The calorimeters in the central detector consist of the hadronic towers in the wedges and also additional towers in the "endwalls" which are attached to the yoke (see Figure 2.4).

For this analysis we are concerned with the Central and End-Plug calorimeters.

Muons are identified by the presence of a track in the muon chambers matched to a track in the central tracking chamber. A minimum ionizing signal in the calorimeter could be required.

Because of the long lifetime and high penetration of muons, the muon chambers are placed outside of the hadronic calorimeters, after a steel absorber to eliminate any electromagnetic and hadronic showers. Muon chambers in the CDF detector are classified into three parts: the central Muon chamber (CMU), the Central Muon upgrade (CMP), and the Central Muon extension (CMX).

The CMU and CMP cover approximately the regions of $56 \leq \theta \leq 124$, $|\eta| < 0.63$ and about 85% of the ϕ angle, the second being external to the first one.

The CMX consists of four free standing arches and extends the muon coverage from 0.6 to 1.0 in pseudorapidity and has 80% coverage in ϕ.

In front of the backward and forward calorimeters there is a plane of scintillation counters (see Figure 2.4) called "Beam-Beam Counters" (BBC). They provide a minimum bias trigger for the detector and are also used as the primary luminosity monitor.

2.3 Tracking

Before discussing the tracking detectors, we define the track helix parameters.

The trajectory of a charged particle in the uniform magnetic field in the longitudinal direction (z) is a helix whose axis is along z. The projection of the helix in the transverse ($x-y$) plane is a circle. The distance of the point of closest approach to the origin defines the "impact parameter" D_0. The z position at the impact parameter point defines Z_0.

Major physical properties of all of the tracking subsystems are listed in Table 2.1.

Tracking System	Polar Angle Coverage	Radial Coverage(cm)	Length (cm)	Layers	Spatial Resolution(μm)
SVX	$\lvert\eta\rvert < 1.2$	$3.0 < r < 7.9$	30	4	15
SVXP	$\lvert\eta\rvert < 1.2$	$2.9 < r < 7.9$	30	4	13
VTX	$\lvert\eta\rvert < 3.25$	$7 < r < 21$	143.5	24	200-500
CTC	$\lvert\eta\rvert < 1.5$	$30.9 < r < 132$	160.7	60,24	200

Table 2.1: Tracking Subsystem Properties.

2.3.1 The SVX

The Silicon Vertex Detector (SVX) was installed in CDF for the 1992-93 run. It is a silicon microstrip vertex detector located at the most inner part of the detector system, just outside of the beam pipe. Its purpose is to provide precision tracking information in the $r-\phi$ plane in order to measure the displacement of the secondary vertices from heavy meson decay.

Particles emerging from the collision with lifetime in order of 10^{-12} seconds will travel some 300 μm before decaying to secondary particles.

The SVX makes it possible to identify such decay vertices (for example b-quark decays) by a precise measurement of reconstructed tracks. This technique is popularly called *b-tagging*.

The SVX consists of two independent identical barrels laid along the beamline, simmetrically placed about $z = 0$ for a total active length of about 51 cm and a gap of about 2.5 cm between the barrels. Each barrel contains four concentric cylindrical layers of silicon detectors (micro-strips) as shown in Figure 2.5.

Each layer was constructed with twelve flat regions, forming a dodecagon. The flat regions of all four layers are aligned, forming twelve wedges. Layer 0 is at 3.0 cm in radius, up to 7.9 cm at layer 3.

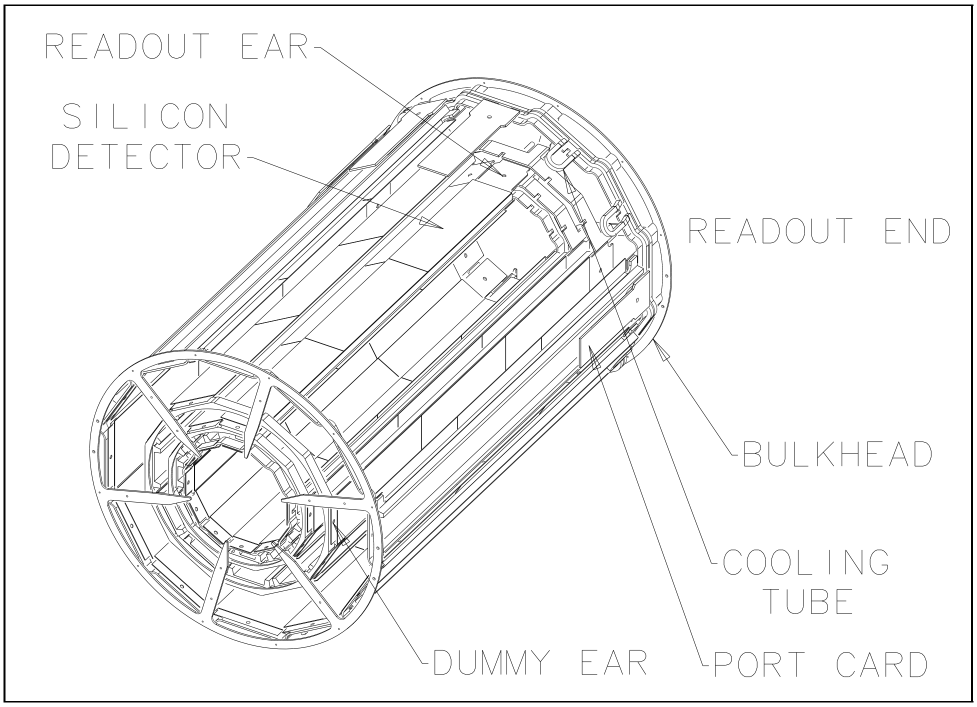

Figure 2.5: View of a barrel of the SVX.

The relevant performance numbers for the SVX are the spatial hit resolution ($\sim$ 13 μm) and the impact parameter resolution ($\sigma_D(p_t) = 13 + 40/p_t$ μm).

Due to its degradation due to a cumulative exposure to radiation, the SVX was replaced by the radiation-hard SVX$'$ for Run 1B. The two detectors are very similar.

2.3.2 The VTX

The Vertex Time Projection Chamber (VTX) is an upgrade of a similar chamber (VTPC) used during the 1988 - 1989 runs and is located around the SVX and inside the CTC. The total outer radius is 22 cm. The VTX is comprised of 28 drift modules filled with a 50/50 Argon/Ethane gas mixture. Each drift module is divided into two drift regions (in z) for a total of 56 drift regions; drift regions are about 5 cm long. Each module is divided into eight octants, each octant covering 45° in ϕ.

The five modules at each end have 24 sense wires in each drift region. The nine internal modules on each side of $\eta = 0$ have 16 sense wires in each drift region. This is because the 18 inner modules have a larger inner radius to allow the SVX to fit inside the VTX. All sense wires are strung azimuthally with eight straight sections, one in each octant. A sense wire plane is placed on each side of the middle of each module so that each drift region has its own sense wire plane. Charged particles drift along the beam toward the center of each module to the sense wires. Each module is tilted 15° relative to its neighbors to provide rudimentary ϕ information for particles passing through two or more modules.

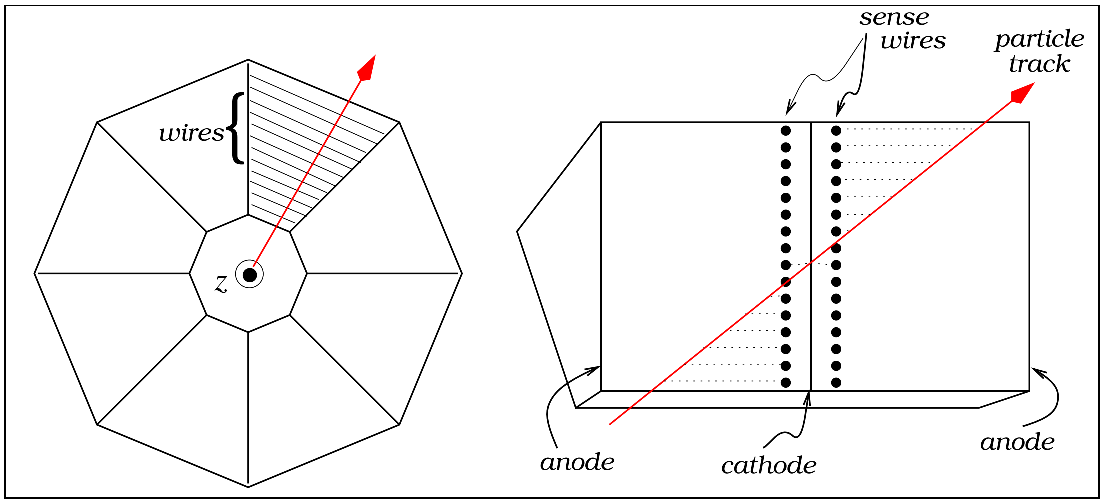

Figure 2.6: Design of a VTX module.

The radial positions of the wires are used in conjunction with the drift times to provide r-z tracking information.

The VTX thus provides two dimensional track reconstruction in the rapidity region of $|\eta| < 3.25$. But it is primarily used to determine the z displacement of the primary vertex of the event by locating the convergence of all the reconstructed tracks in the event.

The knowledge of the location of the event vertex is the starting point for offline reconstruction and is a first order correction in the calculation of some physics quantities such as transverse energy or charged multiplicity.

2.3.3 The CTC

The Central Tracking Chamber is CDF's primary tracking chamber and the only tracking chamber at CDF which measures a full 3-dimensional track trajectory.

It is a 3.2 m long cylindrical drift chamber that fits inside the solenoidal magnet. The outer radius is 1380 mm, the inner radius 277 mm, leaving space for VTX.

The main goal of the CTC is to measure the transverse momentum and determine the sign of charged tracks in the central region (roughly $30° < \theta < 150°$).

However its design was dictated largely by other physics considerations, some of which are relevant to this analysis:

1. maximum drift time shorter than the beam-beam crossing time of 3.5μs;

2. identification and measurement of secondary vertices coming from the decay of long lived particles;

3. measurement of charged particle transverse momenta and multiplicity as a function of rapidity .

The chamber consists of 84 layers of sense wires grouped into 9 super-layers numbered from 0 (the innermost) to 8 (the outermost).

The axial superlayers (layers 0, 2, 4, 6 and 8) consist of 12 sense wires each, arranged parallel to the beam direction. They allow track reconstruction in the $r - \phi$ plane. The stereo superlayers, interspersed between the axial superlayers, have 6 sense wires each, tilted $\pm 3°$ with respect to the axial direction ($+3°$ for superlayers 1 and 5, $-3°$ for superlayers 3 and 7), and enable track reconstruction in the $r - z$ plane. Tracks with hits in the axial and stereo superlayers are termed *3-D* tracks. Layer arrangement is shown in Figure 2.8.

Both axial and stereo superlayers are further subdivided into cells. This results in a maximum drift distance of about 40 mm, corresponding to about 800 ns of drift time. The boundaries of a cell are defined by two planes of field wires. The sense wire plane lies midway between the two field wire planes. Separating each sense wire from each neighbours is a potential wire which is used to control the gas gain on the sense wire. The field wire voltages control the strength of the drift field. Some special wire planes have been added to keep the electric field uniform over the fiducial volume of the cell.

Drift cells are tilted by $45°$ with respect to the radial direction in order to compensate for the Lorentz angle of the drift electrons in the crossed magnetic and electric

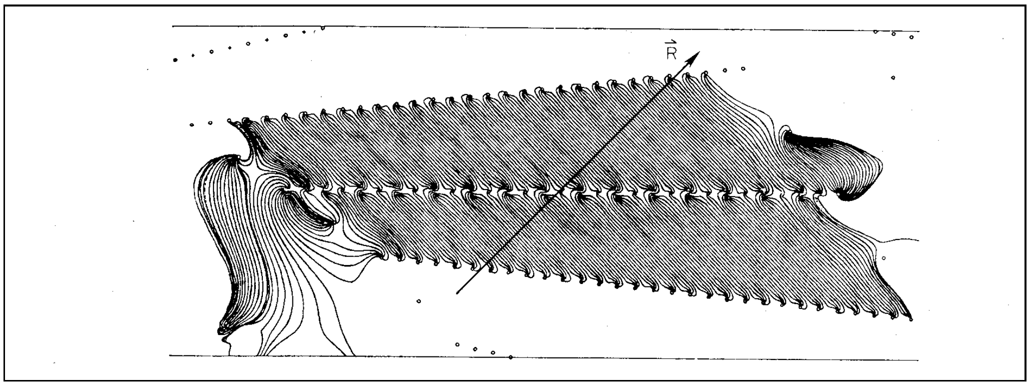

Figure 2.7: Drift trajectories in a 15 kG magnetic field. The radial direction is indicated by the arrow.

Gain	3×10^4 (250 ns gate)
Resolution	<200 μm per wire
Efficiency	>0.98 per point
Double track resolution	<5 mm or 100 ns
Maximum drift distance	40 mm
Maximum hits per wire	>7
Stereo angle	±3°
z resolution	<0.200 mm/sin3°
Momentum resolution	$dP_T/P_T < 0.002 P_T$ (in GeV/c at 90°)
Number of layers	84
Number of superlayers	9
Stereo angle	0° +3° 0° -3° 0° +3° 0° -3° 0°
Number of super cells/layer	30,42,48,60,72,84,96,108,120
Number of sense wires/cell	12,6,12,6,12,6,12,6,12
Sense wire spacing	10 mm in plane of wires
Tilt angle (center of plain)	45°
Radius at innermost wire	309 mm
Radius at outermost wire	1320 mm
Wire length	3214.0 mm
Total number of wires	36504
Gas	argon-ethan-alcohol (49.6%:49.6%:0.8%)
Drift field (E_0)	≈1350 V/cm

Table 2.2: CTC performance specifications and mechanical parameters.

fields (1350 V/cm). This results in a drift direction approximately azimuthal, i.e. perpendicular to the radial direction (Figure 2.7).

Due to the large tilt angle the cells in each superlayer partially overlap. This guaranties that every radial (i.e. high p_t) track must pass close to at least one sense wire in each superlayer. It also helps clearing the right-left ambiguity [3].

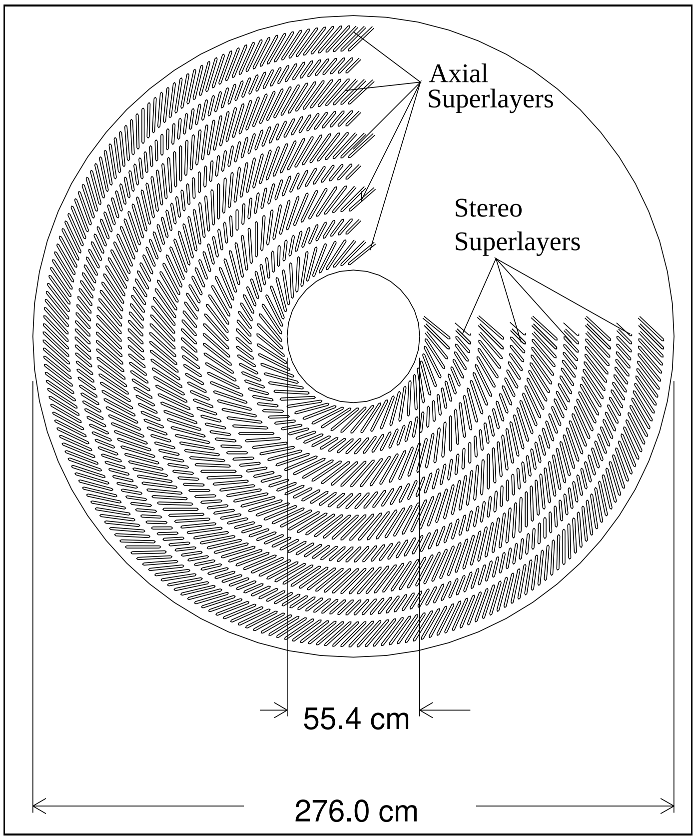

Figure 2.8: The CTC Endplate.

The position of a charged particle at the radius of a given sense wire is determined from the position of the sense wire and the distance corresponding to the drift time measured for that hit. In the plane of the wires, sense wires are separated by 10 mm. The two-track resolution is about 5 mm. The individual hit resolution is about 200 μm, and the efficiency per wire is greater than 98%. The resolution of a stereo wire in the longitudinal z coordinate is approximately $0.2\text{mm}/\sin 3^\circ = 4$ mm.

[3] An ionization electron can approach a sense wire from the right or left, and there is no instrumentation to distinguish between these alternatives. However, with the 45° tilt to the drift cells, only one of these two alternatives will point toward the event vertex for a high p_t track which came from the event vertex.

Track reconstruction in the CTC involves fitting the hits of a track to the arc of a helix and is computed by determining the curvature of the fitted track. The transverse momentum resolution for the CTC alone is $\frac{\delta p_t}{p_t} \approx 0.002 p_t$ at 90°, where p_t is in GeV/c. The impact parameter resolution is in the order of $\sim 200\mu$m.

Tracks with $p_t < 0.275$ GeV/c curl up inside the CTC and do not reach the outer edge.

Performance and parameters of the CTC are shown in Table 2.2.

2.4 Calorimetry

The solenoid and the tracking system of the CDF are surrounded by calorimeters. Their coverage in ϕ is 2π in azimuth and $|\eta|$ <4.2 in pseudorapidity . They are segmented in polar and azimuthal angle to form a projective tower geometry which points back to the geometric center of the detector.

Coverage of the calorimeter towers in $\eta - \phi$ space is shown in Figure 2.9

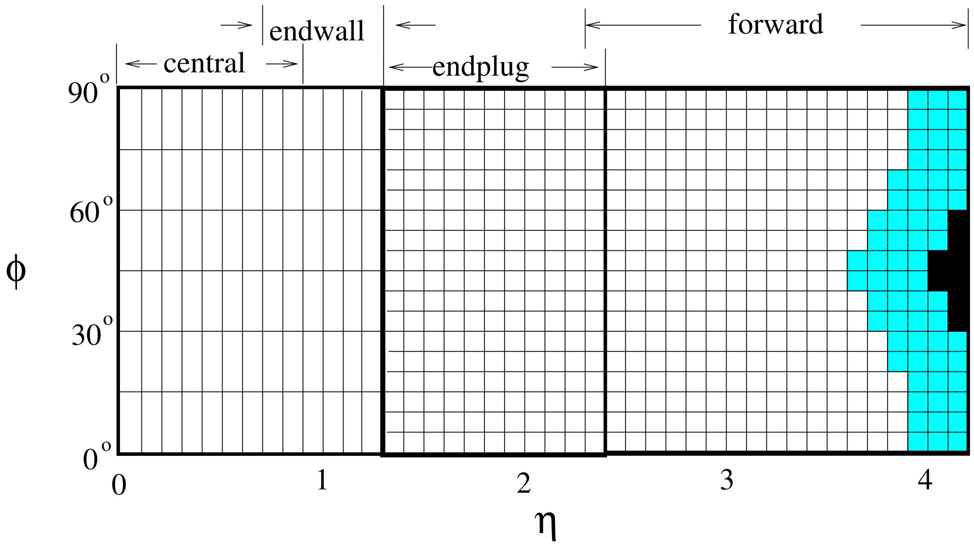

Figure 2.9: Coverage of calorimeters towers in $\eta - \phi$ space. Gray areas indicate partial coverage, black areas no coverage at all.

The CDF calorimeters are symmetric in ϕ and are divided into three regions according to their pseudorapidity coverage: the central, the plug and the forward.

Each region has an electromagnetic calorimeter (CEM,PEM,FEM) followed by a hadronic calorimeter (CHA/WHA,PHA,FHA).

The forward calorimeters have not been used for this analysis.

All CDF calorimeters are sampling calorimeters: they are constructed from alternating layers of an absorbing material and an active material. Electrons loose energy in the absorber mostly through bremsstrahlung, photons mostly through pair production. All charged particles slowly loose energy through ionization and hadrons through interactions with nuclei in the absorber material. At CDF the active layers are scintillating plastic, which measures the energy via the light deposition, and proportional gas tubes which measure ionization produced when the shower passes through the tube.

The absorber in all hadronic calorimeters is iron and in all electromagnetic calorimeters is lead. Table 2.3 summarize the coverage, thickness and resolution of each of the calorimeters.

The CDF hadronic calorimeters are not compensating; their response to π^0's differs from their response to hadronic shower components of equal energy. This accounts in part for the worse performance of hadronic calorimeters compared to electromagnetic ones.

Uninstrumented regions, or cracks, occur every 15° in ϕ, between wedges, as well as at polar angle θ=90° between the east and west arches and θ=30° and θ=10°. Cracks occur between modules, or where cabling or structural support are provided. A particle travelling down a crack will be unmeasured unless it showers and the shower enters a neighboring calorimeter.

The total acceptance loss due to explicit fiducial requirements is 18.7%.

2.4.1 Central Calorimeters

The central calorimeter consists of 48 wedge-shaped modules. It is segmented into two halves in z-plane, divided symmetrically at $\eta = 0$. Each half is segmented into 24 wedges, each covering 15° in ϕ and pseudorapidity range of $0 < |\eta| < 1.1$. Each wedge is divided into 10 towers along the z-axis. Figure 2.10 shows a perspective view of a central calorimeter wedge, with tower numbers marked from 0 to 9.

System	η Coverage	Energy Resolution	Position Resolution	Thickness
CHA	$\|\eta\| < 0.9$	$50\%/\sqrt{E_T} \oplus 3\%$	0.2×0.2 cm	4.5 Λ_0
WHA	$0.7 < \|\eta\| < 1.3$	$75\%/\sqrt{E_T} \oplus 4\%$	0.2×0.2 cm	4.5 Λ_0
PHA	$1.3 < \|\eta\| < 2.4$	$90\%/\sqrt{E_T} \oplus 4\%$	0.2×0.2 cm	5.7 Λ_0
FHA	$2.4 < \|\eta\| < 4.2$	$130\%/\sqrt{E_T} \oplus 4\%$	0.2×0.2 cm	7.7 Λ_0
CEM	$\|\eta\| < 1.1$	$13.7\%/\sqrt{E_T} \oplus 2\%$	0.2×0.2 cm	18 X_0
PEM	$1.1 < \|\eta\| < 2.4$	$28\%/\sqrt{E_T} \oplus 2\%$	0.2×0.2 cm	18-21 X_0
FEM	$2.2 < \|\eta\| < 4.2$	$25\%/\sqrt{E_T} \oplus 2\%$	0.1×0.4 cm	25 X_0

Table 2.3: A summary of the properties of the different CDF calorimeter systems. Energy resolutions for the hadronic calorimeters are for incident pions, and for the electromagnetic calorimeters are for incident electrons and photons (the symbol $\oplus$ means that the constant term is added in quadrature to the resolution). Λ_0 is the interaction length and X_0 the radiation length.

The Central ElectroMagnetic Calorimeter (CEM) is a sampling calorimeter, as each wedge has 31 layers of 3.2 mm thick lead absorber alternating with 5 mm thick layers of plastic scintillator. Plastic light guides take the light from the scintillator to two phototubes per EM tower. The difference in signal pulse height from the two phototubes allows the ϕ position to be determined to an accuracy of 5°.

A hybrid design (scintillators and strip chambers) was used in order to combine the good resolution of scintillator with the fine segmentation of one or more gas layers.

Embedded within the CEM is a proportional strip chamber (CES) to measure the shower position. The CES is inserted in each CEM wedge at a depth corresponding to the maximum average transverse electromagnetic shower development, or the distance at which the greatest amount of initial photon or electron energy is deposited in the shower, about 5.9 radiation lengths. Orthogonal strips (perpendicular to the beam direction) and wires (parallel to the beam direction) measure the shower profile in the η and ϕ directions, respectively. The CES has a position resolution about about ± 2 mm in each view.

The CPR (central pre-radiator) is another set of proportional chambers between the CEM and the CTC that samples early development of the EM showers caused by the material of the solenoid coil.

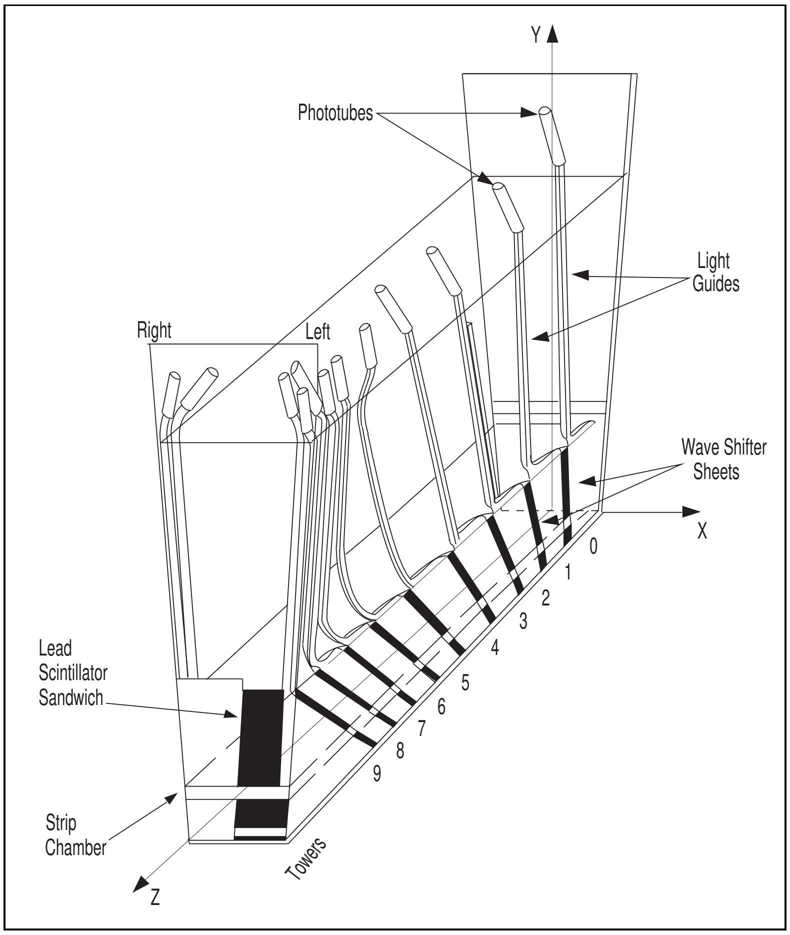

Figure 2.10: Perspective view of a central calorimeter wedge.

The CEM is about 18 radiation lengths [4] and 1.1 absorption length at $\eta = 0$. The overall energy resolution was measured to be about $14\%/\sqrt{E} \oplus 2\%$ with E in GeV.

The central hadron calorimeter systems are used in order to measure the energy of charged and neutral hadrons (mainly pions, kaons and protons).

The CHA covers $|\eta| < 0.9$ and WHA slightly overlap the CHA, covering $0.7 < |\eta| < 1.3$. Towers in the region $0.7 < |\eta| < 0.9$ are shared between WHA and CHA; a particle in this region will first pass through the CHA, then the WHA. Particles

[4] The thickness of an e-m calorimeter is measured in *radiation length* X_0. An average high energy e^- loses all but $1/e$ (e=2.71828) of its energy through bremstrahlung in one radiation length and an average high energy γ has a probability $P = 1 - \exp -7/9 \simeq 54\%$ of converting into a e^+e^- pair. The thickness of hadronic calorimeters is measured in *interaction lengths* Λ_0. Of N neutrals passing through one interaction length, all but N/e will interact with a nucleus in the material.

in the region $0.9 < |\eta| < 1.3$ are only measured by the WHA.

There are time-to-digital converters attached to the hadronic calorimeter components which give the timing information of the deposited energy.

The CHA has 32 layers of 2.5 cm thick steel absorber plates alternating with layers of 1 cm thick plastic scintillator and is about 4.5 interaction lengths thick.

The WHA has 15 layers of 5.1 cm thick steel absorber alternating with plastic scintillator. The steel absorber layers are twice as thick in the WHA, compared to the CHA, because particles of the same E_t going into these calorimeters will have $\sqrt{2}$ times more energy in the WHA. The WHA is about 4.5 interactions lengths thick. For the remainder of this dissertation CHA refers to both the CHA and the WHA.

If the primary interaction occurs in the hadronic calorimeter, the energy resolution is $70\%/\sqrt{E}$ with E in GeV up to 50 GeV and becomes constant at 10% for $50 < E < 150$ GeV. If the primary interaction occurs in the electromagnetic shower counter, the resolution is $65\%/\sqrt{E}$ with E in GeV up to 80 GeV and becomes constant at 8% for $50 < E < 150$ GeV.

2.4.2 End-Plug Calorimeters

Unlike the central calorimeters, the plug calorimeters are divided into 72 wedges in ϕ, each being 5° wide. The plug EM and HAD calorimeters use gas proportional tubes (filled with argon-ethane) with cathode pad readout to measure energy.

The Plug EM calorimeter is built from four azimuthal quadrants which circle the beam pipe. 34 proportional tube arrays are interleaved with 2.7 mm lead absorber. The PEM is about 19 radiation lengths thick.

Its performance is characterised by its energy resolution of $28\%/\sqrt{E} \oplus 2.0\%$. Geometrical position resolution is obtained from its strip size (2 mm $\times$ 2 mm).

The Plug Hadronic Calorimeter (PHA) is constructed from 20 layers of 5.1 cm thick steel interleaved with drift tubes as in the PEM. The PHA is 5.7 interactions lengths thick. It has an energy resolution of $130\ \%/\sqrt{E} \oplus 4\%$.

2.5 The Beam Beam Counters

Two sets of scintillation counters are mounted in front of the forward electromagnetic calorimeters at ±5.82 m in the z direction from the nominal interaction point.

These scintillation counters, the *Beam Beam Counters* (or BBC's) surround the beam pipe and cover the pseudorapidity range 3.24< $|\eta|$ <5.89, that is 0.32° to 4.472°.

Each set has 16 counters, arranged in four rings of four counters each; the radii of the rings range from 3.3 to 47.0 cm. The smallest, innermost, ring sits directly on the Tevatron beam pipe (see Figure 2.11).

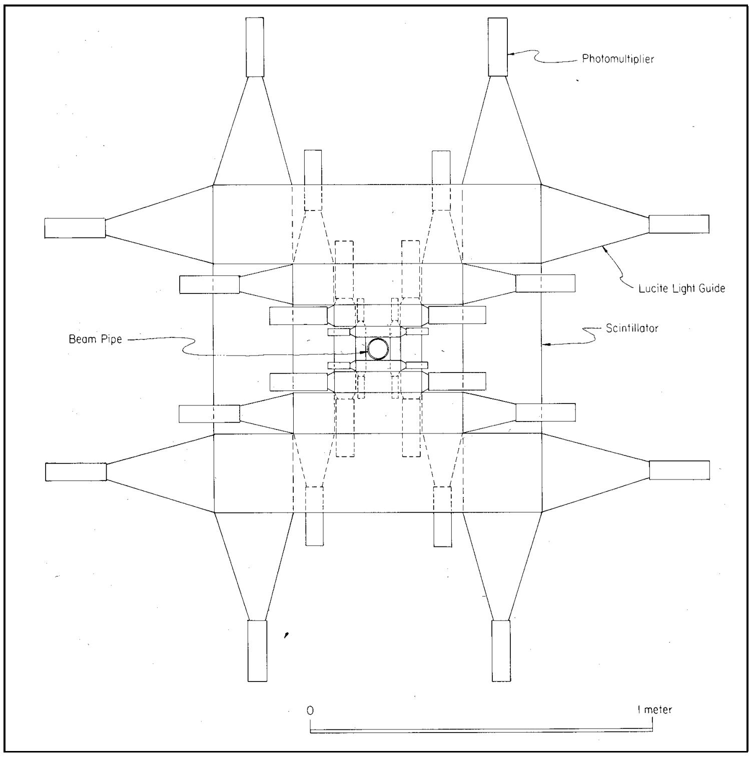

Figure 2.11: A beam's-eye view of one of the beam beam counter planes.

The BBCs provide a minimum-bias trigger, indicating that some inelastic (non-diffractive) $\overline{p}p$ interaction took place during a given bunch crossing. By assigning an estimated inelastic cross-section, the BBCs are also used as a luminosity monitor. Both the luminosity monitor and the minimum-bias trigger require that at least one charged particle hit each set of BBCs in a 15 ns coincidence around the beam crossing time.

2.6 The Trigger System

During Run I the Tevatron was operated with six proton and six antiproton bunches, and $\overline{p}p$ crossing occurred at a rate of about 286 kHz with 3.5 μs between crossings. With a typical istantaneous luminosity of about $10^{31}\text{cm}^{-2}\text{s}^{-1}$ and an assumed inelastic cross-section of 50 mb, we can expect a proton-antiproton interaction rate of

$$R = \mathcal{L} \times \sigma_{inel} \approx 500\ kHz \tag{2.2}$$

that is to say we expect more than one $\overline{p}p$ interaction per bunch crossing, depending on the istantaneous luminosity. It is therefore the bunch crossing rate that defines the maximum rate at which events are produced.

Since the rate at which events can be written to tape is less than 10 Hz, CDF needs to select one event out of about 30000. This is accomplished with the trigger system.

The CDF trigger consists in three decision steps, or levels, each of which imposes a logical "OR" of a limited number of programmable selection criteria that collectively reduce the data rate exposed to the next trigger level. The first two levels consist of specially designed hardware which makes the decision to initiate the full detector readout. The readout of the detector takes a very long time ($\approx$ 1ms) compared to the time between bunch crossings. Therefore it is desiderable to reject as many events as possible *before* fully reading the detector information. In fact it is desiderable to reject as many events as possible during the time between $\overline{p}p$ crossing in order to keep the detector "live" as much as possible.

Lifetime is the fraction of the time that the beam is delivered to CDF during which CDF's trigger is able to consider and process subsequent $\overline{p}p$ interactions. Deadtime wastes delivered luminosity.

The purpose of a multi-level trigger system is to keep deadtime due to readout in the order of 10%.

Level 1. The level 1 trigger is designed to make a decision between $\overline{p}p$ crossings, i.e. in less than 3.5 μs. It thereby causes no deadtime, but is only able to make decisions based on simple detector quantities with no time to group detector information in order to make a more informed decision.

Level 1 decision is based on the following quantities:

- Beam Beam Counters information (this is also called the "Level 0" trigger);
- the electromagnetic, hadronic and total transverse energy E_T, summed over those calorimeter elements which are above a preset threshold;
- transverse energy imbalance in the calorimeters;
- the presence of muons in the muon chambers and the existence of stiff tracks in the CTC.

Level 1 is a hardware trigger implemented with readout of analog signals from subsystems in the CDF detector. Dedicated signal cables communicate a copy of the event information from the front-end electronics to Level 1 and Level 2 triggers.

If Level 1 cannot reject a crossing, the fast analog information is passed to the level 2 trigger for processing. The acceptance rate of level 1 (which is the input rate of level 2) is in the order of few kHz, a reduction of two orders of magnitude from the input rate that corresponds to a Level 1 total cross section $\sigma \sim$100 μb.

LEVEL 2. The level 2 trigger takes about 25-35 μs to make a decision; thus, the next 7-10 crossings are ignored while one collision is being processed and experiment occurs in deadtime. When the level 2 trigger rejects a crossing the level 1 trigger can process the next available collision. When the level 2 trigger accepts a crossing the full detector information is digitized, read out and passed to the third trigger level for processing.

The Data Acquisition (DAQ) takes about 3 ms to digitize and read out the detector information: almost 1000 crossings are ignored while this happens.

Since Level 2 uses more programmable hardware than Level 1 it can cut against physics objects, rather than just detector responses, so to determine basic topological features of the event by considering, with greater sophistication, the same dedicated calorimetry and muon signals used in Level 1. The trigger hardware identifies jet clusters, compute the total E_T and the missing $\not\!\!E_T$ of the event, finds two-dimensional tracks ($r - \phi$) from the Central Fast Tracker (CFT) and matches CFT tracks to clusters.

At level 2 many triggers are prescaled to reduce the total acceptance rates to a maximum of about 20 Hz that is the maximum that Level 3 can handle. This means that a predefined fraction of events that passed the trigger are considered to fail it.

Prescaling is sometimes preferable than making the trigger cuts more stringent and allows to accept as many rare events as possible while still accepting other data at a reasonable rate. Some triggers can be *dynamically* prescaled. A dynamical prescale can be changed during the course of the run depending on the istantaneous luminosity: it will be large when the luminosity is high and small when the luminosity is low.

LEVEL 3. The level 3 trigger makes the final decision whether to reject the event or write onto magnetic tape for later off-line analysis. Unlike the previous trigger levels, Level 3 is implemented in FORTRAN software running on commercially available computer processors, not custom hardware. The Level 3 can process up to 48 events in parallel, taking about 1-2 second for each, and adds no deadtime at a bandwidth up to 20 Hz.

Most of the event reconstruction and filtering code used in Level 3 is the same as that used offline. In order to prevent deadtime, Level 3 does not process all detector data: for example no SVX track reconstruction is performed online.

Level 3 processing consists of two parts: event reconstruction and trigger path processing. Event reconstruction process the raw data into physics analysis quantities such tracks and jets. A trigger path contains a list of analysis and filtering code modules to be executed. Using separate but often overlapping trigger paths, the level 3 trigger searches for electrons, muons, taus, photons, jets, heavy flavors (QCD jets from c and b quarks), exotic physics or physics beyond the standard model. Each trigger in Level 3 is implemented as one path which is independent of every other trigger path. Once event reconstruction is completed each trigger path is executed. An event which passes *any* Level 3 trigger path is accepted and written to 8 mm tape.

Control System. The control of the reading of events, detector calibration and hardware diagnostics is done by a computer process called “Run_Control”. During physics data acquisition a single Run_Control process manages the DAQ hardware and the data flow.

Between data runs calibration processes measure pedestal effects and gains for the calorimeters, and constants for other systems. The data are then stored in large data bases, where they can be extracted at the start of each data run for downloading to the detector subsystems. Other data bases have been created for storing data on external run conditions, integrated luminosity etc.

Chapter 3

Data Selection

This chapter presents the event selection from the CDF Run 1 data set. First the data set and the data reduction process are described. Possible sources of inefficiencies and background are outlined. The last part is dedicated to a MonteCarlo study of the overall efficiency in the detection of minimum bias data.

3.1 Data sample

CDF recorded data from the Tevatron running in $\overline{p}p$ colliding mode at `c.m.s.` energy of 1800 GeV and 630 GeV from 1992 to 1996. This period, which is generally known as Run 1, comprises three separate data-taking intervals: Run 1A (Aug. 1992 – May. 1993), Run 1B (Jan. 1994 – Jul. 1995) and Run 1C (ended Feb. 1996). Only for a short period during Run 1C the Tevatron was operated at the energy of 630 GeV.

A total integrated luminosity of about 130 pb^{-1} was collected and written to tape, corresponding to about 80 million events.

In table 3.1 is reported the cumulative integrated luminosity delivered by the Tevatron to CDF and the amount logged to tape.

A good run list was obtained [49] by requiring all run conditions (high voltages, temperatures, currents, fields) to be near the nominal values and that the beam conditions were normal. Test runs and non-physics runs were removed.

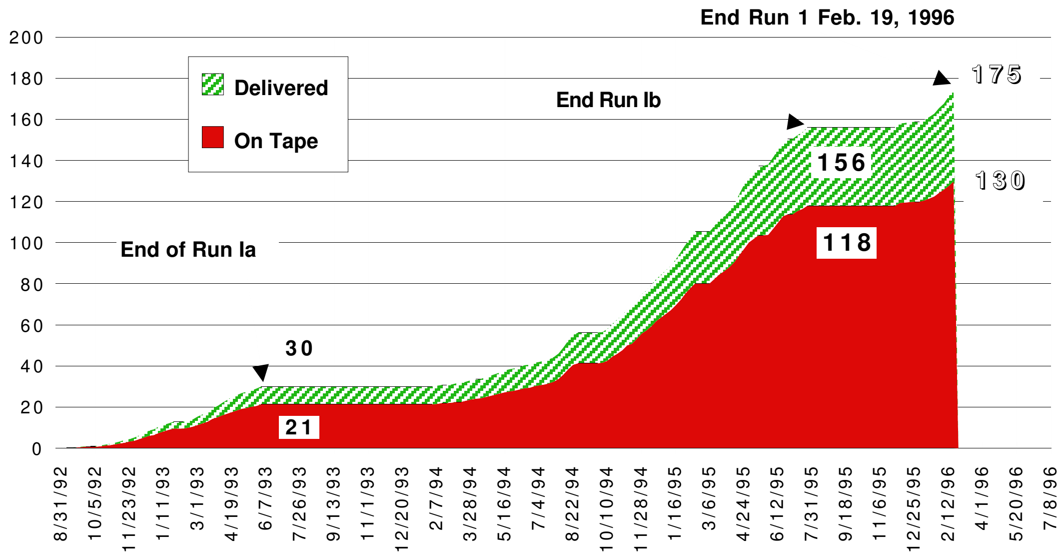

Figure 3.1: Integrated luminosity delivered by the Tevatron and logged to tape (pb^{-1})

About 1.7 million events were written into the Run 1A min-bias data stream (MBO1_3F, 1800 GeV), about 1.5 million into the Run 1B min-bias data stream (XMBB_5F, 1800 GeV), about 0.1 million into the Run 1C min-bias data stream (XMBB_6F, 1800 GeV) and about 2.6 million into the min-bias Run 1C data stream (MBSB_6F, 630 GeV).

The main difference in running conditions between Run 1A and 1B were the upgrade of the SVX and the higher luminosities attained by the Tevatron. Minor improvements in the software and changes in the trigger tables were introduced.

3.2 The Minimum Bias Trigger

At CDF minimum bias data were collected with a trigger (called YMON) which requires that at least one particle transverse each set of the BBC in coincidence with the beam-beam crossing [1]. During Run 1A a prescale was imposed and set to about 10^6. During Run 1B a dynamical prescale was used. The collected event sample is

[1] For a limited time during Run 1A a trigger started by the beam-beam crossing signal has been implemented. Data collected with such trigger are not included in this analysis,although they have been for comparisons and cross-checks.

a mixture of diffractive and inelastic non-diffractive interactions from beam-beam collisions, along with a negligible contamination of beam-gas interactions.

	1A	1B	1C
$\mathcal{L}$ delivered (pb^{-1})	~30	~126	~19
$\mathcal{L}$ written (pb^{-1})	~21	~97	~12
$\mathcal{L}$ good runs (pb^{-1})	~20	~86	~8 (1800) <1 (630)

Table 3.1: Integrated luminosities in Run 1.

3.3 Offline Reconstruction and Filtering

From the Level 3 trigger system to the final selection at the physics analysis stage, several iterations of data processing and reduction occurred. The various algorithms applied at each stage work on a event-by-event base.

Events that passed all the trigger levels are stored on raw data tapes that are successively processed through offline reconstruction and filtering, a process known as *production*. The energy in the calorimeter is measured in terms of the ADC counts of each calorimeter electronic channel. ADC counts are converted to energy with the use of detector dependent scale factors and calibration constants.

Full tracking is done, including the information from the SVX. Any known problems with the data are also corrected at this stage.

After reconstruction the events are split into the different streams of related triggers. The production process outputs two different formats for each data stream: Data Summary Tapes (DST) which includes all the original raw detector information plus the reconstructed event data, and the Physics Analysis Dataset (PAD) which contains only the reconstructed data and compressed information about the detector.

The use of PAD data results in some loss of precision on low-momentum tracks and low-energy towers. Only the DST format has been used for this analysis.

Since the complete set of DST's from minimum bias stream consists of some hundreds double density hexabyte tapes, a final reduction stage was applied to reconstructed data. Events that passed the offline cosmic rays filter (see next subsection) were stored in NTUPLEs (RZ format files) containing –in a more elaborated form– only the information strictly needed for the physics analysis. Up to 800 events were stored in each ntuple, for a total of 8.227 files and 1.712.277 triggers from Run 1A, 1.525.703 from Run 1B, 106.121 from Run 1C at 1800 GeV and 2.575.643 from Run 1C at 630 GeV.

3.3.1 Cosmic Rays Filtering

Cosmic rays passing through the detector can give large energy deposits in the calorimeter and fake the energy measure. They can also pass inside the CTC and get included in the track list.

However, in general, these energy deposits will occur out of time with respect to a $\overline{p}p$ collision and the tracks they produce in the CTC will not point to the event vertex. Similar properties hold also for beam-gas interactions in the beampipe.

An offline cosmic rays filter (COSFLT) which reject such events is executed in the reconstruction path.

COSFLT first tries to reject cosmics that do not coincide with a bunch crossing by examining the out of time energy in the central hadronic calorimeters. The timing information is given by the time-to-digital converters (TDC) attached to the CHA. TDC hits in towers with more than 1 GeV of hadronic energy are checked for whether they are in time with a bunch crossing using a time window of $-20< t <30$ ns. Since timing information is only available for central calorimeters the COSFLT cuts only applies to cosmics in the central region.

3.3.2 Primary Vertex Reconstruction

Offline reconstruction of primary vertices location begins by identifying track segments in the VTX. The segments that meet some basic criteria are combined to form vertices positions: the z-coordinate of a vertex is found by maximizing the number of track segments intercepts in a window 1.5 cm wide. A mean z value of the intercepts is found; the program then iterates until the mean value of all the intercepts within ± 1 cm from the first mean converges.

If no VTX segments are found BBC time of flight information is used. BBC timing resolution is in the order of $\approx$ 200 ps and enables them to determine the position of the event vertex to within 10 cm by computing the time difference between the two counter sets.

All vertices are marked according to the number of hits and segments associated with the vertex, and are given a "class" number ranging from 5 (worst, non $\overline{p}p$ vertex) to 12 (best, high multiplicity vertex). Primary vertices are then identified looking both to the total number of segments and to the forward-backward asymmetry (*shape* of the vertex). The exact criteria for vertex identification and classification are given in [50].

The distribution of primary vertices is gaussian with a width $\sigma_z \simeq$30 cm.

The primary vertices finding efficiency is strongly dependent on the quality of the vertex. Probability to be a real primary vertex for vertices classified as second best primaries is: 98%±2% for class 12, 79%±5% for class 11, 60%±18% for class 10, 50%±18% for class 8, 50%±50% for class 7 and only 33%±33% for class 5 vertices.

Primary vertices classified in the lower class originate from beam-gas interactions and should be rejected in physics analysis. The position of each vertex may be used to compute the parameters of the tracks associated with it. The event vertex is also used to determine the polar angle θ of each calorimeter tower.

The resolving power for two close primary vertices is $\approx$ 6 cm.

3.3.3 Track Finding

Raw CTC information, consisting of drift times for individual wires, are first converted to distances which are then grouped together using a pattern recognition algorithm. A helix is fitted to hit distances and their errors.

Track finding is started by looking for a track segment ("seed") in an outer axial superlayer of the CTC. When a seed is found it is extended to inner axial superlayers forming a 2-dimensional track object in the $r-\phi$ view. Track candidates for fits are required to have at least four hits in each of at least two axial CTC superlayers and at least two hits in each of at least two stereo CTC superlayers.

Stereo reconstruction then takes place beginning from the outermost axial superlayer of the $r-\phi$ track. The VTX provides the initial information on the Z_0

helix parameter of the track. Final $r - \phi - z$ tracks are required to have at least 7 hits from stereo layers and 16 hits from axial layers.

The helical trajectories of such tracks are extrapolated back into the SVX where associated hits are sought using a road algorithm. If a sufficient number of SVX hits is found, the track is refitted using all of the relevant SVX, VTX and CTC information. SVX track segments which are not linked to CTC tracks are ignored.

Tracks with momenta $p_t < 250$ MeV/c were not reconstructed in the production stage of data of data reduction process.

The combined SVX+CTC system resolution when the SVX track fit constraint is required, is

$$\frac{\delta p_t}{p_t} = \left[(0.0009 p_t)^2 + (0.0066)^2\right]^{\frac{1}{2}} \tag{3.1}$$

3.4 Event Selection

The main goal of the event selection was to remove the contamination of non $\overline{p}p$ interactions (beam-gas or beam-wall interactions) and to ensure good tracking efficiency conditions.

The following event selection criteria were estabilished:

1. all events were required to pass YMON trigger at level 2 (minimum bias trigger);
2. all events were required to pass COSFLT filter (cosmic rays rejection);
3. to ensure maximum tracking efficiency the event vertex z position was required to be within ± 60 cm from the origin of CDF coordinate system;
4. events with one (or more) tracks of p_t >50 GeV/c were rejected;
5. main event vertices of lowest class (class 5) mostly originate from beam-gas interactions and were rejected;
6. the event vertex was chosen to be the “best” primary vertex. A full description of the event vertex selection is given in section 3.4.1. In order to suppress multiple interactions, events with a second primary vertex within ± 60 cm from the main event vertex were rejected.

	1800 (1A+1B+1C)	630 (1C)
triggers	3344101	2575643
selected trigs.	2270453	2039451
events (tracking sel.)	2333372	2053117
events (calorimeter sel.)	2080287	1982712

Table 3.2: Triggers and selected events.

After these selections our minimum bias data set contains 2.259.043 beam-beam interactions at 1800 GeV and 2.023.328 at 630 GeV. Since in a few cases (<3%) two "good" events (that is: accepted event vertices) can be found in the same beam-beam interaction, we select in our final sample 2.321.962 events at 1800 GeV and 2.036.994 at 630 GeV.

More and different conditions were needed when the measure of the transverse energy was employed. These cuts are described in detail in chapter 5.

3.4.1 Multiple Interactions and Vertex Selection

Whereas in Run 1A the average number of primary vertices in a given bunch crossing was ~ 1.6, in Run 1B an average of ~ 2.9 primary vertices was present.

The presence of other primary interactions close to the main event vertex may affect the tracking reconstruction and has to be suppressed. Unfortunately, the ability of the reconstruction code to distinguish low-quality primary from secondary vertices is very poor: $\leq 60\%$ for class 10 and lower.

In figure 3.2 is shown the distribution of second best vertices position along the beam axis: for best quality vertices (classes 11 and 12) the distribution is roughly gaussian within ± 60 cm from the nominal interaction point, while it is almost flat along z for vertices of all other classes.

Since events with higher multiplicity have a higher probability of making a secondary interaction which can fake a primary interaction, the exclusion of such interactions would introduce a strong bias in the computation of the event multiplicity, rejecting mostly events of high multiplicity.

For this reason it was decided to cut only on those multiple interactions which are due to a high quality vertex (classes 11 and 12) for which the probability of

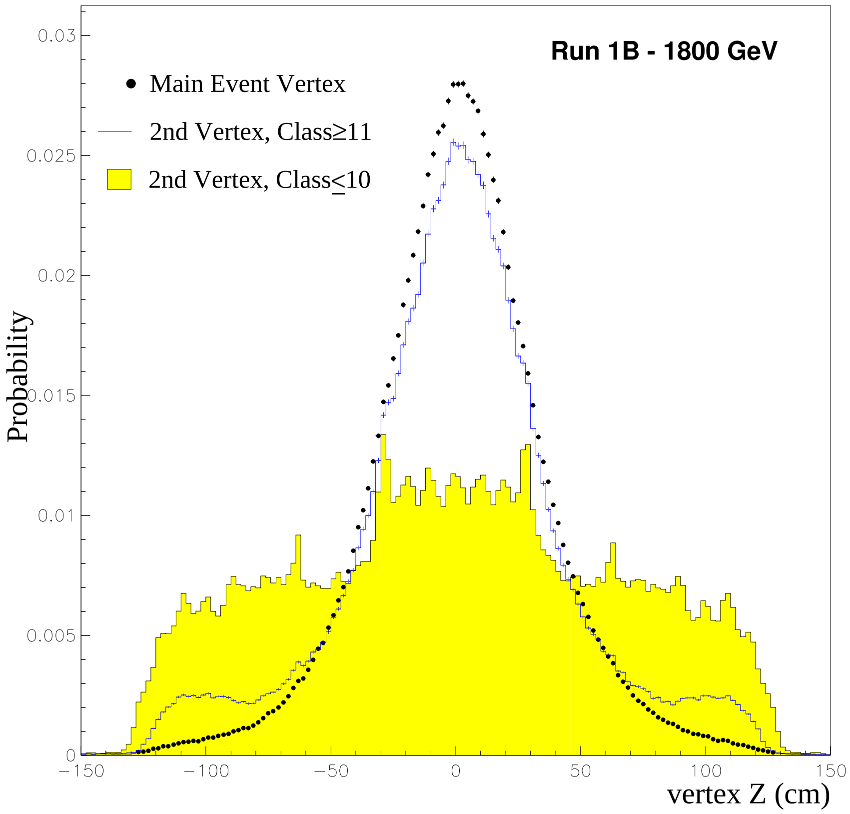

Figure 3.2: Second best vertices position distribution along the beam axis for multiple interaction events. Filled area represent lower quality vertices, continuous line high quality vertices. Full dots are for the main event vertices.

being a "real" primary vertex is greater than 80%.

The final algorithm for vertex selection works as follows:

- the "best" vertex within ±60 cm from origin is chosen;
- if two high quality vertices (classes 11 and 12) are present in the same beam-beam interactions, both within ±60 cm from origin, they are both held and two events are computed out of the same trigger;
- if three (or more) high quality vertices are found in the ±60 cm confidence window centered on origin, the interaction is rejected;
- if one (or more) high quality vertices is found outside this window, and only low quality vertices inside, the interaction is rejected;
- if only low quality vertices are found, only the "best" one is held and the others are considered secondary vertices;

- finally a check for multiple interactions is done: if other high quality vertices closer than 60 cm from the selected one(s) are found, the trigger is rejected.

3.5 Track Selection

Since the track finding algorithm has very loose requirements, further quality controls with tighter cuts were needed to reduce the backgrounds arising from poor measurements in the CDF detector.

The loss of good tracks due to the track selection was negligible. The following cuts were applied to tracks:

Track quality cuts. Minimal conditions are imposed to the quality of the fit and to the number of wires and layers hit in the CTC (CTCSEL quality cuts).

Secondaries removal. Non primary particles resulting from decays of secondary interactions have large impact parameter with respect to the beam axis and are not associated with the z position of the event vertex. To reject these tracks two conditions are applied:

1) track impact parameter $d_o = \left|\sqrt{x_o^2 + y_o^2} - c\right| \leq 5$ mm (where the coordinates x_o and y_o define the transverse location of the center of the helix and c the curvature radius).
2) the distance between the point of closest approach of the track to the z axis and the position of the event vertex (track Z_0 intercept) was required to be $Z_0 \leq 5$ cm.

CTC acceptance cut. A final cut was imposed to ensure optimal CTC acceptance and maximum efficiency. Only tracks within the following phase space region were accepted:

$$|\eta_{track}| \leq 1.0 \tag{3.2}$$

$$p_{ttrack} \geq 0.400 \quad GeV/c \tag{3.3}$$

3.6 Physical Backgrounds in CTC measures

Tracking systematics have been intensively studied at CDF [51] and possible sources of tracking errors have been outlined.

Effects of photon conversion, secondary interactions and decays of neutral strange particles increase the number of reconstructed tracks. Using the impact parameter distribution of pions coming from K^0_S decays, the fraction of secondaries from strange particles was estimated [57] to be about 2.4% of the observed charged multiplicity. An upper bound to this plus other effects (such as decay products of charged hadrons) can be set to $3.0 \pm 1.0\%$ in the region of $|\eta| < 1.0$, nearly independent of p_t for $p_t > 0.4$ GeV/c. A cross-check with MonteCarlo technique gives similar results (section 3.8.1).

Decays in flight of charged pions and kaons have been evaluated to cause a depletion of inclusive distributions in the central region ranging from about 5% at $p_t = 0.4$ GeV/c to about 2% at $p_t = 2$ GeV/c.

The overall correction is very close to one and is nearly independent of p_t for $p_t > 0.45$ GeV/c.

The analysis of the error introduced by the primary vertex selection is described in section 4.2.1.

3.7 Reconstruction Efficiency and CTC Acceptance

Since charged particles with $p_t < 0.33$ GeV/c spiral inside the solenoid and the track finding criteria were optimized for high p_t tracks to avoid misreconstructions due to these spirals, the pattern recognition efficiency drops rapidly for p_t below 0.4 GeV/c. Above this value efficiency was studied as a function of several different kinematic variables. No significant dependence of the pattern recognition efficiency on the azimuthal angle and pseudorapidity was observed in $|\eta| < 1.0$.

A study with the technique of embedding a Montecarlo simulated track into data [52] shows that, for the CTC, an exit radius criterion of $r^{exit}_{CTC} > 110$ cm (corresponding to the outer edge of superlayer 6) ensures that the track is in a region of well-understand pattern recognition efficiency without undue compromise to the CTC fiducial acceptance.

The bulk of the CTC tracking inefficiency is found to be due to occupancy effects alone. An analysis as a function of the total number of tracks in the CTC (not only the tracks pointing to the event vertex) show the efficiency to be decreasing at higher multiplicities, but to be always greater than $\sim 90\%$ in the worst conditions. These conditions are found frequently at the end of Run 1B when the instantaneous luminosity was very high.

3.8 Montecarlo Simulation

A Montecarlo event generator was used to simulate minimum bias data and estimate an overall detection and reconstruction efficiency.

The primary event generator simulates the desired interaction and stores, for each particle of the process, the full event information including the complete decay chain, particles 4-momentum, position, and parent and daughter pointers.

This information forms the input for subsequent detector simulation which usually ends into a raw data format storage analogous to that output from the CDF detector. Simulated data are then passed through the production process and are reconstructed just as $\overline{p}p$ data.

Version 5_7 of the PYTHIA Montecarlo generator [53] was used to simulate a minimum bias sample. About 320.000 events were generated both at `c.m.s.` energy of 1800 GeV and 630 GeV.

The default minimum bias configuration was used. A few parameters were adjusted to best match the measured CTC multiplicity distribution and transverse momentum spectrum. Reset parameters are related to multiple parton-parton interactions and to the $p_{t_{min}}$ cut off (section 1.8.1). For the details of the tuning see appendix 1.

A fast simulation (QFL [54]) of the detector was used. Unlike other simulation packages such as CDFSIM, which trace an evolution of each particle through the detector based on first physics principles, QFL philosophy is to paramatrize the detector response.

These parametrizations are tuned to the data, either from $\overline{p}p$ collisions or from calibration runs of the various detector components in test beam experiments. QFL produces a high level output which need not be reconstructed and allows a considerable savings of CPU and solar time. For simplicity from now on we will use *reconstructed* for *simulated through QFL fast simulation*.

3.8.1 Efficiency and physics backgrounds

Detection and reconstruction efficiency is determined by comparing Pythia generated distributions to the corresponding reconstructed distributions. The effect of the decay in flight of charged hadrons is considered. The ratio of reconstructed versus generated data is plotted, in figure 3.3, 3.4 and 3.5 as a function of p_t, η and multiplicity.

For tracks with p_t >0.4 GeV/c and η <1.0 tracking efficiency is very good (on average greater than 98%), independent of η and ϕ. A weak dependence on p_t can be observed for 0.4< p_t <0.5 GeV/c. As a function of multiplicity the efficiency drops down to about 90% for events with more than about 20-25 tracks in the limited acceptance phase space region of the CTC. It should be noticed, however, that the statistical error is very high due to poor Montecarlo statistics. The small effect (<1%) of over-efficiency in the first bins in multiplicity (charged multiplicity $\leq$3) is due to the reconstruction code.

In addition to the reconstruction efficiency the observed inclusive distributions are affected by various physical backgrounds whose contribution was studied in the region p_t >0.4 GeV/c and $|\eta|$ <1.0 Altogether such contributions were estimated to be about 5%.

The effect of tracks originating from the decays of neutral particles and from gamma conversion was estimated to be, respectively, about 3.5% and 0.5%. Decays of neutral particles are almost solely due to hadrons containing a strange quark (mostly K^0_S). Decay products of charged particles are found to contribute for less than 1% to the measured charged multiplicity.

The overall contribution of the above systematics is flat in η, ϕ and multiplicity, and only weakly dependent on p_t.

The average effect of all corrections on the inclusive distributions was to decrease the measured number of particles of about 2%.

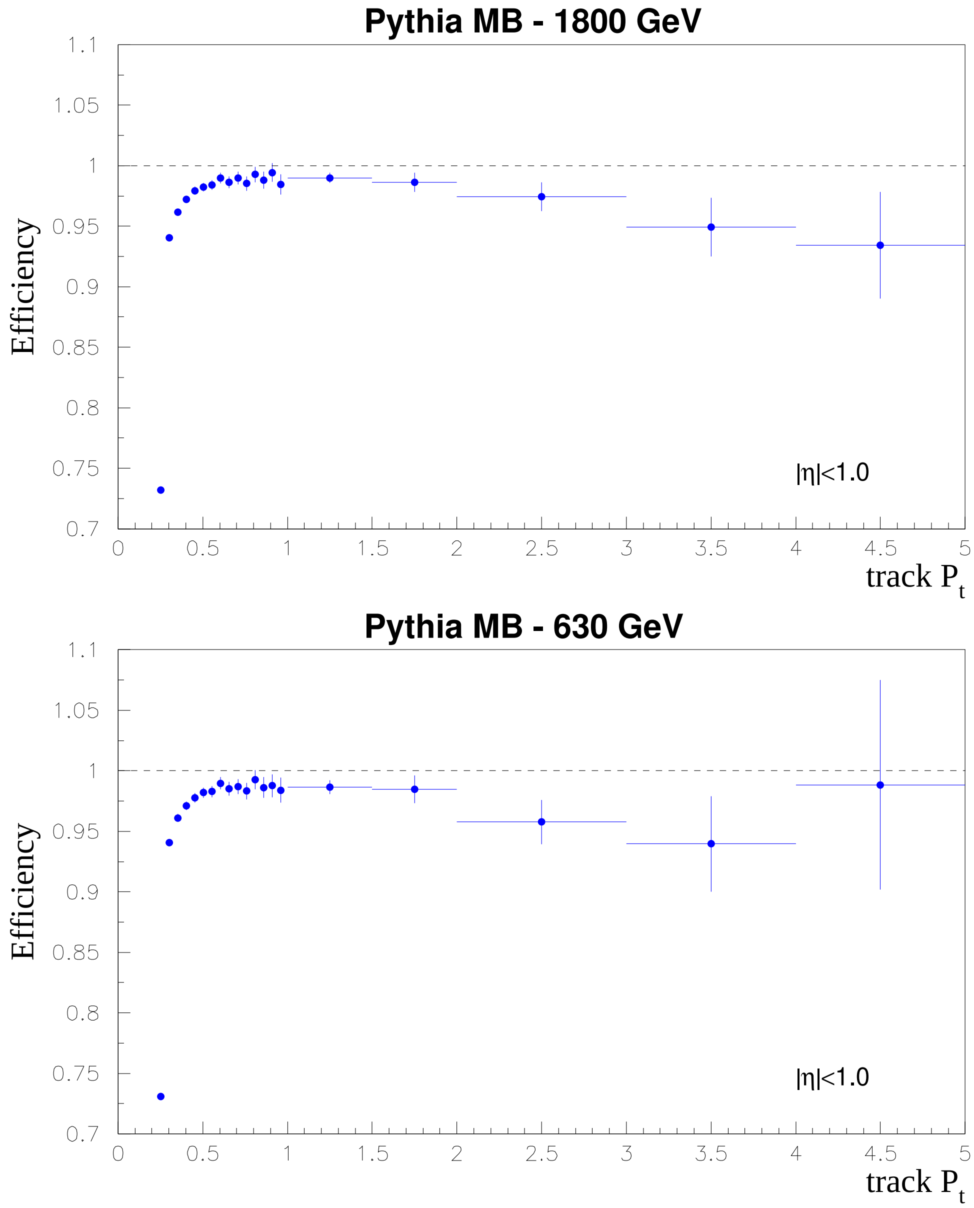

Figure 3.3: Efficiency versus the track transverse momentum p_t at 1800 and 630 GeV. Efficiency is computed as the ratio of reconstructed over generated number of tracks in each bin of p_t.

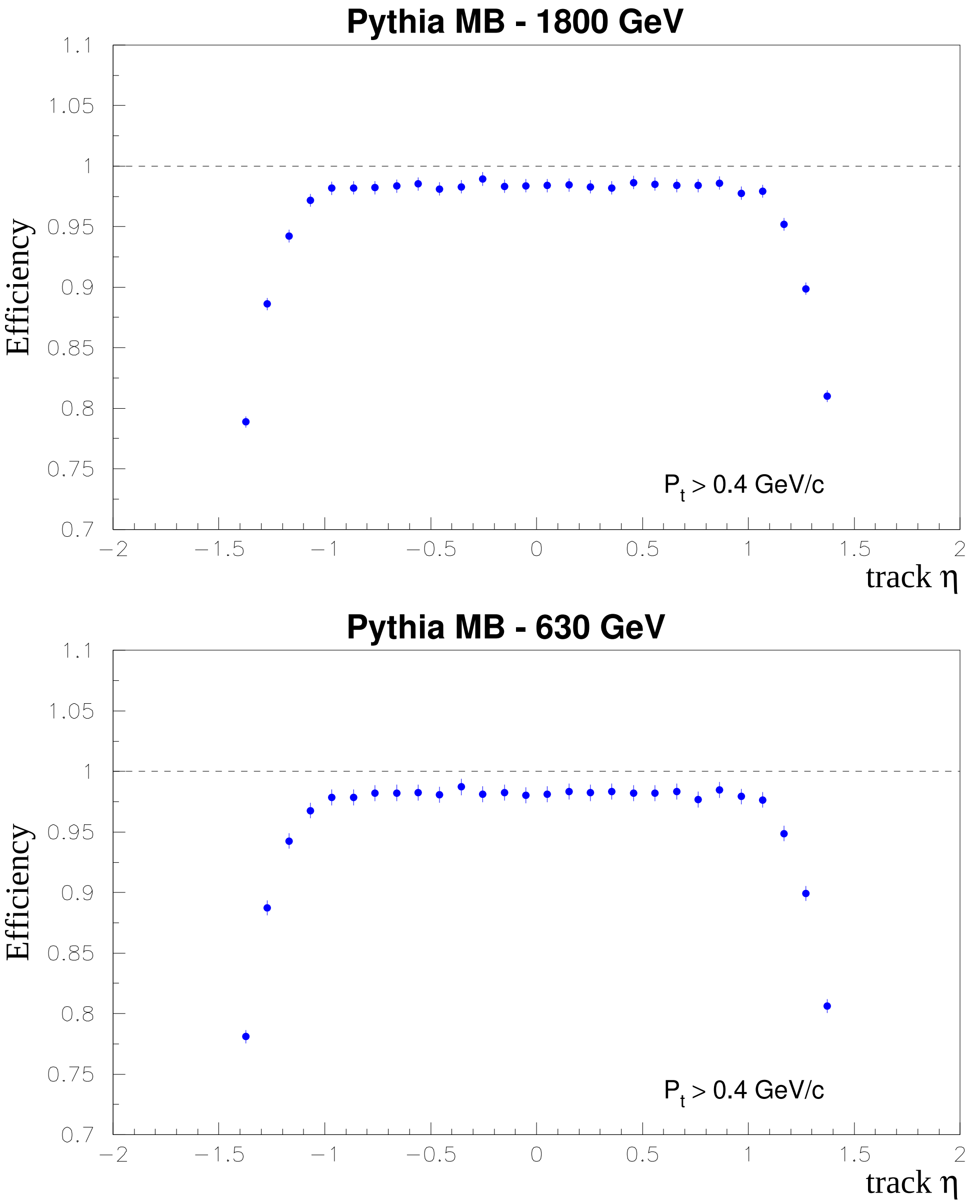

Figure 3.4: Efficiency versus track pseudorapidity at 1800 and 630 GeV. Efficiency is computed as the ratio of reconstructed over generated number of tracks in each bin of pseudorapidity.

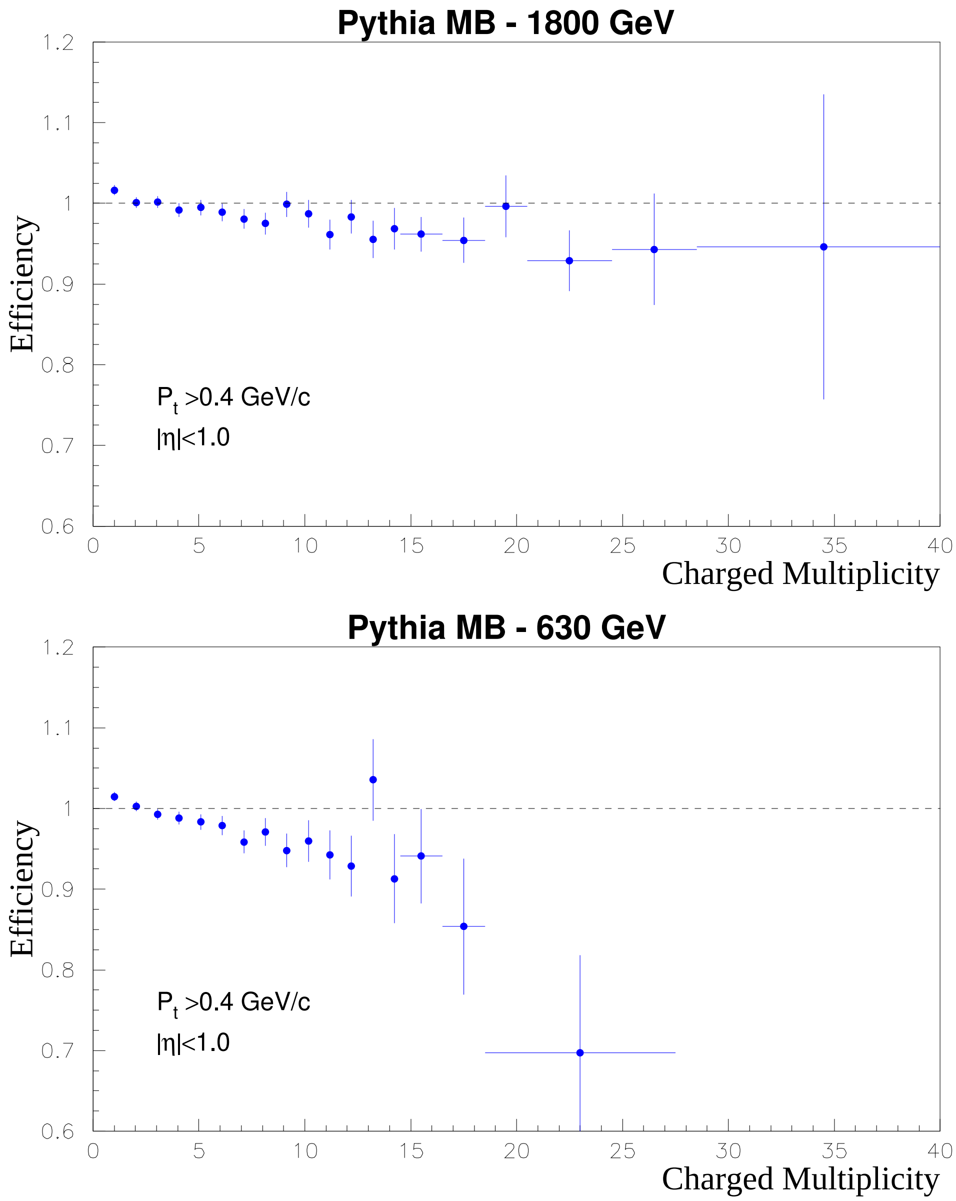

Figure 3.5: Efficiency versus the charged multiplicity at 1800 and 630 GeV. Efficiency is computed as the ratio of reconstructed over generated total number of tracks, for all events of same multiplicity.

Chapter 4

Momentum Correlations and Dispersion

4.1 The Analysis

In the beginning of this chapter we shall discuss some general features of the minimum bias sample. This sample contains –by definition– all possible inelastic physics ranging from soft to hard in its natural amount.

A global description of the minimum bias events can be extracted from a statistical analysis of a multibody final state variable (e.g. the multiplicity) plotted against a reference variable.

The choice of this latter variable is, of course, critical for a meaningful approach to this kind of physics. We chose to use the mean event transverse momentum. This latter variable, involving both transverse momentum and multiplicity, is significantly related to the dynamical origin of the single event. Its value may represent the soft or hard degree of the interaction [55].

In the second part of the chapter we analyze the evolution of the underlying scattering process. To attain this object we perform a comparative study of different types of correlations: in particular (for the limits of this dissertation) the correlation of p_t with multiplicity and the event-by-event fluctuations of the mean event p_t. The analysis of correlations provides a "second order" information with respect to what can be obtained by studying the inclusive particle spectra. In this case we analyze the correlations as a function of a set of statistical variables, namely the charged multiplicity and the total transverse energy.

By examining the same correlations in the full minimum bias sample (this chapter) and in selected sub-samples (next chapter) we evidence the different behavior of the event statistical properties in different dynamical conditions of the interaction.

4.2 Multiplicity in the CTC

To begin it is important to mention how the charged multiplicity is computed. Following the same convention of $Sp\bar{p}S$ experiments (see, for instance [16]) "...in the charged multiplicity distribution only particles from the primary vertex are included, and not, for example the decay products of..." long lived neutral particles such as "...K_s^0 and Λ^0".

This can be obtained in most cases by applying the impact parameter and Z_0 intercept cuts described in the previous chapter to the reconstructed tracks.

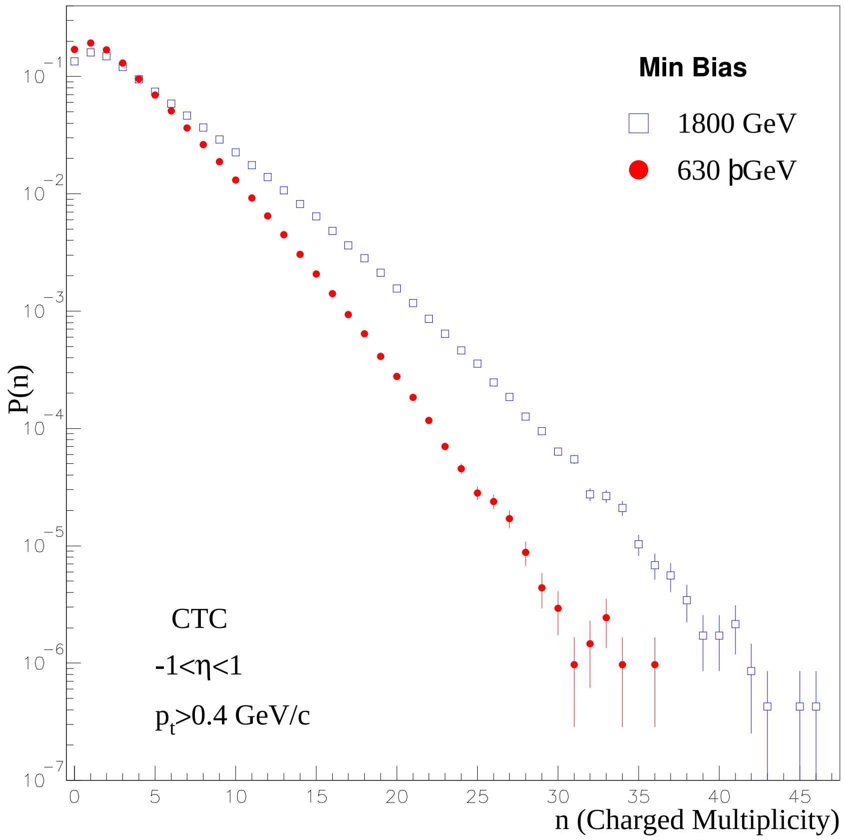

Figure 4.1: Raw multiplicity distribution in the CTC (normalized to one).

The contamination from residual decay products of K_s^0 and Λ^0 (V^0) which are not rejected in this way was estimated with MonteCarlo. This gives a bias on the multiplicity in the order of 3% after having applied the track selection cuts.

In figure 4.1 is shown a distribution of the raw multiplicity as measured by the CTC in the rapidity interval $|\eta| < 1.0$: the probability $P(n)$ for finding an event with n charged particles is plotted versus n. No other corrections for track detection or reconstruction inefficiencies are applied. The errors given are purely statistical, computed assuming a multinomial distribution. No systematic errors are plotted here. The mean value of charged multiplicity in each sample is $\langle n \rangle = 4.094 \pm 0.003$ at 1800 GeV `c.m.s.` energy and $\langle n \rangle = 3.100 \pm 0.002$ at 630 GeV.

The distributions plotted in the KNO z-variable $z = n/\langle n \rangle$ are shown in figure 4.2. Only a weak violation of the KNO scaling at lower multiplicities can be observed, as could be expected in our limited phase space.

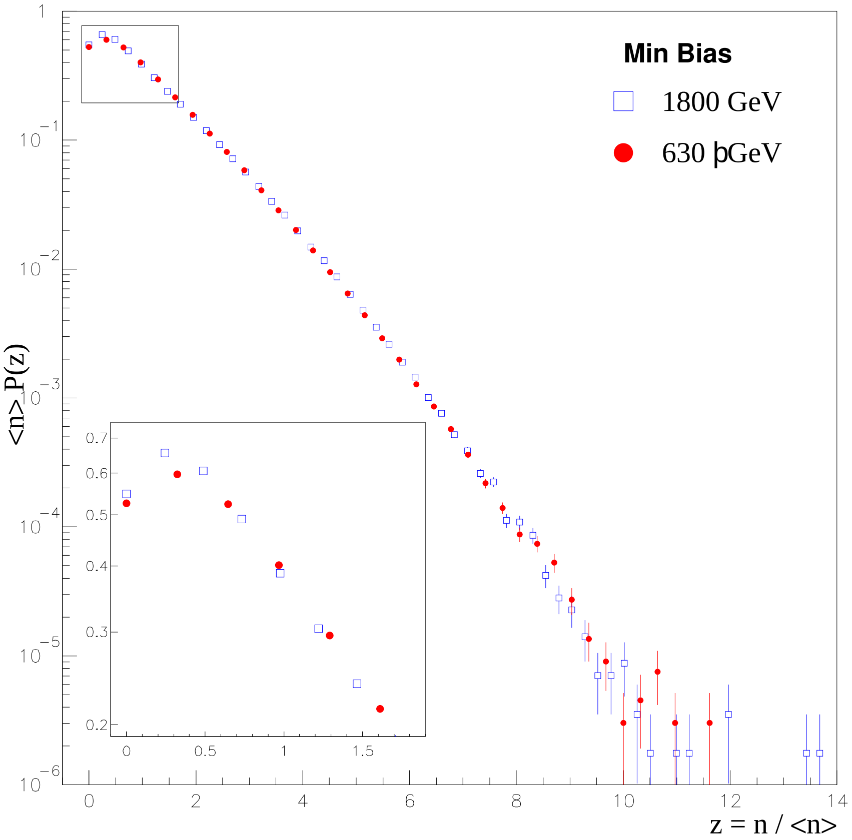

Figure 4.2: Raw multiplicity distribution in KNO form.

4.2.1 Systematics due to primary vertex selection

The decision not to cut those multiple interaction events in which low quality vertices are close to the selected event vertex introduces a small distorsion in the multiplicity distribution since some "true" multiple interactions will not be suppressed. We can estimate the bias introduced in this way by considering the multiplicity distribution obtained in the two opposite conditions. The first in which all observed vertices are considered to be really primary: in this case all multiple interactions are rejected together with some high multiplicity events; the second in which all observed vertices – but the "best" one – are considered secondary vertices and some multiple interactions remain in the sample, but no other bias is introduced in the multiplicity distribution.

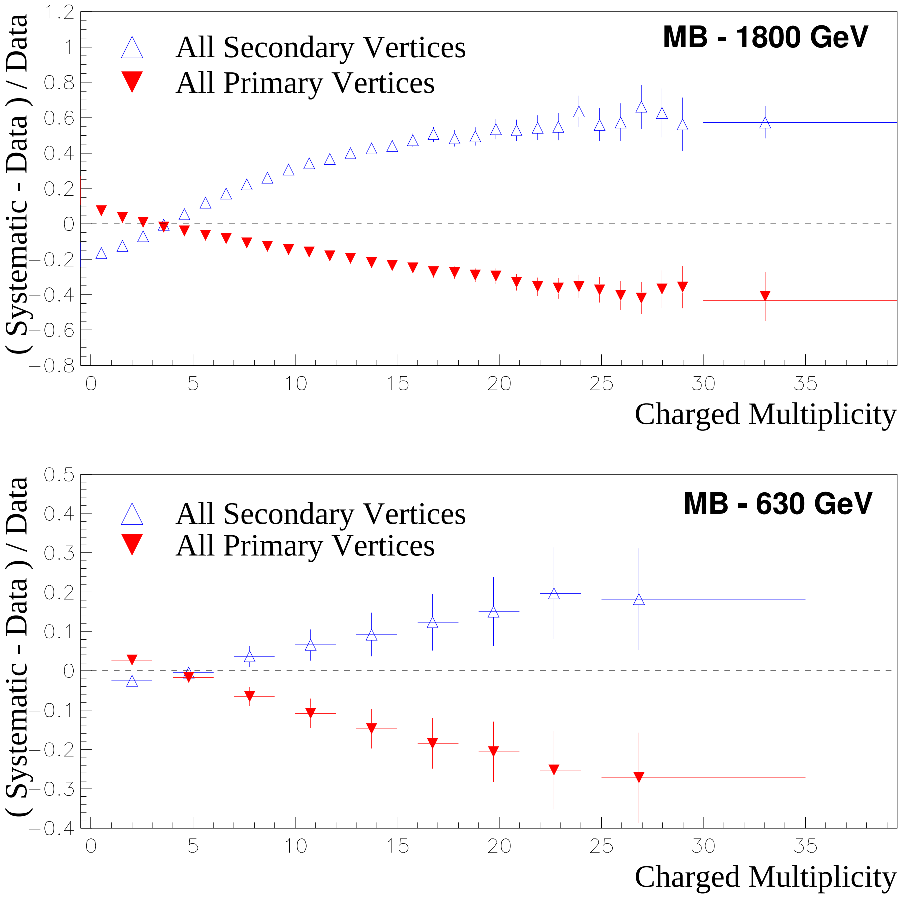

Figure 4.3: Relative value of the difference between the multiplicity distributions obtained from two different primary vertex classifications and the default vertex choice.

The difference is shown in figure 4.3 and can be considered as an upper limit of the systematic error due to fake vertices. The distorsion introduced can be safely assumed to be less than half of this limit. It is to be noticed in any case, that this systematic is approximately equal at both `c.m.s.` energies, so that it can be neglected when comparisons are done.

4.3 The Minimum Bias Sample

Throughout our analysis the mean event transverse momentum is defined as:

$$\langle p_t \rangle_{ev} = \frac{1}{N} \sum_{i}^{N} p_{ti} \tag{4.1}$$

where N is the number of tracks in the CTC that converge to the main event vertex and p_{ti} the transverse momentum of the i^{th} track. Note that $\langle p_t \rangle_{ev}$, as defined in equation 4.1, characterizes the property of a single event: it is qualitatively different from both the average tracks momentum of the sample and from the transverse momentum of a single particle.

The $\langle p_t \rangle_{ev}$ distribution normalized to the number of events in the sample is shown in figure 4.4 at the two energies. The $\langle p_t \rangle_{ev}$ averaged over all events is 0.7742 ± 0.0002 and 0.7478 ± 0.0002 GeV/c for the higher and lower `c.m.s.` energy sample respectively.

In the space of $\langle p_t \rangle_{ev}$ and multiplicity, min-bias events occupy the region of low-p_t *and* low-multiplicity as can be seen in the scatter plot of figure 4.5. For comparison the same plot has been obtained from a small sample of jet triggers (data stream QJTB_6F from run 1C at `c.m.s.` energy of 1800 GeV). This trigger requires the presence of at least one jet with minimum 20 GeV energy in the central calorimeter. About 65.000 events were selected from this trigger, with a jet E_t spectrum which is also shown in figure 4.5. Events from the jet trigger spread in a larger interval of the scatter plot with respect to the min-bias trigger events. A three dimensional plot would show more clearly that the min-bias sample is far more peaked in a smaller region of the plot.

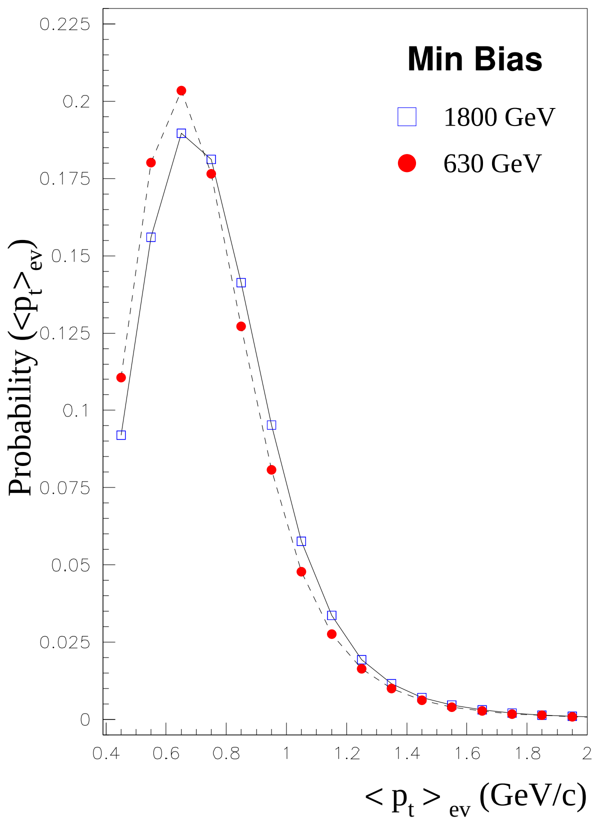

Figure 4.4: The mean event p_t distributions as measured in the CTC. Only tracks in $p_t > 0.4$ GeV/c and $|\eta| < 1.0$ are considered. The distribution is normalized to the number of events in the sample.

4.4 The mean multiplicity as a function of $\langle p_t \rangle_{ev}$

A more meaningful inspection to the same data can be done analyzing the profile (vertical average) of the previous distributions. On the same $\langle p_t \rangle_{ev}$ scale we are now plotting the charged multiplicity averaged over all the events of a given $\langle p_t \rangle_{ev}$. In order to make possible the comparison at the two energies the averaged multiplicity has been further divided by the mean multiplicity of the whole sample (KNO form). Errors are statistical only and are computed as the square root of the dispersion inside the bin.

The data in figure 4.6 show a peculiar shape with a peak around 1 GeV/c. The position of the peak is roughly the same at all energies. Most part of the inelastic cross section is located in the region of this peak. The region ranging from 0.7 to

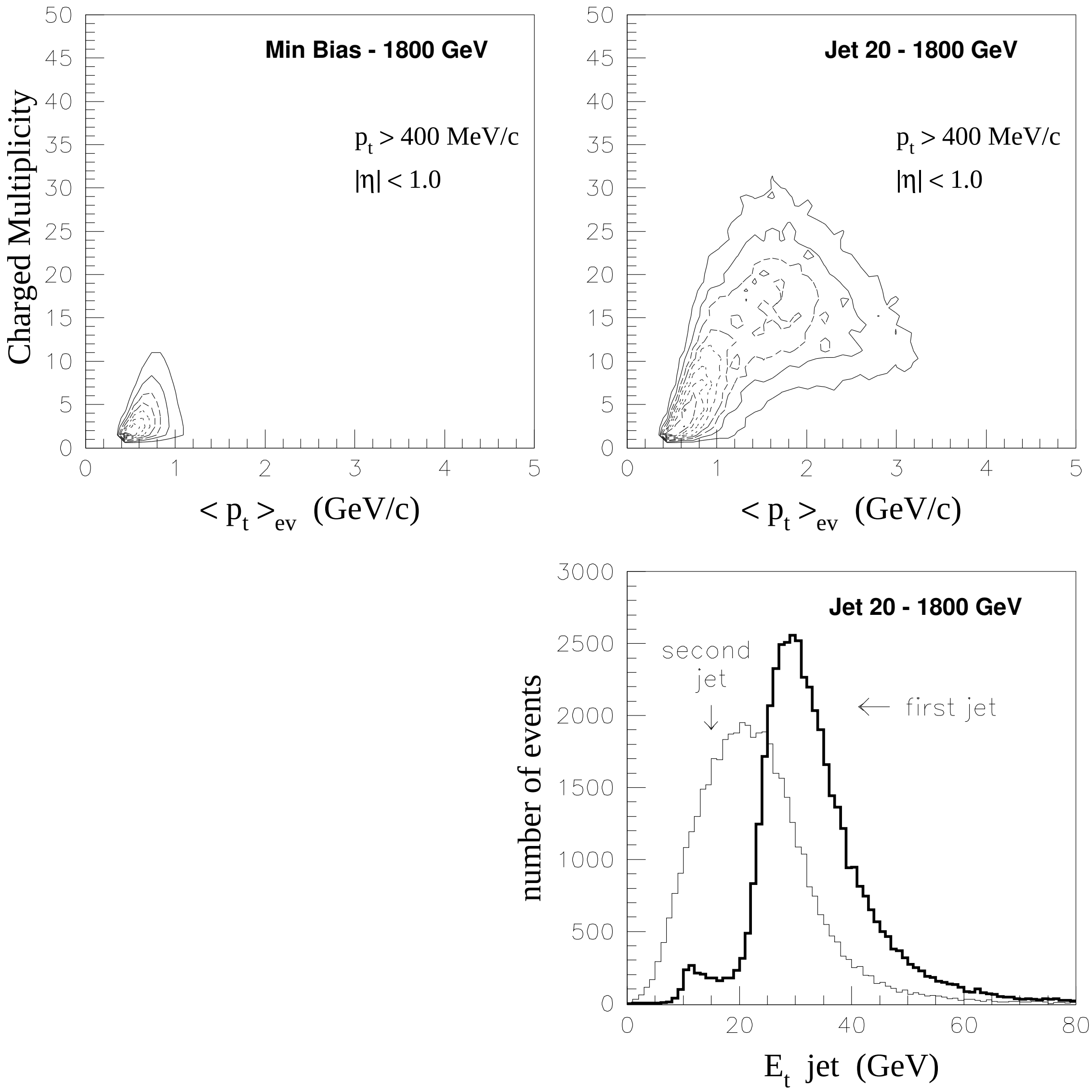

Figure 4.5: Contour plots of the multiplicity versus the mean event p_t in the min bias and jet trigger samples (1800 GeV). Spacing between contours is linear. Lower right: E_t spectra of jets from the JET_20 trigger sample (1800 GeV).

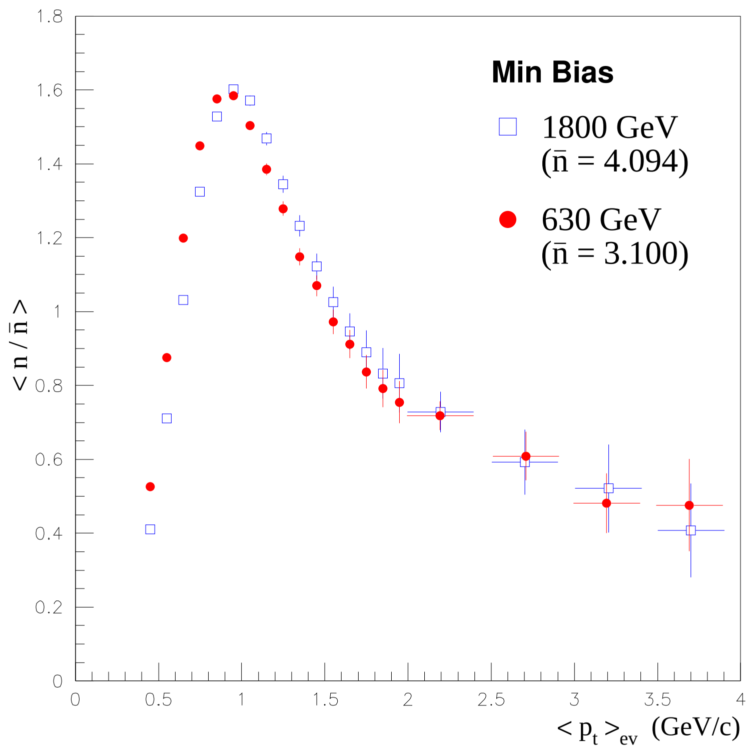

Figure 4.6: Charged multiplicity as a function of the mean event p_t. In order to compare the two energies, the multiplicity has been normalized to the sample mean multiplicity.

1.4 GeV/c contains about 90% of the events both at both `c.m.s.` energies.

It has been suggested [58] that the particular shape of the plot and the initial rise up to the maximum could be an effect of the specific kinematical cuts that we apply and, specifically, of the limited rapidity window that is considered. In order to check the physical significance of the plot the same analysis was repeated on the MonteCarlo sample in the full phase space. Pythia generator was employed in a configuration – described in detail in Appendix 1 – which best reproduces both the multiplicity and the inclusive p_t spectrum in the phase space region in which the data are collected.

In $-1 < \eta < 1$ and $p_t > 0.4$ GeV/c the MonteCarlo simulation roughly reproduces the data. In the full phase space region the simulation still indicates the presence of a rise at low p_t followed by a peak (figure 4.7). The high $\langle p_t \rangle_{ev}$ tail is missing due to the increasing number of soft tracks that enter the distribution.

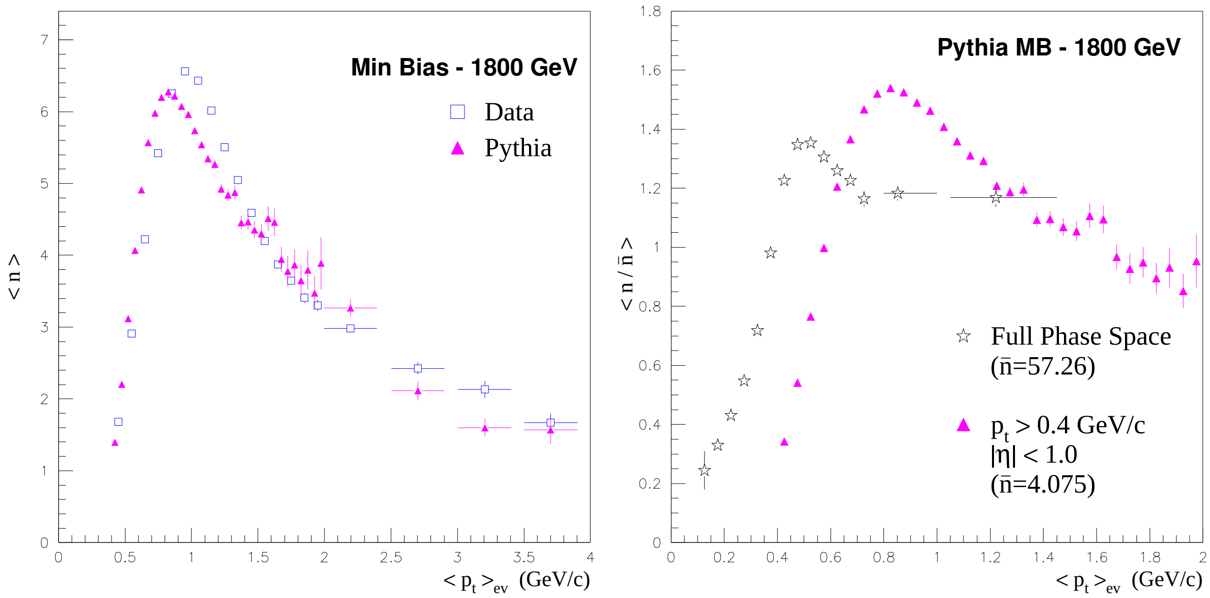

Figure 4.7: Left: charged multiplicity as a function of the mean event p_t in the 1800 GeV data sample and in the Montecarlo sample. Right: Montecarlo data are plotted both in the phase space limits of the CTC and in full phase space, each normalized to its mean multiplicity.

4.5 The Correlation of p_t with multiplicity

The charged multiplicity dependence of the average transverse momentum was first studied for tracks with $p_t > 400$ MeV/c (figure 4.8 and 4.9). Experimentally this correlation can be obtained by computing the mean p_t of all the tracks pertaining to events of equal multiplicity. This implies a different event classification than that employed when computing the mean event transverse momentum $\langle p_t \rangle_{ev}$.

A non-linear rise of the mean p_t is observed both at 630 and 1800 GeV: more pronounced at the higher energy but clearly visible also at the lower energy.

It is worth noting that, despite the limitations imposed by the small phase space region accessible to our tracking instruments, this measure is of high precision and with the higher statistics reached up to now. This allows some detailed analysis of the properties of the correlation.

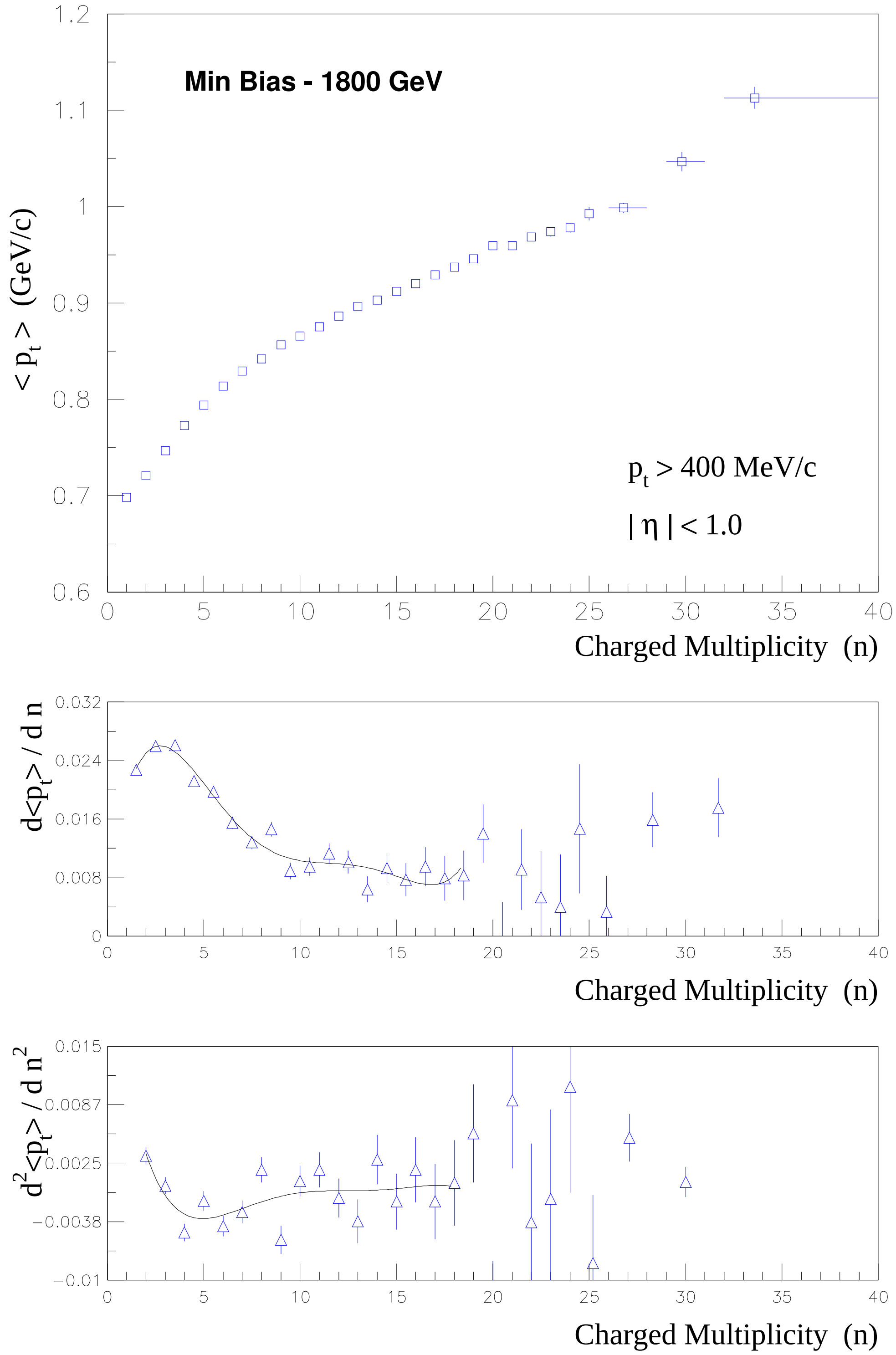

Figure 4.8: Raw average p_t versus the event charged multiplicity (1800 GeV). First and second derivatives are shown below. The continuous lines are intended simply for driving the eye.

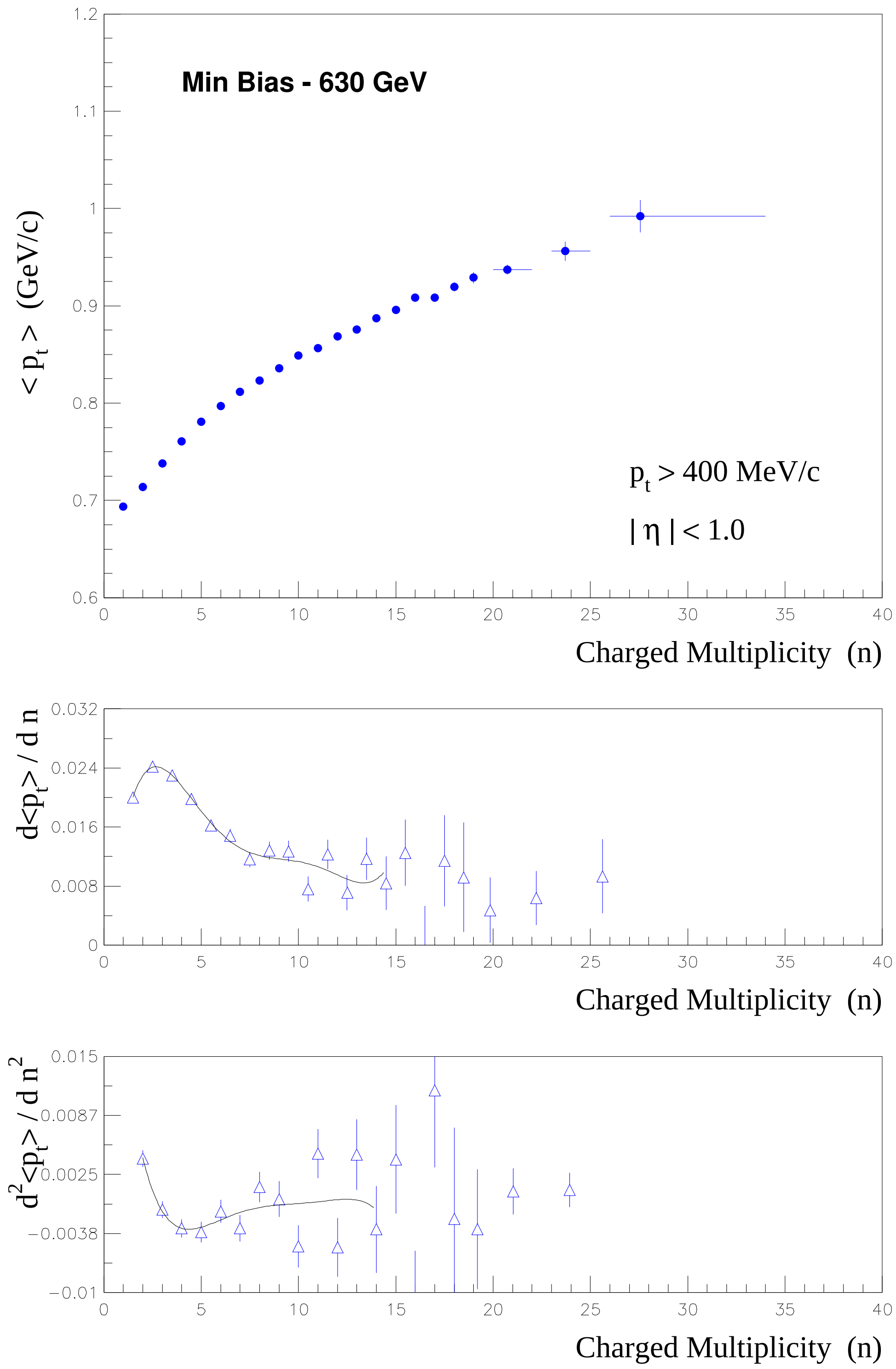

Figure 4.9: Raw average p_t versus the event charged multiplicity (630 GeV). First and second derivatives are shown below. The continuous lines are intended simply for driving the eye.

4.5.1 Derivatives of the Correlation

It is possible to study the structures of the correlation of mean p_t with multiplicity by computing the first and second derivatives of the plot.

The first derivative was obtained by simply computing the difference between two successive bins of the histogram; the second derivative was obtained by applying the same method to the first derivative. The curves are shown in figure 4.8 and 4.9.

At both energies the first derivative has a maximum at multiplicity of about 3, where the second derivative passes through zero. In other words there is a flex in the curve. Both derivatives are flat for multiplicities higher than about 8-10.

4.6 The full p_t spectrum

The definition of the mean value of the transverse momentum is the following:

$$\langle p_t \rangle = \frac{\int_0^\infty \frac{d\sigma}{dp_t} p_t dp_t}{\int_0^\infty \frac{d\sigma}{dp_t} dp_t} \tag{4.2}$$

We measure the p_t spectrum:

$$f = \frac{1}{N_{ev}} \frac{1}{p_t} \frac{\Delta N}{\Delta\eta \Delta p_t} = A \cdot E \frac{d^3\sigma}{dp^3} \tag{4.3}$$

where N_{ev} is the total number of events and $\Delta N / \Delta\eta\Delta p_t$ is the number of tracks per unit pseudorapidity and unit transverse momentum. This quantity becomes a differential cross section when the total inelastic cross section is included in the factor A.

The determination of the "true" value of the transverse momentum relies on the extrapolation of the observed spectrum ($p_t > 400$ MeV/c) to $p_t = 0$. The p_t spectrum measured in the CTC was fitted to the functional form:

$$\frac{df}{dp_t^2} = A \left(\frac{p_t^0}{p_t - p_t^0} \right)^n \tag{4.4}$$

in which A, p^0 and n are the free parameters and the average p_t is determined from the fitted values:

$$\langle p_t \rangle = \frac{2p^0}{n-3} \tag{4.5}$$

This functional form was chosen among the others for best describing the data in the entire p_t range at both energies. For a more complete description of this subject refer to [57, 10].

Before fitting, we applied to the measured p_t spectrum the efficiency correction computed via the MonteCarlo simulation. The effect of the correction is very small: $< 2\%$ for $p_t < 1$ GeV/c and $\lesssim 4\%$ otherwise. The measured number of particles is decreased for $p_t < 3$ GeV/c and increased for higher p_t.

To check the consistency of our data with 1989 CDF measurements [59] we fitted the full sample (run 1A, 1B and 1C) p_t spectrum in the range $p_t > 400$ MeV/c: the fit parameters and their statistical errors are given in table 4.1. Our measure yields $\langle p_t \rangle = 0.488 \pm 0.001$ GeV/c (1989 data: $\langle p_t \rangle = 0.495 \pm 0.014$ GeV/c) at 1800 GeV `c.m.s.` energy and $\langle p_t \rangle = 0.457 \pm 0.002$ GeV/c (1989 data: $\langle p_t \rangle = 0.432 \pm 0.004$ GeV/c) at 630 GeV. Considered a reported systematic error of 20 MeV common to both energies on 1989 data, our measure is in accordance with the previous one.

Energy	χ^2/dof	p^o	Δp^o	n	Δn	$\langle p_t \rangle$ (GeV/c)	$\Delta\langle p_t \rangle$ (GeV/c)
1800	0.63	1.24	0.01	8.09	0.04	0.488	0.001
630	0.71	1.38	0.02	9.03	0.09	0.457	0.002
1800	0.53	1.23	0.01	8.11	0.05	0.483	0.001
630	0.68	1.37	0.003	9.04	0.09	0.455	0.002

Table 4.1: Fit parameters and average p_t of the Minimum Bias samples. Upper rows: default event selection is applied. Lower rows: the event selection applied is the tighter one employed when the calorimeter measure is needed. Errors are statistical only.

4.6.1 Fits to p_t spectra at fixed multiplicities

In order to measure the dependence of the "true" mean p_t on the multiplicity we used the functional form in 4.4 to fit the p_t spectra for each (fixed) multiplicity.

Each p_t spectra was corrected for the overall inefficiency given by the simulation described in the previous chapter.

In each fit all the parameters were let free to vary; the χ^2s obtained are quite good at all multiplicities. Data from the fit are reported in tables 4.2 and 4.3.

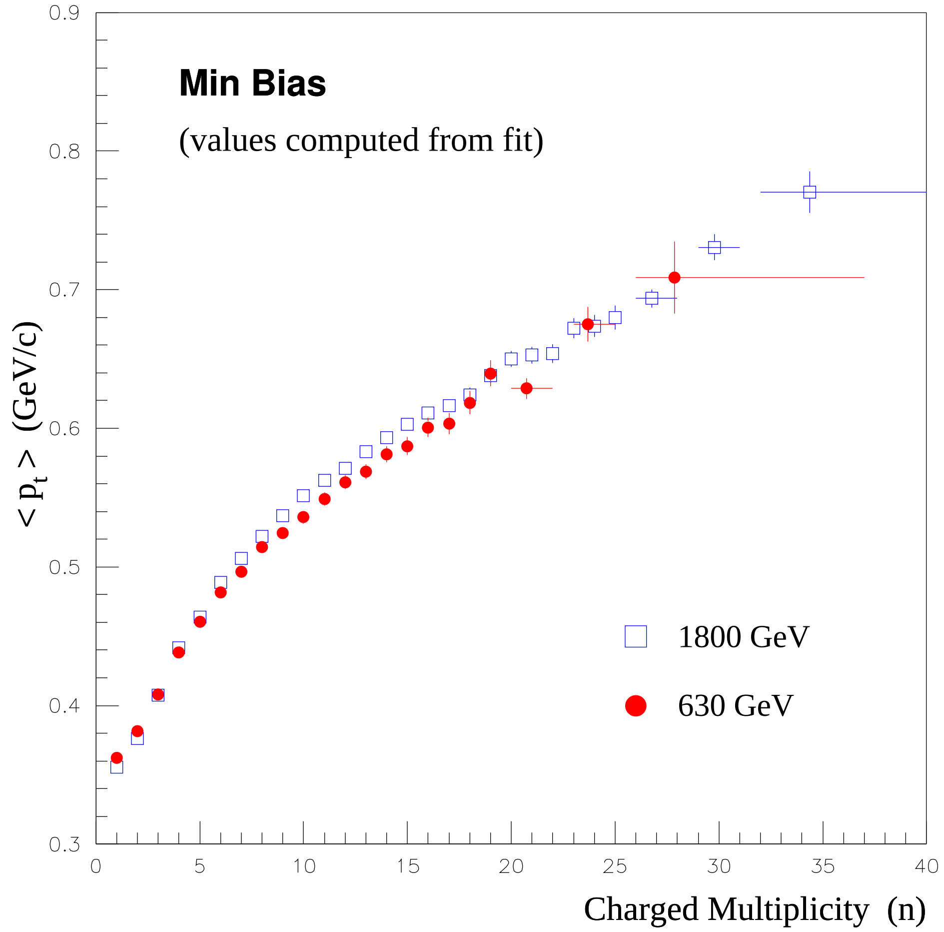

Figure 4.10: The mean p_t versus the charged multiplicity. Each point has been computed by fitting the p_t spectrum of the corresponding multiplicity.

The corrected final correlation is shown in figure 4.10 at both energies. With respect to the raw data the average transverse momentum is obviously smaller but the shape of the dependence seems to be preserved.

1800 GeV				
Multiplicity	$\chi^2/d.o.f.$	p^o	n	$\langle p_t \rangle$ (GeV/c)
1	1.4	1.35±0.06	10.6±0.2	0.356±0.004
2	1.0	1.25±0.04	9.7±0.2	0.376±0.003
3	0.6	1.29±0.04	9.3±0.1	0.408±0.003
4	0.7	1.40±0.04	9.3±0.1	0.442±0.003
5	0.5	1.39±0.04	9.0±0.1	0.464±0.003
6	0.5	1.46±0.04	9.0±0.1	0.489±0.003
7	0.5	1.48±0.04	8.9±0.1	0.506±0.004
8	0.4	1.52±0.04	8.8±0.1	0.522±0.004
9	0.6	1.51±0.04	8.6±0.1	0.537±0.004
10	0.7	1.60±0.05	8.8±0.1	0.551±0.004
11	0.5	1.63±0.05	8.8±0.1	0.562±0.004
12	0.4	1.56±0.04	8.5±0.1	0.571±0.004
13	0.6	1.59±0.05	8.5±0.1	0.583±0.004
14	0.4	1.66±0.05	8.6±0.1	0.593±0.004
15	0.6	1.66±0.05	8.5±0.2	0.603±0.004
16	0.4	1.68±0.06	8.5±0.2	0.611±0.004
17	0.5	1.58±0.06	8.1±0.2	0.617±0.005
18	0.4	1.57±0.06	8.0±0.2	0.624±0.005
19	0.4	1.66±0.07	8.2±0.2	0.638±0.005
20	0.6	1.67±0.07	8.1±0.2	0.650±0.006
21	0.6	1.74±0.09	8.3±0.2	0.653±0.006
22	0.5	1.55±0.09	7.7±0.2	0.654±0.007
23	0.7	1.85±0.10	8.5±0.3	0.672±0.007
24	1.2	2.0±0.1	8.9±0.4	0.674±0.008
25	0.6	1.7±0.1	7.9±0.3	0.680±0.009
26 - 28	0.9	1.69±0.09	7.9±0.2	0.694±0.006
29 - 31	0.6	1.6±0.1	7.3±0.3	0.731±0.009
32 - 41	1.3	2.2±0.2	8.7±0.6	0.77±0.01

Table 4.2: Fit parameters and average p_t for each multiplicity (1800 GeV).

630 GeV				
Multiplicity	$\chi^2/d.o.f.$	p^o	n	$\langle p_t \rangle$ (GeV/c)
1	1.7	1.61±0.08	11.9±0.3	0.362±0.004
2	1.0	1.49±0.06	10.8±0.2	0.381±0.003
3	0.7	1.47±0.05	10.2±0.2	0.408±0.003
4	0.8	1.59±0.05	10.3±0.2	0.438±0.003
5	0.3	1.61±0.06	10.0±0.2	0.461±0.004
6	0.6	1.69±0.06	10.0±0.2	0.482±0.004
7	0.4	1.66±0.06	9.7±0.2	0.497±0.004
8	0.7	1.79±0.06	9.9±0.2	0.514±0.004
9	0.5	1.70±0.06	9.5±0.2	0.525±0.004
10	0.4	1.65±0.06	9.2±0.2	0.536±0.005
11	0.5	1.77±0.07	9.4±0.2	0.549±0.005
12	0.5	1.77±0.08	9.3±0.2	0.561±0.005
13	0.5	1.77±0.08	9.2±0.2	0.569±0.005
14	0.5	1.76±0.09	9.1±0.3	0.581±0.006
15	0.4	1.7±0.1	8.9±0.3	0.587±0.006
16	0.5	1.8±0.1	8.8±0.3	0.601±0.007
17	0.4	1.8±0.1	8.9±0.4	0.603±0.008
18	0.6	1.8±0.2	8.9±0.5	0.618±0.008
19	0.8	2.4±0.2	10.7±0.7	0.640±0.009
20 - 22	0.6	1.7±0.1	8.4±0.3	0.629±0.008
23 - 25	0.6	1.8±0.3	8.4±0.7	0.68±0.01
26 - 37	2.1	5.4±1.8	18±5	0.71±0.03

Table 4.3: Fit parameters and average p_t for each multiplicity (630 GeV).

4.7 The dispersion of the event mean transverse momentum

4.7.1 Definition and meaning

Studies of event-by-event non statistical fluctuations of the event mean p_t were presented by ISR experiments [60]. In figure 4.11 the dispersion of the mean event p_t as obtained from those data is plotted as a function of the inverse of the multiplicity at the `c.m.s.` energy of 63 GeV.

The dispersion (normalized to the mean p_t of the sample) is defined as follows:

$$D_n\left(\bar{p}_t\right) = \frac{\langle \bar{p}_t^2 \rangle_n - \langle \bar{p}_t \rangle_n^2}{\langle p_t \rangle_{sample}} \tag{4.6}$$

Brackets $\langle\rangle$ indicate average over all events with a given multiplicity n, while $\bar{p}_t$ is here the mean event p_t as was defined in 4.1.

The dispersion D is expected to decrease with increasing multiplicity and to converge to zero when $n \to \infty$ if only pure statistical fluctuations are present. Conversely, an extrapolation to a non-zero value would indicate the presence of non statistical fluctuations from event to event in the $\bar{p}_t$ distribution.

Assuming that a possible non-statistical contribution to the $\langle p_t \rangle_{ev}$ fluctuations does not depend on multiplicity, the square of the normalized dispersion can be written as:

$$R_n^2 = a + \frac{b}{n} \tag{4.7}$$

where n is the charged multiplicity and the parameters a and b (intercept and slope) may be computed from the data.

In ISR data a linear extrapolation to $n \to \infty$ yields 0.0133±0.0001 with a slope of 0.425±0.006. It has to be noticed that these data were taken in a central window of $|x| < 0.3$ and no p_t cutoff.

4.8 Raw data Dispersion

We repeated the same analysis in the limited phase space accessible to CDF tracking. In our data (figure 4.12) the points at high multiplicity clearly deviate from linearity in the 1800 GeV sample. This behaviour is present also in the low energy sample,

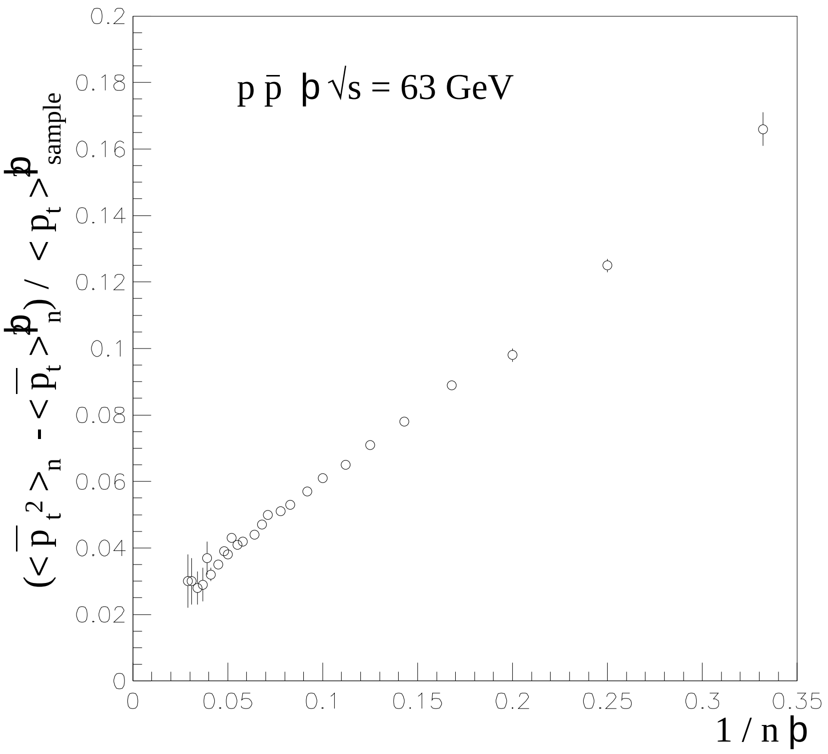

Figure 4.11: The mean event p_t dispersion at 63 GeV c.m.s. energy (as measured at ISR by SFM) is plotted against the inverse multiplicity $1/n$.

although much smaller (it will become more evident when the MB sample is analyzed as the sum of different components: see chapter 5).

This effect is new and completely unexpected: besides confirming the presence of non statistical fluctuations in the sample, it seems to indicate the onset of a distinct type of event-by-event fluctuations at multiplicities between 8 and 10.

Despite the non-linear behavior of the data a linear fit in different multiplicity ranges was attempted. Fit parameters and values of the extrapolation to $n \to \infty$ are reported in table 4.2. The value of the intercept at ∞ multiplicity is always greater (and non compatible) than zero whatever fit range is used.

The region of multiplicity in which the dispersion is linear (within the errors) is the same region in which the correlation of the mean p_t with multiplicity show a negative second derivative, that is to say the low multiplicity region.

In thermodynamical models these fluctuations in $\langle p_t \rangle_{ev}$ can be interpreted as fluctuations in temperature: the interacting particles may experience a large transverse

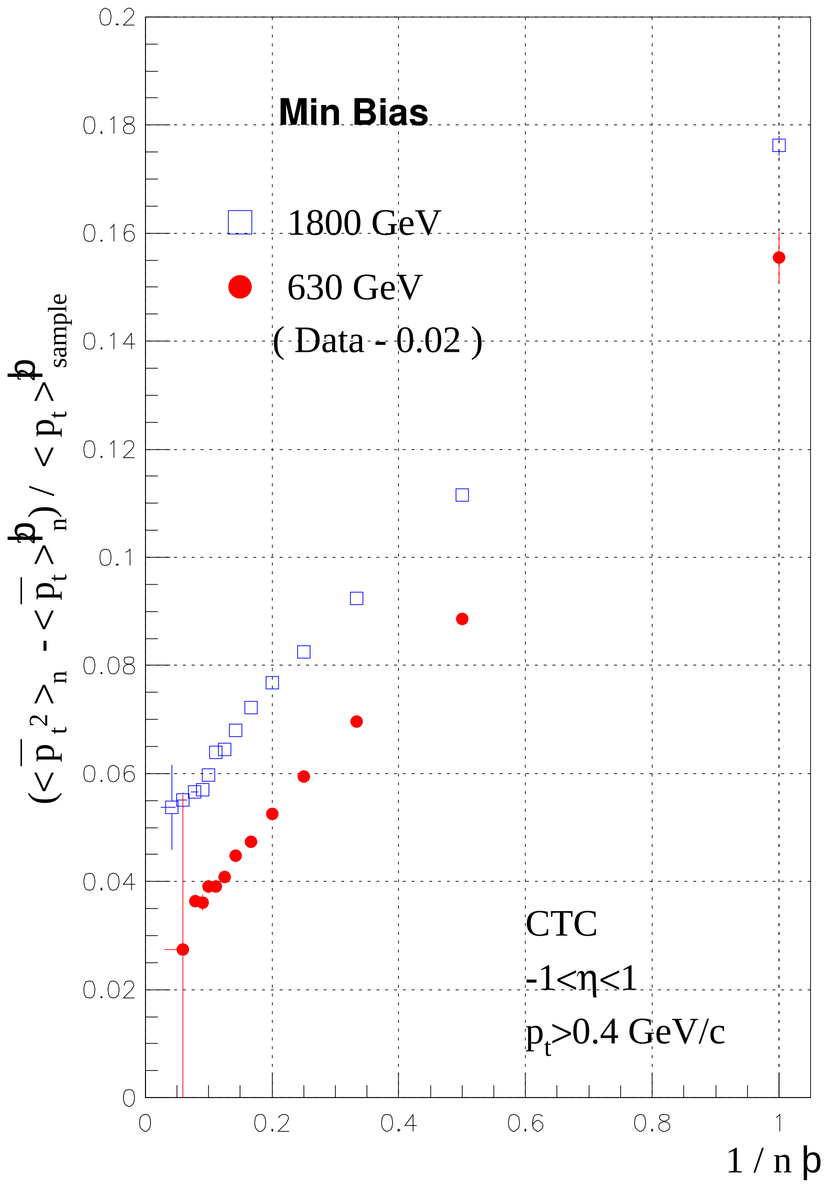

Figure 4.12: Raw data dispersion of the mean event p_t versus the inverse multiplicity at both energies. The statistical error is added in quadrature to the experimental CTC resolution. A bias of 0.02 have been subtracted to the 630 GeV data in order not to overlap the two graphs.

relative acceleration which may be connected with thermal emission of particles at a temperature T given by $kT = a/2\pi$ where k is the Boltzmann constant [61].

Energy	Mult. Range	χ^2/dof	Intercept	Slope
1800	1 - 41	3.6	0.0488±0.0004	0.129±0.002
1800	1 - 7	1.1	0.051±0.001	0.123±0.002
Pythia (1800)	1 - 38	0.7	0.052±0.001	0.078±0.004
Pythia (1800)	1 - 7	0.6	0.053±0.002	0.075±0.004
630	1 - 33	0.9	0.0462±0.0005	0.128±0.002
630	1 - 7	0.8	0.047±0.001	0.125±0.003

Table 4.4: Fit parameters for the dispersion at both energies.

4.8.1 Statistical error and CTC Resolution

The statistical error can be estimated when one consider the numerator of our dispersion (D) as the sampling variance of the event $\langle p_t \rangle_{ev}$. The error can then be computed with the aid of the following approximated formula [62]:

$$variance(D) = \frac{\mu_4 - \mu_2^2}{N_{ev}} - \frac{2\,(\mu_4 - 2\mu_2^2)}{N_{ev}^2} + \frac{\mu_4 - 3\mu_2^2}{N_{ev}^3} + \cdots \tag{4.8}$$

where μ_k is the k-th order moment around the mean and N_{ev} the number of events in the sample.

The experimental resolution on the mean p_t was computed in each multiplicity bin as:

$$R_n^2 = \frac{1}{N_n} \sum_{j=1}^{N_n} \frac{1}{n} \sum_{i=1}^{n} \left(\frac{\sigma_i}{p_{ti}} \right)^2 \tag{4.9}$$

where σ_i is the error on the measure of transverse momentum of each track as obtained by the offline reconstruction code and N_n is the number of events with a given multiplicity n. This quantity is directly comparable with the $\langle p_t \rangle_{ev}$ (normalized) dispersion and is always at least an order of magnitude smaller, over all the multiplicity range. Therefore we can assume that the measured dispersion is not due to instrumental effects. The CTC resolution as computed in 4.9 has been added in quadrature to the statistical error of the measured dispersion in figure 4.12.

4.8.2 MonteCarlo Dispersion

The dispersion of $\langle p_t \rangle_{ev}$ was computed for the MonteCarlo sample and is shown in figure 4.13. The global shape only very roughly resemble the data both at high and low multiplicity.

The overall sample dispersion for the MonteCarlo is 0.089 ± 0.001 (data: 0.107 ± 0.001) at 1800 GeV and 0.092 ± 0.001 (data 0.109 ± 0.001) at 630 GeV.

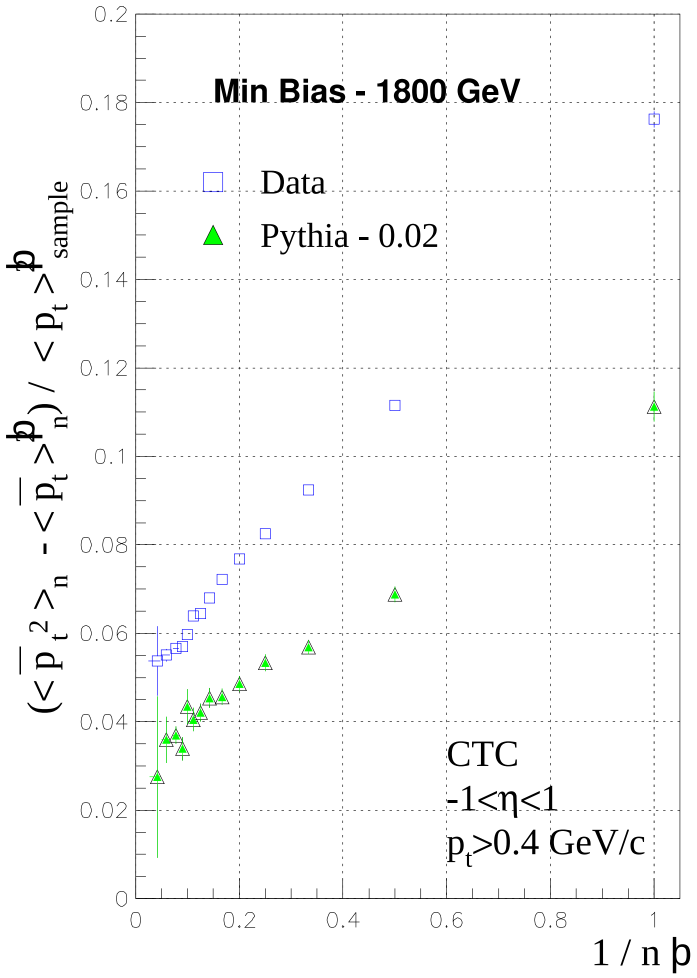

Figure 4.13: MonteCarlo dispersion of the mean event p_t versus the inverse of multiplicity. A bias of 0.02 have been subtracted to the simulated data in order not to overlap the two graphs.

Chapter 5

Correlations versus Transverse Energy

5.1 Further Analysis

In this chapter a deeper investigation on the global properties of the minimum bias events is carried on.

The same correlations discussed in the previous chapter are examined more in detail by analyzing their structure in separate subsamples of different transverse energy. The transverse energy is computed for each event as the sum of the transverse energies deposited in the Central and Plug calorimeter towers (for convenience we recall that the angular region covered by these detectors reaches 2.4 units in η).

The operation of decomposing the whole minimum bias sample according to the event total transverse energy is equivalent to introducing a third variable (the E_t) in the plots already seen. In this way another degree of freedom in the underlying dynamics is being taken care of and the statistical description of the event is significantly simplified.

The same idea is also applied by selecting another different "variable". A distinct decomposition of the minimum bias sample is obtained by choosing those events in which one or more particle cluster can be separated from the rest of the final state.

In the first part of the chapter we describe the additional selections that need to be applied when the calorimeter measures are introduced.

In the second part we discuss the same analyses seen in chapter four in different transverse energy ranges.

Finally, the CDF clustering algorithm is shortly described with its application to our data.

5.2 Calorimeter Backgrounds

The background for spurious or instrumental effects, residual cosmics or noise in the calorimeter is different than in the tracking system. For this reason the sample of events in the analyses which use only tracking information is different from that where both tracking and calorimeter were used.

We list here a set of additional cuts that were applied in the following analyses. After these selections 2.080.297 events remained from the full 1800 GeV sample and 1.982.712 from the 630 GeV sample.

5.2.1 Multiple Interactions

All multiple interaction events were rejected, independently of the distance of the main event vertex from the other primary vertices.

The uncertainty on the classification of the "true" primary vertices reflects in a systematic error in the measure of the transverse energy which - as explained in § 3.4.1 - depends on the event multiplicity.

The upper and lower bounds of the bandwidth on which our measure relies can be appraised as the energy difference of events for which low-quality vertices are classified as primary or secondary. The ratio of this difference over the event total transverse energy, almost independent of multiplicity, is about 6% (1800 GeV) and 3% (630 GeV).

5.2.2 Instrumental effects

A few events were found in which a charged multiplicity greater than zero was measured by the tracking, but no towers in the calorimeters signal an energy release of more than 100 MeV. Such events were rejected.

A visual scan of more than 500 events have been done on a selected sample for which the electromagnetic or hadronic energy fraction (EMF and HAF) exceeded a

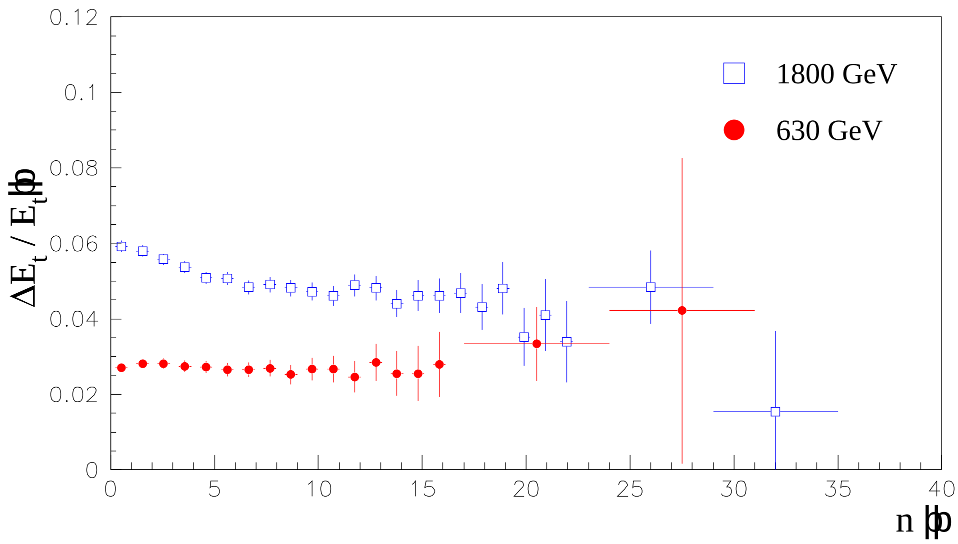

Figure 5.1: The relative error due to classification uncertainty of the primary vertices versus charged multiplicity.

given threshold (98% for the EMF and 90% for HAF).

Two different intrumental effects were found, both in the End-Plug calorimeters.

1) Many events show a "double ring" configuration of hit EM towers, always at the same rapidity. A typical event is shown in figure 5.2. About 16.000 such events were rejected from Run 1A, 1B and 1C (1800 GeV) and about 3.000 from Run 1C (630 GeV).

2) A small number of events was found in which is present a cluster of more than 12 contiguous hit hadronc towers with an energy deposit smaller than 1 GeV per tower. No EM energy is measured in these towers and no track points to the cluster. Since the shape of these clusters is typically geometrical they were attributed to misfunctions of the calorimeter and the events were rejected. Figure 5.3 shows a lego plot of the EM and HAD calorimeters in one of these cases.

5.2.3 Residual Cosmics

A residual number of cosmic rays crossing transversally the detector was found in the central hadronic calorimeter.

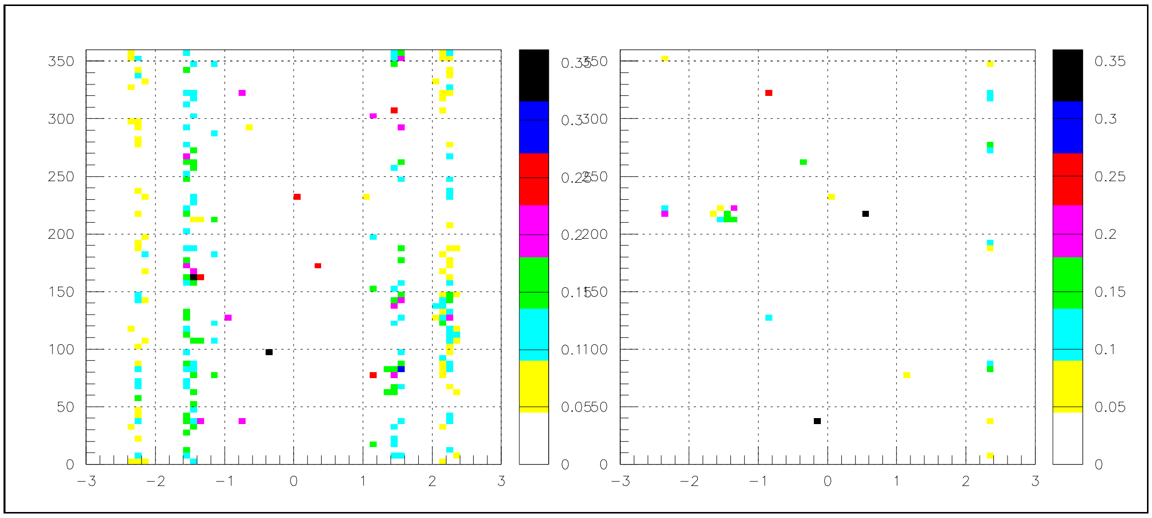

Figure 5.2: The "two-rings" configuration of the EM End Plug calorimeter. The EM towers are plotted on the left, the HAD towers on the right. The event shown is number 66773 of Run 63079 (1B).

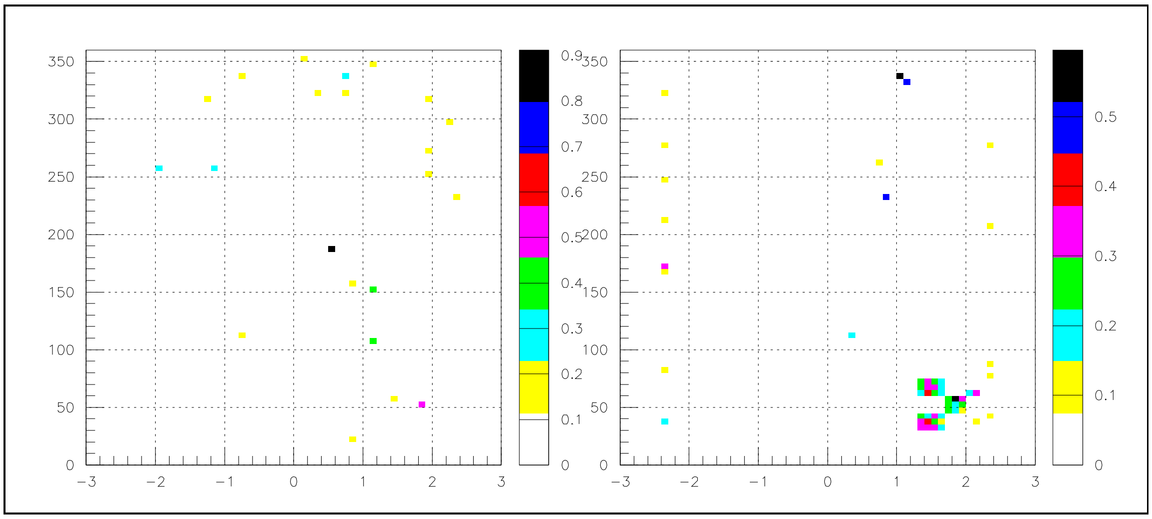

Figure 5.3: Lego plot of the calorimeters. A group of hit hadronic towers due to malfunctions is visible on the lower right corner. The event shown is number 28837 of run 66246 (1B).

These particles hit the upper part of the detector and - since they are oblique with respect to the vertical axis -they leave a track of hit towers in the external (hadronic) calorimeter. In each tower is deposited no more than 1 GeV of transverse energy so that the total energy due to the cosmic is in the order of 5 GeV.

A total of 970 such events were found: a visual scan of the lego plots of the calorimeter (an example in figure 5.4) ensures we are not rejecting good events.

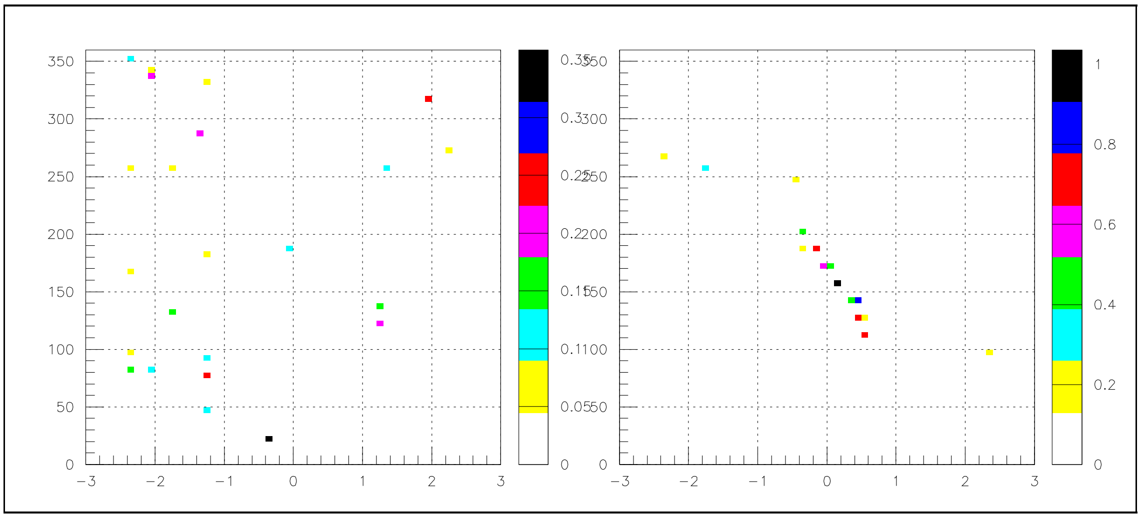

Figure 5.4: Lego plot of the EM (left) and HAD (right) calorimeters. A particle from $\phi \approx 100^o$ hits the HAD calorimeter and leaves a track of small energy deposits along its path. The event shown is number 482404 of run 61247 (1B).

5.2.4 Bad runs rejection

Runs numbered 58450, 58451 and 58482 were found to have an exceedingly high number of events with more than 250 calorimeter towers hit and were excluded from the good runs list.

5.3 Transverse Energy Intervals

The event average transverse energy has been measured in the Central and End-Plug calorimeters to be $\langle E_t \rangle = 15.54 \pm 0.01$ GeV at the higher `c.m.s.` energy and $\langle E_t \rangle = 12.00 \pm 0.01$ GeV at the lower energy (errors reported are statistical only).

The selection of the E_t intervals was done first at 1800 GeV choosing the smallest possible intervals compatible with a sufficiently high statistic. For the selection at lower energy the criterion followed was that the relative "hardness" of the events at the two energies should be the same.

Since we are not dealing with jets, the criterion of selecting transverse energies for which the parton's x_T is approximately the same (see [63]) seemed not to be correct.

Our choice was that the x_T spectrum should be the same at both energies, so that:

$$\int_0^{x_T} x_T dx_T \Big|_{E_{CMS}=1800} = \int_0^{x_T} x_T dx_T \Big|_{E_{CMS}=630} \tag{5.1}$$

With the approximation:

$$x_T \approx \frac{2E_t}{\sqrt{s}} \tag{5.2}$$

we used equation 5.1 to compute the energy ranges at 630 GeV once they were selected at 1800 GeV.

It may be interesting to notice that E_t ranges selected in such a way (table 5.1) are roughly equal to what one would obtain by considering the ratio of the mean transverse energies ($\langle E_t(630)\rangle / \langle E_t(1800)\rangle \simeq 0.78$) or the ratio of the squared logarithm of the `c.m.s.` energies ($\ln^2 630 / \ln^2 1800 \simeq 0.74$).

1800 GeV		630 GeV	
E_t (GeV)	events	E_t (GeV)	events
0 - 3.0	21606	0 - 2.2	43621
3.0 - 6.0	221119	2.2 - 4.4	302407
6.0 - 9.0	318834	4.4 - 7.2	359993
9.0 - 12	279700	7.2 - 9.8	286263
12 - 15	224658	9.8 - 12	209820
15 - 20	269738	12 - 15	219737
20 - 25	173756	15 - 20	114155
25 - 30	109452	20 - 24	56580
30 - 40	110674	24 - 30	40088
40 - 50	40361	30 - 38	8370

Table 5.1: E_t intervals at the two `c.m.s.` energies. The number of events in each interval is also reported.

5.4 Correlation in E_t intervals

The correlation of the average p_t with multiplicity is shown in figures 5.5 and 5.6 for the selected transverse energy ranges.

At both energies the shape of the correlation is approximately flat but the value of the mean p_t increases with E_t. The rate of this increase is not constant with E_t so that it is reasonable to see in this change the origin of the non linearity of the plot in the full minimum bias sample.

5.5 Dispersion in E_t intervals

We computed the dispersion as defined in equation 4.6 in all different E_t intervals (figures 5.7 and 5.8). In limited energy ranges the data show a roughly linear behavior up to about 30 GeV (at 1800 GeV). The slopes of the data points decrease with increasing E_t; as for the case of the correlation of momentum with multiplicity this suggests that the non linear behavior of the full sample is due to the rate of the change of the slope with transverse energy.

The data points were fitted to a line in the full multiplicity range. The extrapolation to $n \to \infty$ always gives intercept values much closer to zero than the full sample value. In some intervals, though, the extrapolation yields an unphysical negative value which suggests that the linear fit does not represent the data.

In figure 5.9 and 5.10 the dispersion is plotted against the inverse multiplicity for events with total E_t smaller or greater than a given threshold.

It is clearly visible a different behavior for multiplicities greater than about 10: while the curve for events with total E_t less than threshold weakly slows down, the other curve rises after that multiplicity.

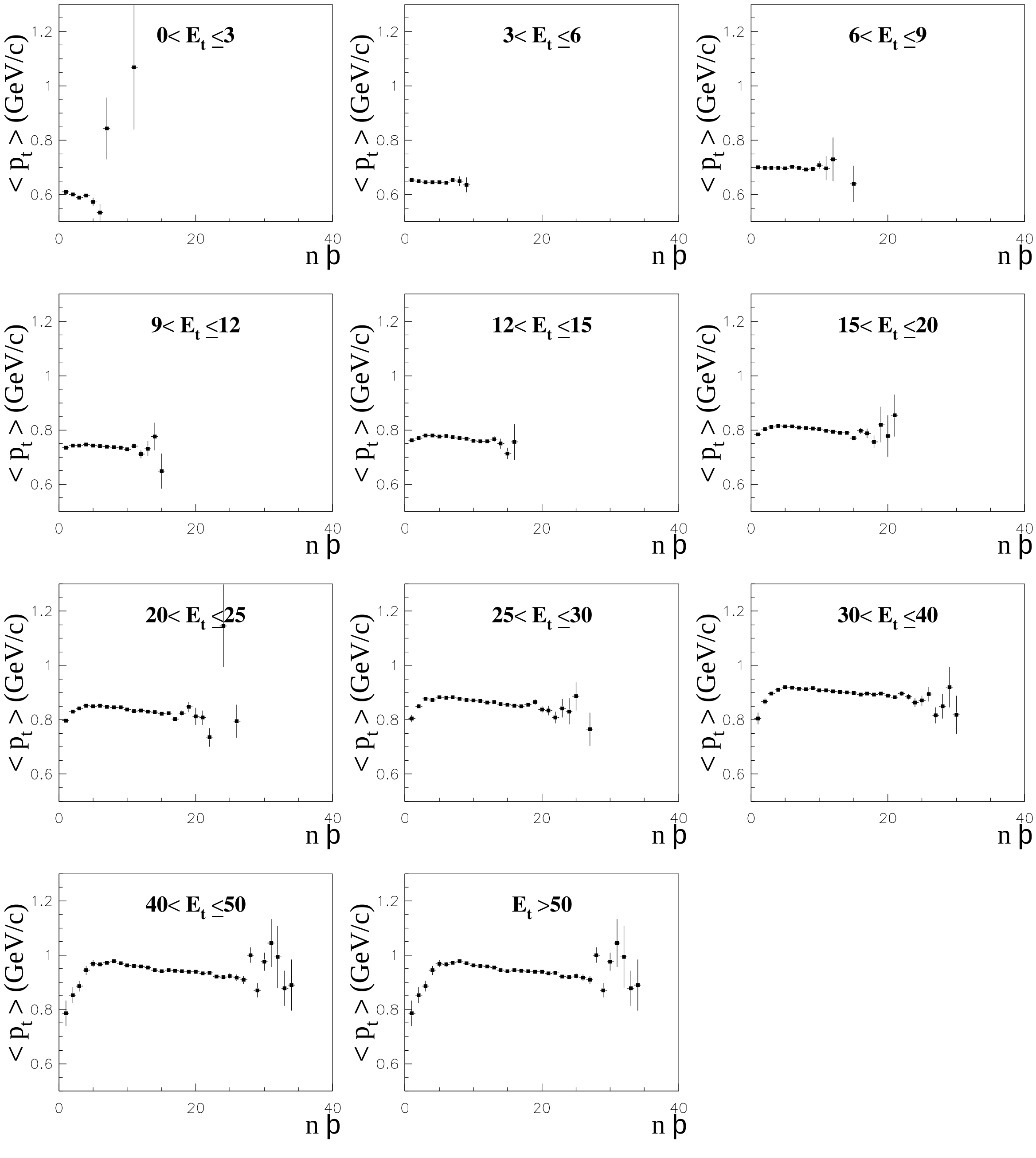

Figure 5.5: The correlation of the average p_t with multiplicity at 1800 GeV is shown in 10 E_t intervals.

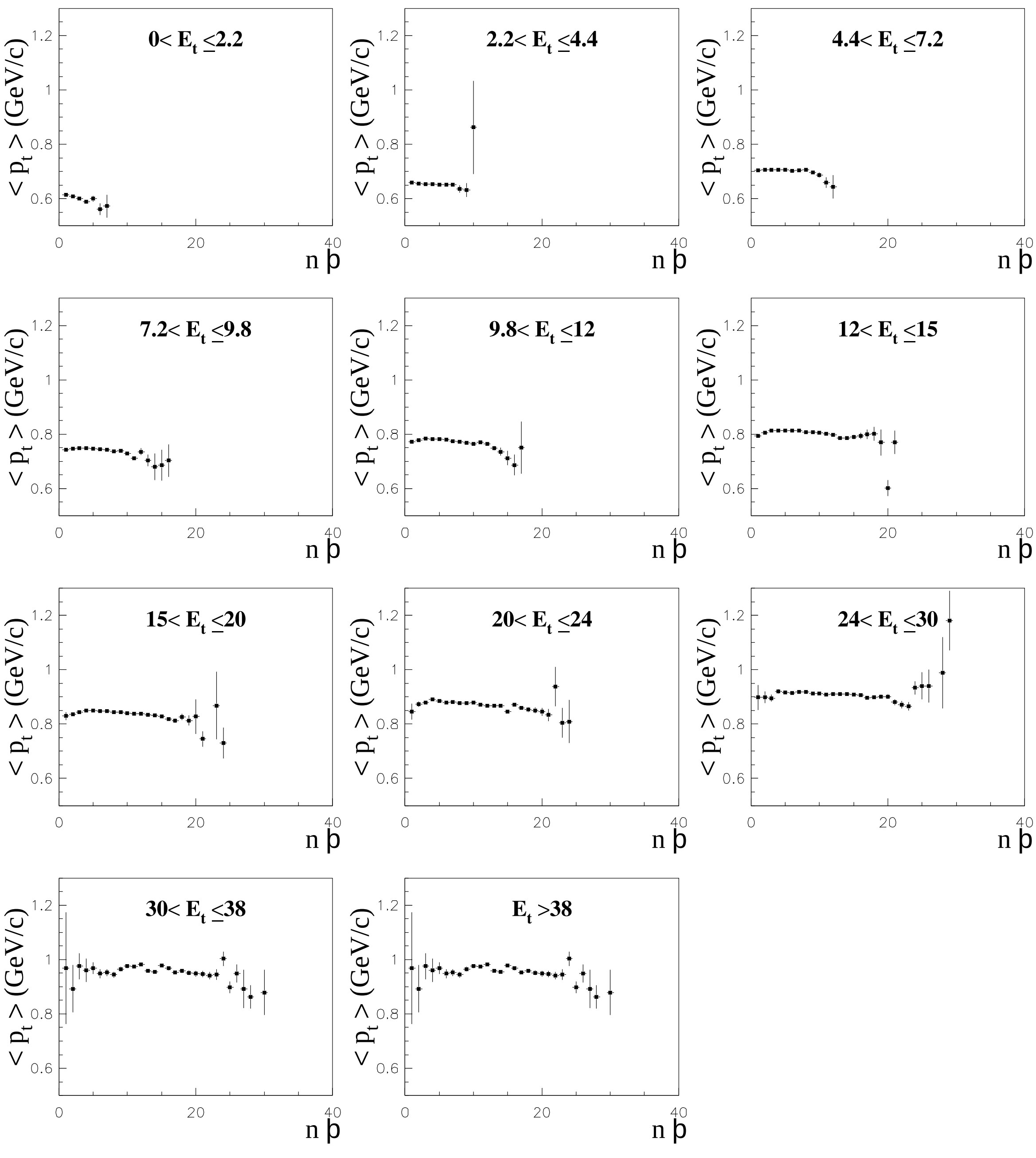

Figure 5.6: The correlation of the average p_t with multiplicity at 630 GeV is shown in 10 E_t intervals.

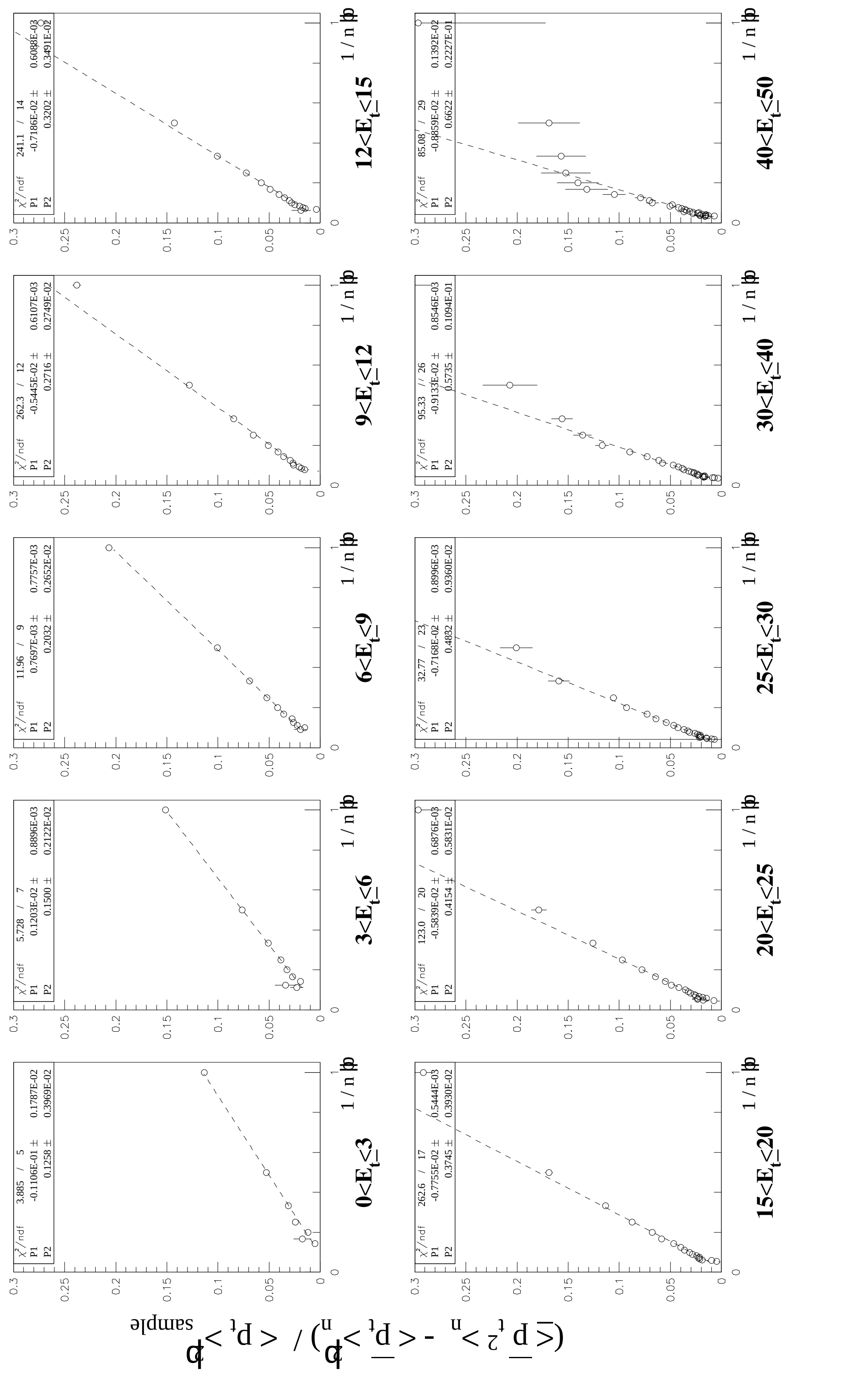

Figure 5.7: The $\langle p_t \rangle_{ev}$ dispersion at 1800 GeV in 10 different E_t intervals.

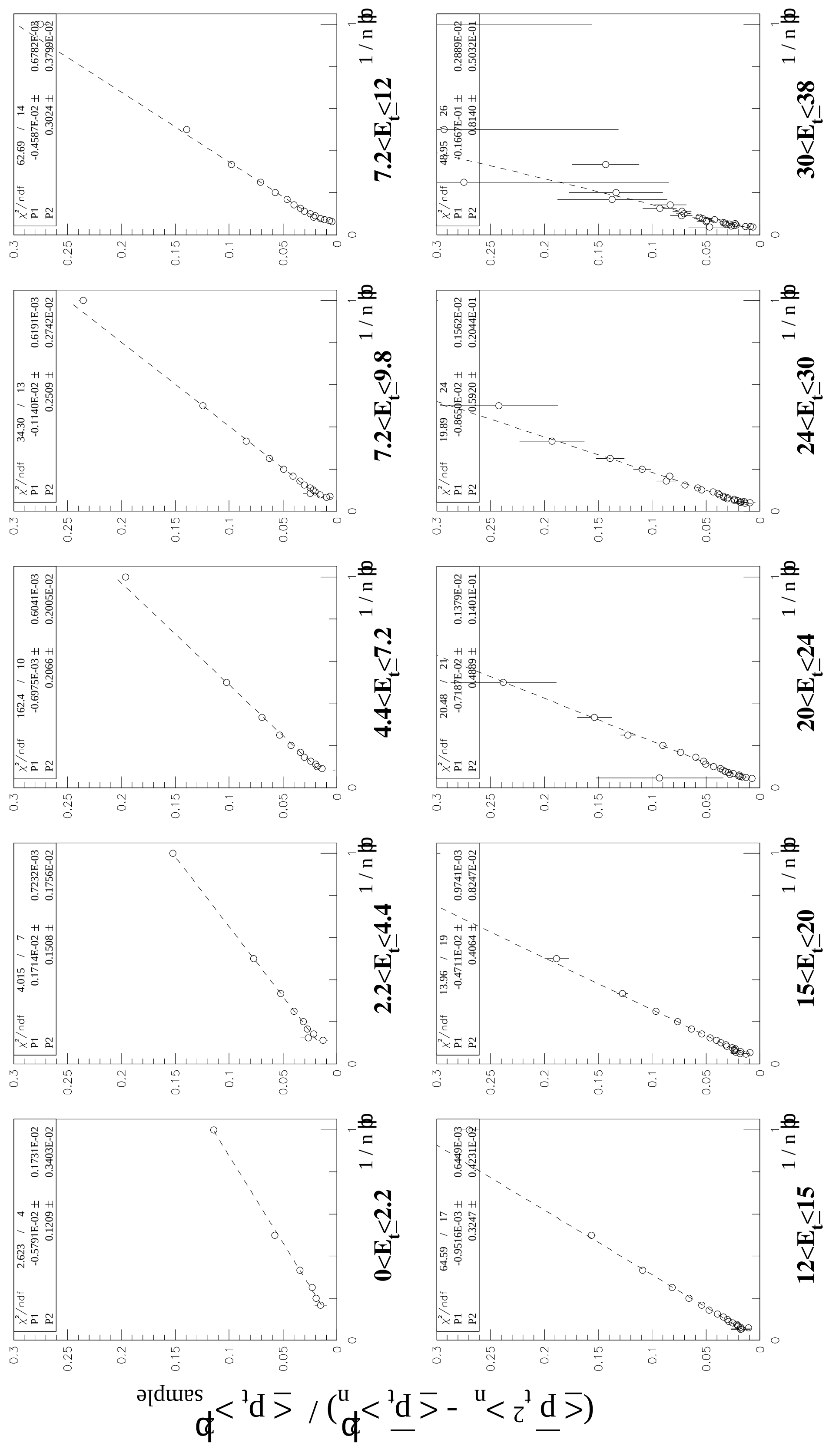

Figure 5.8: The $\langle p_t \rangle_{ev}$ dispersion at 630 GeV in 10 different E_t intervals.

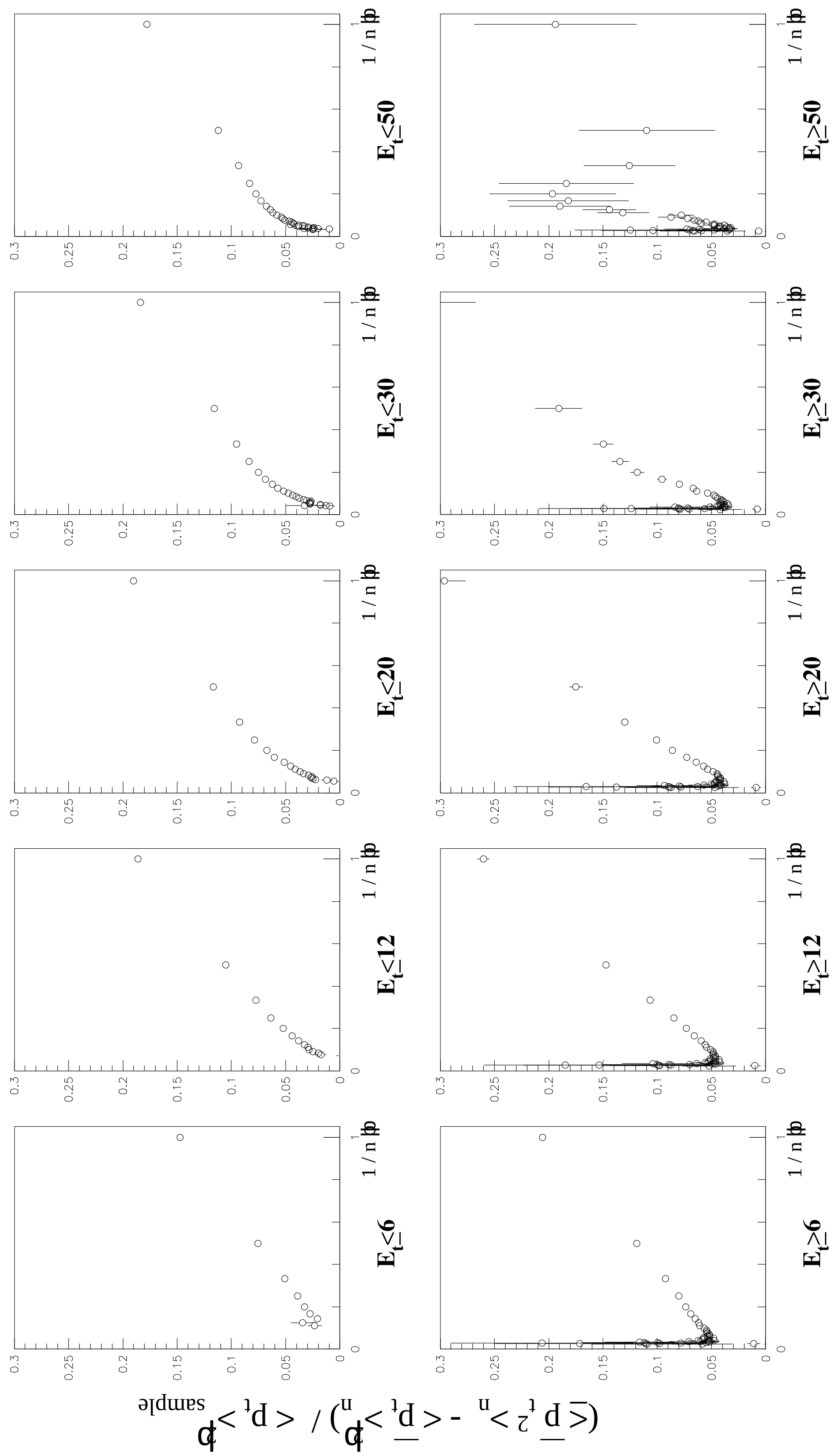

Figure 5.9: The $\langle p_t \rangle_{ev}$ dispersion at 1800 GeV for different E_t ranges.

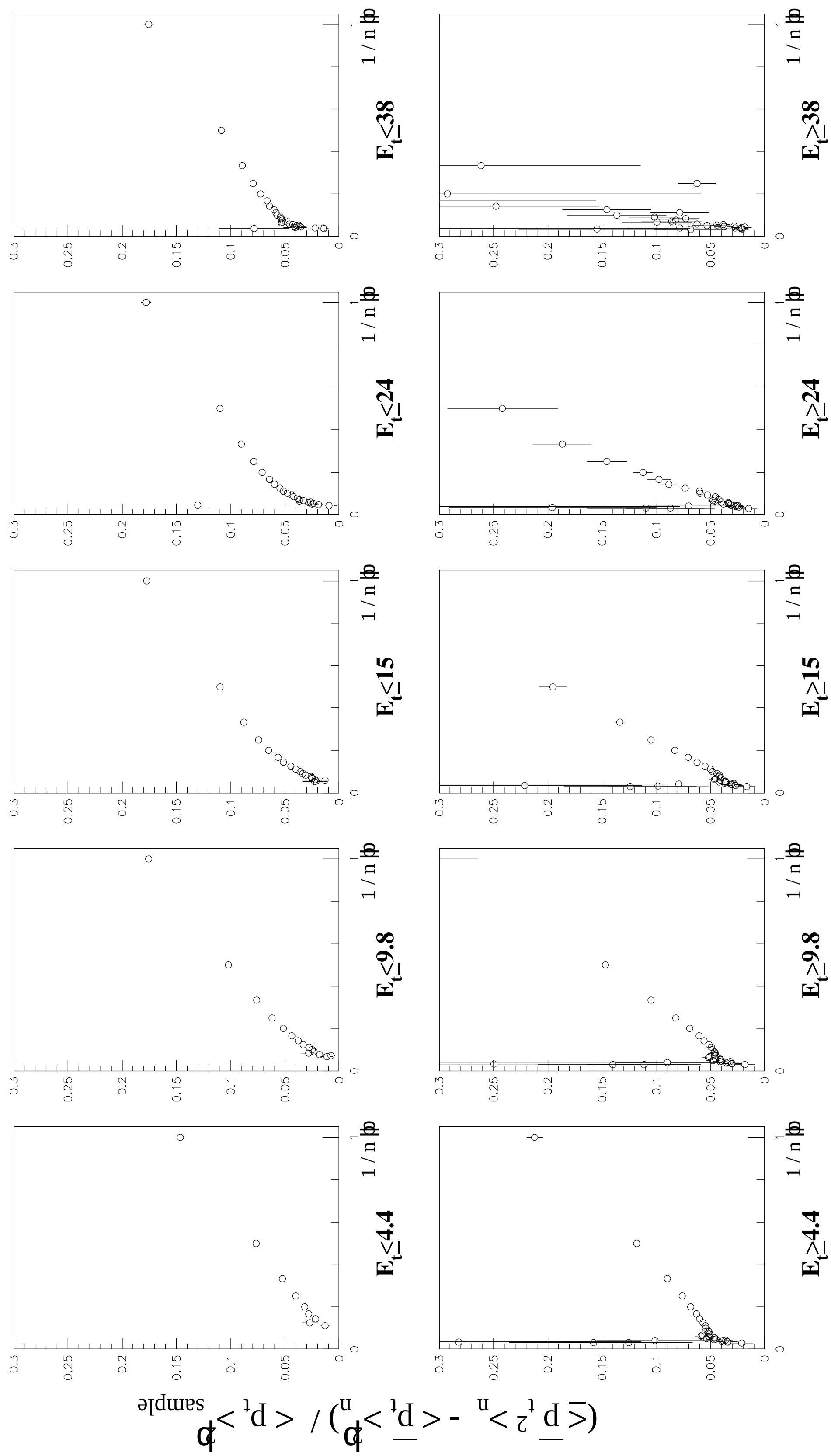

Figure 5.10: The $\langle p_t \rangle_{ev}$ dispersion at 630 GeV for different E_t ranges.

5.6 Production of low E_t Clusters

It is now established that "high E_t" jets are the observable result of a hard scattering between partons. The direction and energy of the jet - as defined by a suitable but arbitrary algorithm - provides a measure of the emitted partons.

As the jet energy decreases, one reaches a regime where the interpretation of the event topology becomes more difficult and the definition of what is a "jet" becomes arbitrary. Several reasons can be found for this: multiple parton-parton interactions [64], an increasing relative contribution to the transverse energy from gluon radiation as the momentum transfer Q^2 decreases [65], an increasing relative contribution from events of high multiplicity without real jet production but such that transverse energy fluctuations can be attributed to QCD jets.

In this work we have been using the CDF jet clustering algorithm, applied to minimum bias data, down to the smallest possible jet E_t values. Two main limitations have to be taken into account.

- First the separation of the contribution of the scattered partons to the total event E_t with respect to the rest of the event[1] is more difficult and the experimental definition of what is a jet becomes less reliable.

- Second it become more difficult to describe parton-parton collisions by QCD perturbative calculations and the direct identification of partons with jets may be questioned.

In our analysis *clusters* are defined by the CDF jet finding algorithm (see §5.6.1) which is based on calorimeter transverse energy deposition in $\eta - \phi$ space. The cluster energy and axis are defined by the vector sum of all energy depositions in a cone of radius $R = (\Delta\eta^2 + \Delta\phi^2)^{1/2} = 0.7$. Clusters are considered only if their axis is in the detector pseudorapidity interval $|\eta| < 2.4$, corresponding to the Central and End-Plug calorimeters.

[1] when dealing with high E_t well established jets it is called *underlying event* the contribution to the final state from spectator partons and initial state bremsstrahlung.

To the purpose of this analysis the low energy threshold for clusters was set to $E_t \geq 3$ GeV. This value is - of course - totally arbitrary and we cannot assume that jet interpretation is the only possible for such topologies. Considering that the UA1 collaboration suggests that clusters with $E_t > 5$ GeV are consistent with having a substantial component of QCD jets, the 3 GeV cut represents only the lowest reasonable limit below which any attempt to separe experimentally soft production fluctuations from hard scattering would be completely foggy and unreliable.

On the base of our definition of particle cluster, the full MB sample was split into two complementary subsamples. In the first one only events containing at least one cluster are included (from now on *cluster* or *hard* sample); the second one contains all other events (*non-cluster* or *soft* sample). The amount of events in each dataset is given in table 5.2.

	cluster	non-cluster
1800 GeV	532413	1547884
630 GeV	333521	1649191

Table 5.2: Number of events in the minimum-bias subsamples with and without clusters.

5.6.1 CDF Clustering Algorithm

In this section the CDF clustering algorithm is described. A more extensive discussion is given in [66].

The CDF calorimeter is composed of small cells (or towers) which form the basic unit of the clustering algorithm. The towers are assigned to clusters in three steps.

1) Preclustering. A search is made for towers above a fixed energy threshold (*seed* towers) $E_t > 1$ GeV. Seed towers are grouped together to form *preclusters*: a seed tower is added to a precluster if it is within a distance R in η and ϕ from the largest E_t tower in that precluster and it is adiacent to a seed tower already assigned to that precluster. The seed towers that are not assigned to a precluster are used too start a new precluster.

2) Cone Algorithm. A loop over the preclusters of step one is performed. For each cluster a loop over towers with E_t above a low threshold ($E_{tmin} > 0.1$ GeV) is performed. Towers are added to the cluster if they are within R of the centroid. This paramenter defines the so-called *cone radius*; for this analysis a radius of 0.7 was used.

The centroid of the cluster is then recalculated: if the list of towers for this cluster has changed, the loop over towers is repeated using the new cluster centroid. This process is repeated until the list of towers is unchanged in two consecutive passes.

3) Merge and/or resolve overlaps. After the above steps, some towers may end in being assigned to more than one cluster. In this stage the overlapping towers are separated or the clusters are merged together.

If the amount of overlapping energy is more than 75% of the smallest cluster then the clusters are merged. If the overlapping energy is less than the cut-off the shared towers are assigned to the nearest cluster. After the clusters have been separated or merged, the centroid of each cluster is recalculated using the new list of towers.

5.7 $\mathbf{p_t}$ Correlation with multiplicity

We measured the mean p_t dependence on the event multiplicity in the two minimum bias subsamples.

Both subsamples show a rise at low multiplicity followed by a flat region but the “soft” sample does not contain very high multiplicity events. The overall correlation can be described as the convolution of the two complementary event sets.

It is worth mentioning that the rise at low multiplicity is still present in the subsample with no clusters: an important indication that such rise cannot be attributed (only) to the onsetting of mini-jets.

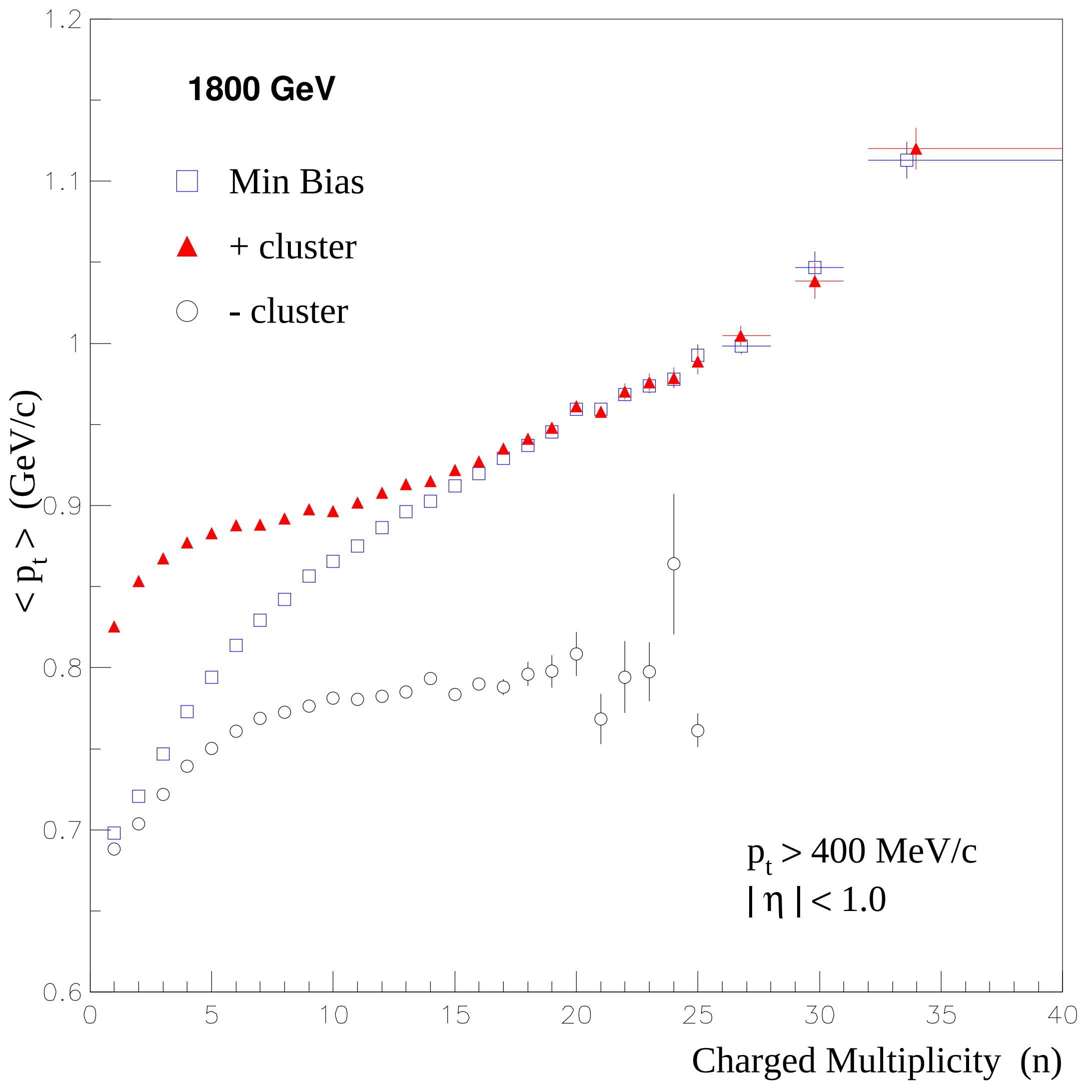

Figure 5.11: The correlation of p_t with multiplicity in the "cluster" and "non-cluster" data sets at 1800 GeV.

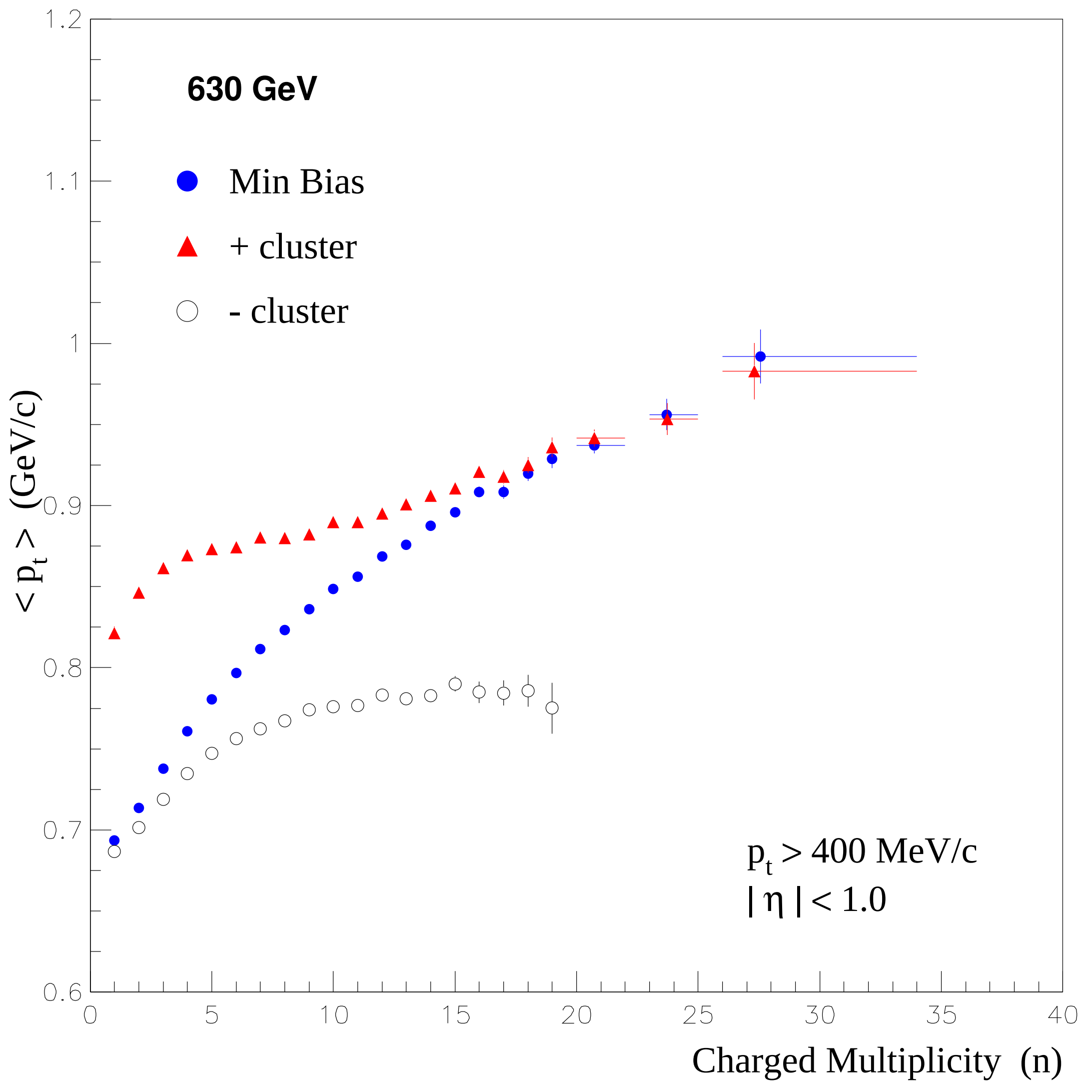

Figure 5.12: The correlation of p_t with multiplicity in the "cluster" and "non-cluster" data sets at 630 GeV.

5.8 $\langle \mathbf{p_t} \rangle_{\mathbf{ev}}$ Dispersion

The mean event p_t dispersion was computed for the cluster and non-cluster subsamples. Cluster data set show an increased non linearity at high multiplicity and a steeper rise at low multiplicity which gives a good linear fit at multiplicities ranging from 1 to about 10. The increasing of the dispersion after such multiplicities indicates that the corresponding deviation from linearity in the full minimum bias sample (clearly observable only at the higher energy) is due to the presence of hard parton interactions. The soft subsample is non-linear in all the multiplicity range (see table 5.3 for the results of the linear fit). It is remarkable that our points drop toward zero at high multiplicity, an unexpected behavior never observed before and qualitatively different from ISR data.

The value of the dispersion computed in the whole dataset is given in table 5.4

1800 GeV				
Sample	Mult. Range	$\chi^2/d.o.f.$	Intercept	Slope
no cluster	1 - 23	36	-0.0010±0.0001	0.236±0.001
no cluster	1 - 7	21	0.0222±0.0004	0.160±0.002
no cluster	8 - 23	21	-0.0074±0.0002	0.374±0.004
cluster	1 - 41	1.0	0.015±0.001	0.367±0.006
cluster	1 - 7	1.4	0.014±0.003	0.374±0.008
cluster	1 - 10	1.0	0.013±0.001	0.377±0.007
cluster	8 - 41	2.5	0.022±0.002	0.29±0.02

630 GeV				
Sample	Mult. Range	$\chi^2/d.o.f.$	Intercept	Slope
no cluster	1 - 21	68	0.012±0.001	0.180±0.001
no cluster	1 - 7	26	0.0221±0.0004	0.152±0.001
no cluster	8 - 21	3.5	0.0110±0.0003	0.202±0.005
cluster	1 - 33	3.9	0.015±0.001	0.364±0.001
cluster	1 - 7	1.4	0.014±0.002	0.374±0.001
cluster	1 - 10	1.0	0.013±0.001	0.377±0.001
cluster	8 - 33	3.7	0.024±0.002	0.268±0.002

Table 5.3: Parameters of different linear fits to the cluster and non-cluster dispersion at 1800 an 630 GeV.

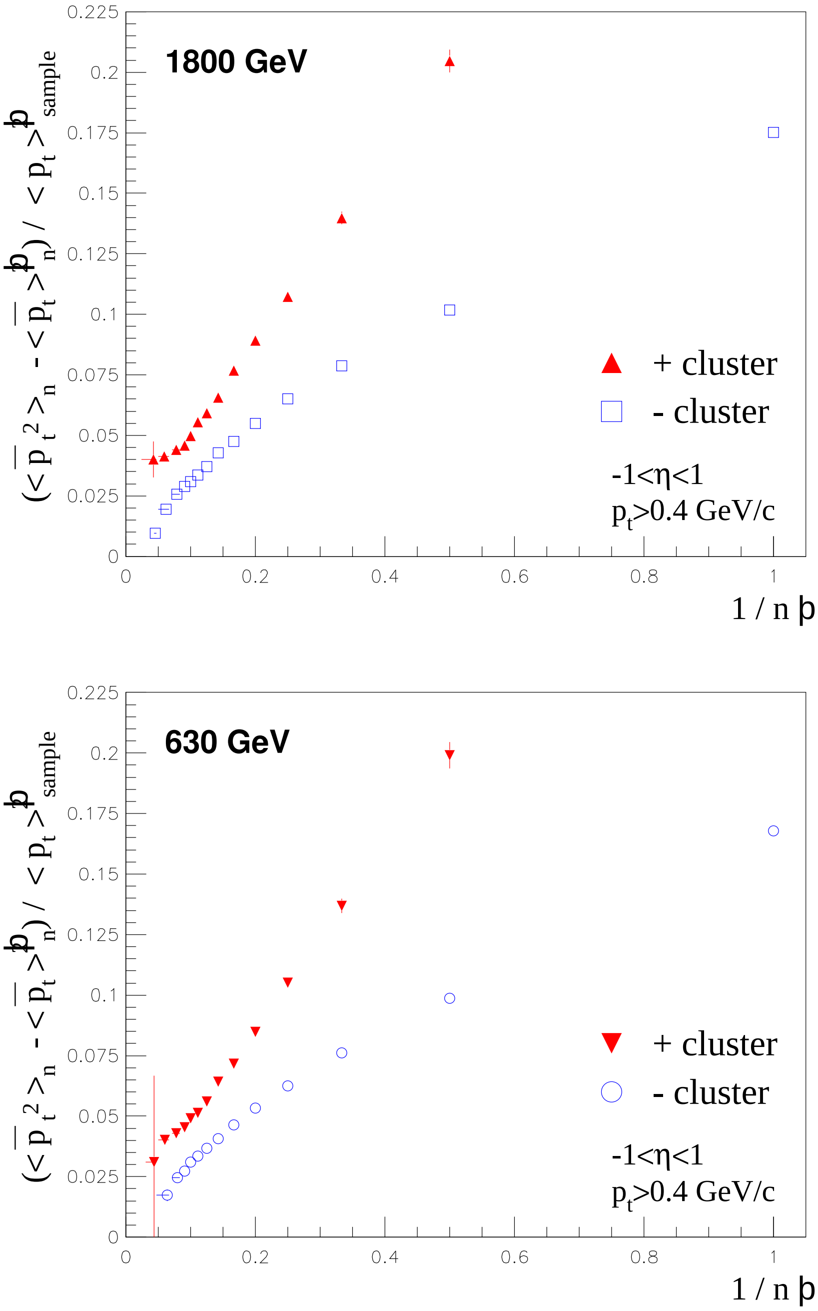

Figure 5.13: The $\langle p_t \rangle_{ev}$ dispersion in the "cluster" and "non-cluster" data sets at 1800 and 630 GeV is plotted against the inverse multiplicity.

Dispersion			
	cluster	non-cluster	min-bias
1800 GeV	0.092±0.001	0.1002±0.0004	0.1081±0.0004
630 GeV	0.107±0.004	0.1002±0.0003	0.110±0.001
Average $\langle p_t \rangle_{ev}$ (GeV/c)			
	cluster	non-cluster	min-bias
1800 GeV	0.8899±0.0004	0.7221±0.0002	0.7701±0.0002
630 GeV	0.8728±0.0005	0.7163±0.0002	0.7470±0.0002

Table 5.4: Dispersion and average event transverse momentum values in each dataset. Errors are statistical only.

5.9 Soft scaling properties

The cluster and non-cluster subsamples were compared at the two energies to investigate possible differences in the scaling properties. This procedure has the advantage that most of the systematic effects due to the detector response cancel since the data were taken with the same detector.

The multiplicity distribution of the soft sample as measured by the CTC in the known phase space limits, show an excellent scaling with `c.m.s.` energy if plotted in KNO form. Remarkably, also the hard sample scales when plotted in KNO variables, suggesting that the violation observed in the minimum bias is due to the different contribution of jet production at the two energies (figure 5.14). The mean multiplicity of each dataset is given in table 5.5.

Moreover, both the mean p_t correlation and $\langle p_t \rangle_{ev}$ dispersion of the soft data set completely overlap, within the statistical errors, at the two energies (figures 5.15 and 5.16). Regarding the event-by-event momentum dispersion it should be noticed that also the hard subsample shows scaling properties while this is not true for the other correlation.

	cluster	non-cluster
1800 GeV	7.581±0.006	2.716±0.002
630 GeV	6.133±0.007	2.447±0.002

Table 5.5: Mean multiplicity in the *soft* and *hard* samples. The errors reported are statistical only.

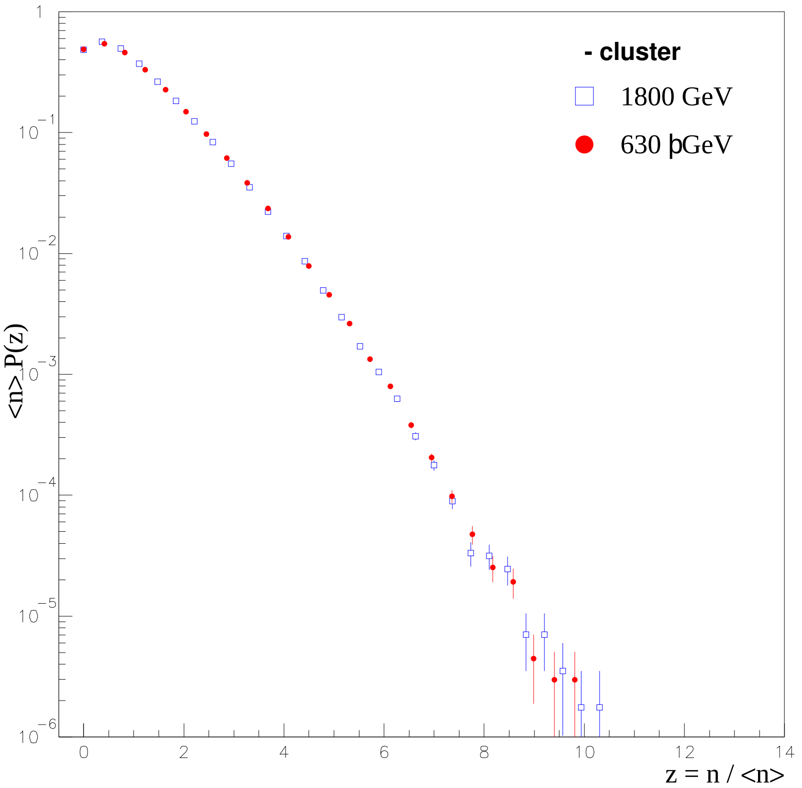

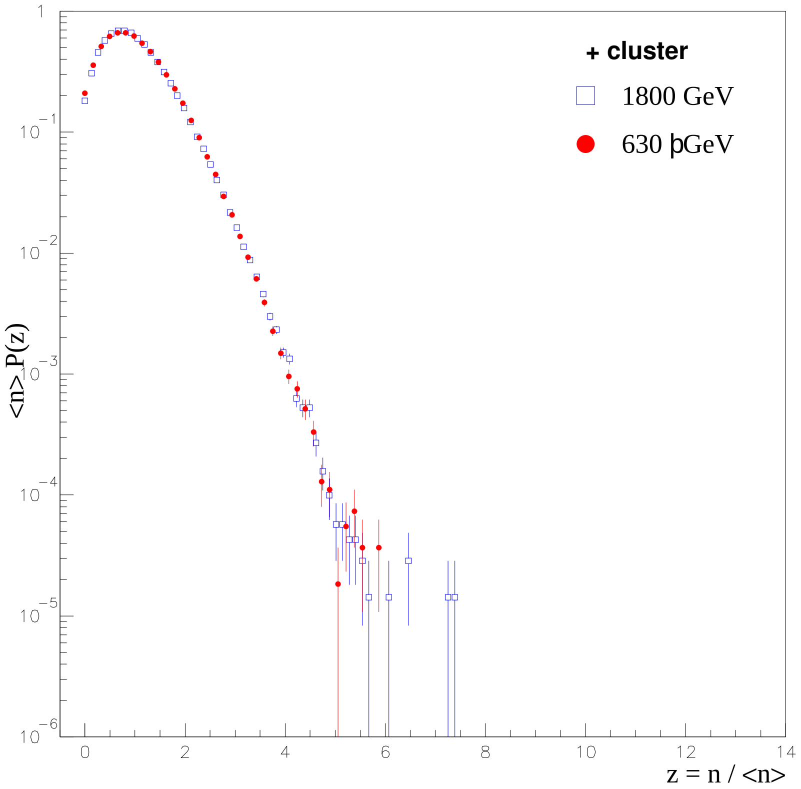

Figure 5.14: The multiplicity distribution for “non-cluster” (upper) and “cluster” (lower) events in KNO form.

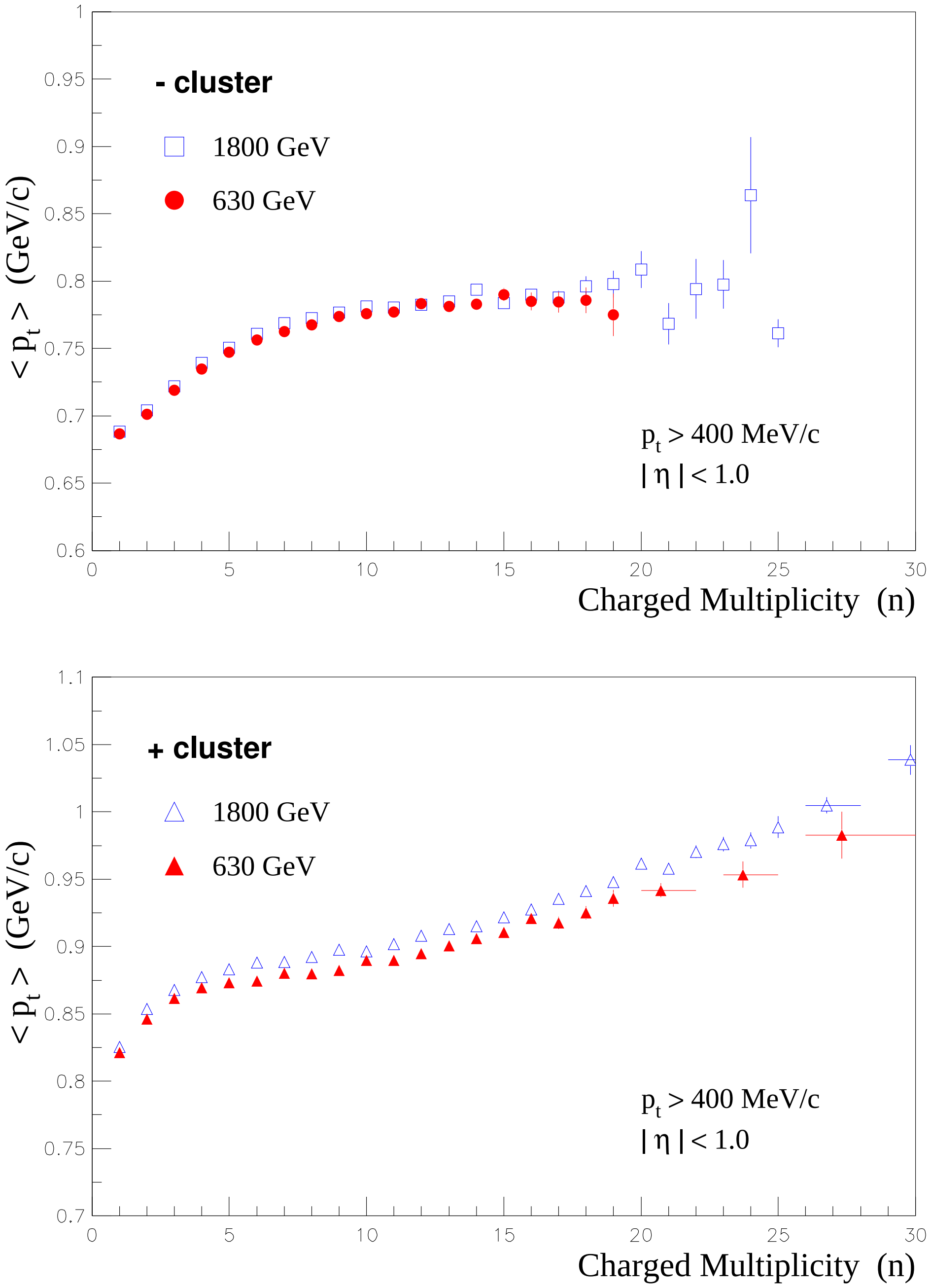

Figure 5.15: The correlation of p_t with multiplicity in the "non-cluster" (upper) and "cluster" (lower) data sets. Comparison of the two energies.

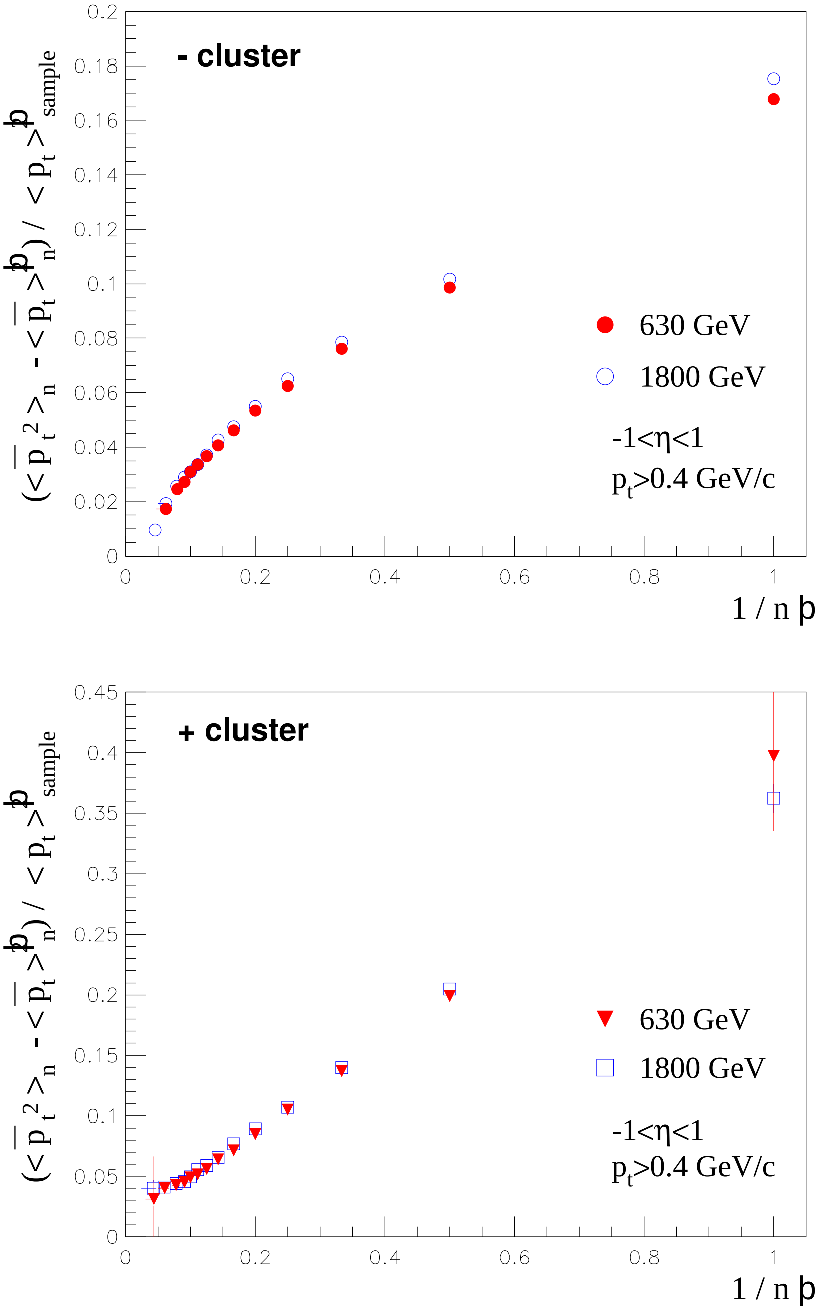

Figure 5.16: The dispersion of $\langle p_t \rangle_{ev}$ against inverse multiplicity in "non-cluster" and "cluster" events. Comparison of the two energies.

Conclusions

We have studied multiparticle low-p_t production in the central region in $\overline{p}p$ interactions. This field of high energy physics has probably not received in the last twenty years all the attention that it deserves, and no systematic studies are present in the literature, in particular at the highest energies now available.

For this reasons a more complete and comparative study is under way at CDF at `c.m.s.` energy of 1800 and 630 GeV.

Through a statistical analysis, some global properties of the minumum bias event have been examined as a function of the event charged multiplicity and total transverse energy E_t.

- The dependence of transverse momentum versus multiplicity is being studied. The high statistic collected allows for the first time a detailed analysis of the structures of this curve. The correlation, which can be regarded as a sign of a transition in the underlying production dynamics, seems to have a definite own structure that varies with the event E_t. In the minimum bias sample the shape of the correlation is described as the convolution of the correlation in different energy intervals, indicating a continuous change of the event properties with E_t.

- The dispersion of the mean event transverse momentum $\langle p_t \rangle_{ev}$ indicates the presence of non statistical event-to-event fluctuations. In minimum bias the dispersion as a function of the inverse multiplicity is strongly non linear (more evidently at the higher energy and for multiplicity greater than about 10) which is in contrast with the last known measures from the ISR at 63 GeV.

The behavior is different in limited E_t ranges, where dispersion seems to decrease linearly with multiplicity. The growth at higher multiplicities seems to be due to the high E_t events.

- The same analyses were applied in two different subsamples of minimum bias data: one which contains events where at least one energy cluster of $E_t >$ 3 GeV can be found, and a second one which does not contain such clusters. We assume that hard parton interactions are enriched in the first one and at least strongly dumped in the second one.

  Both the p_t correlation and the $\langle p_t \rangle_{ev}$ dispersion are very different in the two data sets. It is remarkable that these event global variables in the "soft" sample seem to have scaling properties with the `c.m.s.` energy. The multiplicity distribution itself, in the limited phase space region which is accessible to our tracking, seems to obey KNO scaling.

  This important observation suggests that the soft component of Minimum Bias has statistical features that scale with the `c.m.s.` energy. In other words, its specific properties are characterized independently of the total energy of the system.

Appendix

Min Bias Pythia Configuration

The tuning of the MonteCralo generator was made by using the published CDF p_t spectrum and the CTC measure of the charged multiplicity ("raw" data). The following parameters were adjusted to best match the data (for more detail refer to the generator manual [53]).

MSEL=1 QCD high p_t processes plus "low-p_t" production.

MSTP(2)=2 Second order running α_s.

MSTP(33)=3 Inclusion of K factors in hard cross-sections for parton-parton interactions. A factor is introduced by a shift in the α_s Q^2 argument.

MSTP(81)=1 Allows multiple parton-parton interactions.

MSTP(82)=4 Assumes a varying impact parameter for multiple interactions and a hadronic matter overlap consistent with a double Gaussian matter distribution given by parameters PARP(83) and PARP(84).

PARP(83)=0.2 Fraction of the total hadronic matter contained in the core radius od the double Gaussian matter distribution inside the colliding hadrons.

PARP(84)=0.5 Core radius of the double Gaussian matter distribution inside the colliding hadrons.

Bibliography

[1] S. L. Glashow, Nucl. Phys. **22** (1961) 579;
S. Weinberg, Phys. Rev. Lett. **19** (1967) 1264.

[2] For a full list of references on the birth of QCD see, e.g.,
G. Altarelli, Phys. Rep. **81**(1982) 1.

[3] N. Amos *et al.*, Phys. Rev. Lett. **68** (1992) 2433.

[4] F. Abe *et al.*, Phys. Rev. **D50** (1994) 5550.

[5] J. C. Collins, D. E. Soper and G. Sterman, *Factorization of hard processes in QCD* in "Perturbative QCD", World Scientific, Singapore.

[6] G. J. Alner *et al.*, Phys. Rep. **154** (1987) 247.

[7] M.Demarteu, $P\bar{P}$ *Collider Physics*, FERMILAB-Conf-92/103.

[8] CDF Coll., *Log(s) Physics Results from CDF*, Proc. European Physical Society, International European Conference on High Energy Physics, Madrid, Spain, Sept 6-13, 1989.

[9] J. Bjorken and J. Kogut, Phys. Rev. **D8** (1973) 1341.

[10] G.Arnison *et al.*, Phys. Lett. **118B** (1982) 167;
M.Banner *et al.*, Phys. Lett. **122B** (1983) 322;
M.Banner *et al.*, Z. Phys **C27** (1985) 329.

[11] G. J. Alner *et al.*, Phys. Rep **154** (1987) 247.

[12] F. Rimondi, Proc. of XXIII Intl. Symposium on Multiparticle Dynamics, Aspen, USA, 12-17 Sept. 1993.

[13] K. Goulianos, *Universality of Multiparticle Production*, Lectures at the 3^{rd} Wataghin School on High Energy Phenomenology, 11-16 July 1994, Campinas, Sao Paulo, Brasil.

[14] A. Giovannini and L. Van Hove, *Negative Binomial Properties and Clan Structure in Multiplicity Distributions*, CERN-TH 4894/87 (1987).

[15] G. J.Alner *et al.*, Phys. Lett. **138B** (1984) 304.

[16] R.E.Ansorge *et al.*, Z. Phys. **43C** (1989) 357.

[17] UA5 Coll., Proc. of the International Europhysics Conference on High Energy Physics, Bari, Italy, 363, (1985);
G.Arnison *et al.*, Phys. Rev. Lett. **60** (1988) 405.

[18] Z. Koba, H. B. Nielsen, P. Olesen, Nucl.Phys. **B40** (1972) 317.

[19] T. Alexopoulos *et al.*, Phys. Rev. Lett. **60** (1988) 1622.

[20] T. Alexopoulos *et al.*, Phys. Rev. Lett. **64** (1990) 991;
A.Breakstone *et.al* Z. Phys. C33 (1987) 333.

[21] G. Pancheri and C. Rubbia, Nucl.Phys **A418** (1984) 117;
A. Pancheri and Y. Srivastava, Phys. Lett. **159B** (1985) 69;
F. W. Bopp, P. Aurenche and J. Ranft, Phys. Rev. **D33** (1986) 1867.

[22] L. Van Hove, Phys. Lett. **118B** (1982) 138.

[23] A. Giovannini and L. Van Hove, Acta Phys. Pol. **B19** (1988) 495, 917, 931.

[24] L. A. De Wolf, I . M. Dremin and W. Kittel, Phys.Rep. **270** (1996) 1.

[25] A. Bialas and R. Peschansky, Nucl. Phys. **B273** (1986) 703;
A. Bialas and R. Peschansky, Nucl. Phys. **B308** (1988) 857.

[26] W. Braunschweig *et al.*, Phys. Lett. **B231** (1989) 548;
I. V. Ajinenko *et al.*, Phys.Lett. **B222** (1989) 306;
I. V. Ajinenko *et al.*, Phys.Lett. **B235** (1990) 373;
C. Albajar *et al.*, Nucl. Phys. **B345** (1990) 1.

[27] F. Halzen *From hard to soft collisions*, Proc. of the International Symposium of Very High Energy Cosmic Rays Interactions. Lodz, Poland, 1988.

[28] T. K. Gaisser and F. Halzen, Phys. Rev. **54** (1985) 1754;
T. K.Gaisser *et al.*, Phys. Lett. **B166** (1986) 219.

[29] L. V. Grobov, E. M. Levin and M. G. Ryskin, Phys.Rep. **100** (1983) 1.

[30] J. Kwiecinski, Inst. of Nucl. Phys., Cracow, Report 1338/PH (1986);
I. Sarcevic, Phys. Rev. **D40** (1989) 1446.

[31] C. Albajar *et al.*, Nucl. Phys. **B309** (1988).

[32] A. Giovannini and R. Uguccioni, Nucl.Phys. **B** (proc.Suppl.) (1999) 71.

[33] T. Sjöstrand and M. van Zijl, Phys. Rev. **D36** (1987) 2019.

[34] B. Andersson, G. Gustafson, G. Ingelman and T. Sjöstrand, Phys. Rep. **97** (1983) 33;
T. Sjöstrand, Phys. Lett **142B** (1984) 420;
T. Sjöstrand, Nucl. Phys. **B248** (1984) 469.

[35] A. Capella *et al.*, Phys. Lett. **B81** (1979);
A. Capella *et al.*, Phys. Lett. **C3** (1980) 329;
A. Capella and J. Tran Tan Van, Z. Phys. **C23** (1984) 165;
P. Aurenche *et al.*, Z. Phys. **C23** (1984) 67;
P. Aurenche *et al.*, Z. Phys. **C26** (1984) 279;
P. Aurenche *et al.*, Phys. Lett. **B147** (1984) 212;
P. Aurenche *et al.*, Phys. Rev. **33D** (1986) 1876.

[36] P. D. B.Collins and A. D. Martin, *Hadron Interations* Adam Hilger LTD, Bristol, 1984.

[37] J. D. Bjorken, Int. J. Mod. Phys. **A7** (1992) 4189.

[38] E. Fermi, Progr. Theor. Phys. **5** (1950) 570.

[39] L. D. Landau, Izv. AN SSSR, ser. fiz. **17** (1953) 51.

[40] E. V. Shuryak, Phys. Lett. **78B** (1978) 150;
D. J. Gross, R. D. Pisarsky and L. G. Yaffe, Rev. Mod. Phys. **53** (1981) 43;
J. Cleymans, R. V. Gavari and E. Suchonen, Phys. Rep. **C130** (1986) 217.

[41] L. Van Hove, Nucl. Phys. **A** (1986) 447;
E. V. Shuryak, Phys. Rep. **61** (1980) 71.

[42] J. D. Bjorken, Phys. Rev. **D27** (1983) 140.

[43] J. Schurkraft, Nucl. Phys. **A553** (1993) 31C.

[44] I. M. Dremin and A. V. Leonidov, *Theoretical search for collective effects in multiparticle production*, FIAN-TD-8-95 (1995).

[45] M. Jacob and P. V. Landshoff, *Deep inside matter* CERN-TH.4556/86 (1986).

[46] B. Andersson, G. Jarlskog and G. Damgaard, Nucl. Phys. **B112** (1976) 413.

[47] L. Van Hove, Phys. Lett. **118B** (1982) 138.

[48] F. Abe *et.al.*, Nucl. Instrum. Methods **A 271** 387 (1988) and the references therein.
D. Amidei *et al.*, Nucl. Instr. Meth. **A 289** (1990) 388;
D. Amidei *et al.*, Nucl. Instr. Meth. **A 350** (1994) 73;
F. Abe *et al.*, CDF internal note 1172 (1990);
D. Amidei *et al.*, Nucl. Instr. Meth. **A 268** (1988) 50;
L. Balka *et al.*, Nucl. Instr. Meth. **A 267** (1988) 272;
S. Bertolucci *et al.*, Nucl. Instr. Meth. **A 267** (1988) 301.
Y. Fukui *et al.*, Nucl. Instr. Meth. **A 267** (1988) 280;
G. Ascoli *et al.*, Nucl. Instr. Meth. **A 268** (1988) 33;
G. Ascoli *et al.*, Nucl. Instr. Meth. **A 269** (1988) 63;
D. Amidei *et al.*, Nucl. Instr. Meth. **A 269** (1988) 51;
J. T. Caroll *et al.*, Nucl. Instr. Meth. **A 300** (1992) 552.

[49] CDF internal note 4721.

[50] CDF internal note 884.

[51] CDF internal note 1534.

[52] CDF internal note 4139.

[53] T. Sjöstrand, Computer Physics Commun. **82** (1994) 74.

[54] CDF internal note 1810.

[55] W. Yuanfang *et al.*, Proc. of XXIV Int. Symp. on Multiparticle Dynamics, Vietri sul Mare, Italy, 12-19 Sept.(1994).

[56] CDF internal note 2886.

[57] A. Byon, *Central Production of Charged Particles at CDF*, Purdue Univ. Ph.D Thesis (1989)
and CDF internal note 741.

[58] F. Becattini, private communication.

[59] F. Abe *et al.*, Phys. Rev. Lett. **61** (1988) 1819.

[60] K. Braune *et al.*, Phys. Lett. **B123** (1983) 467.
G. Giacomelli, Intl. J. Mod. Phys., **A5** (1990) 223.

[61] S. Barshay *et al.*, Phys. Lett. **73B** (1978) 437.

[62] B. W. Lindgren. *Statistical Theory* 3^{rd} Ed., Macmillan Pub. Co., New York, pg. 216.

[63] CDF internal note 4358.

[64] T. Akesson *et al.*, Z. Phys. **C34** (1987) 163.

[65] C. Albajar *et al.*, Z. Phys. **C36** (1987) 33.

[66] CDF internal note 605.